STUDIES ON DYNAMICS OF FINANCIAL MARKETS AND REACTING FLOWS

A Dissertation

Presented to

the Faculty of the Department of Physics

University of Houston

In Partial Fulfillment

of the Requirements for the Degree

Doctor of Philosophy

By

Jia-Chen Hua

August 2014

STUDIES ON DYNAMICS OF FINANCIAL MARKETS AND REACTING FLOWS

Jia-Chen Hua

APPROVED:

Gemunu H. Gunaratne, Professor and Chairman
Department of Physics

Kevin E. Bassler, Professor
Department of Physics and Mathematics

Joseph L. McCauley, Professor
Department of Physics

Andrew Török, Professor
Department of Mathematics

Dean, College of Natural Sciences and Mathematics

Acknowledgements

I would like to express my deepest appreciation and thanks to my advisor Professor Gemunu H. Gunaratne, for making me part of his research group and for his support, encouragement and guidance during the last three-and-a-half years. I am truly grateful to him for sharing with me his ingenious insight, remarkable erudition, and incredible problem solving skills, and for his inspiring energy, indefatigable enthusiasm, and well-known generosity. He is definitely a tremendous mentor and his advice is always priceless. Without his supervision and constant help this dissertation would not have been possible.

I am especially grateful to Professor Joseph L. McCauley, who is in principle my second advisor. Without his strong recommendation, I would not have been accepted by Professor Gunaratne to join in his group. He is actually the reason why I transfered to UH from New Mexico State University. His unique perspective on science, mathematics, philosophy, and economics is always an eye-opener for me. I feel lucky and honored to have worked with him and learned from him.

I am very thankful to Professor Kevin E. Bassler, for his signature-like critical insight and questioning, which was quite helpful in developing research work. It was he who initiated me to check the correction of quadratic term in the expansion of scaled diffusion coefficient in our variable diffusion model. I also thank him for his strict (or even harsh sometimes) attitude towards first-year students. It was he who spurred me to bounce back from my misery and low productive first year.

I thank Professor Bambi Hu and Professor Andrew Török for agreeing to serve on my dissertation committee. Although unfortunately, Professor Hu will not be

able to be at the defense, I appreciate him for his interesting introduction to KAM theory in his course on phase transition.

I thank my former colleague Lars Seemann, for his faithful collaboration in our research projects. I actually learned programming in "modern" languages (compared to plain C and Fortran) from him. His excellent programming skills saved us a lot of precious time and always pushed our research to progress rapidly.

I am thankful to Professor Michael Gorman, whose pioneering work provides data for our latest analytical methods on dynamics of reacting flows. I still remember the day about three-and-a-half years ago when I proctored his exam. It was an obligation as a TA to help professors proctor exams; however, he still paid me for the unexpected delay in the end of that exam. His unfortunate and untimely death was a pity and a significant loss to our department. I thank Dr. Sukesh Roy, an outstanding alumni of UH and CEO of Spectral Energies LLC. Without his high quality experimental data, our analysis on reacting flows would not have been possible.

I wish to thank Professor William Ott and Professor Edward Kao, for their interesting math courses. Pure math is always beautiful and attractive to me, although I am too old to start a new PhD career in mathematics after I finish this current one. I also thank Professor George Reiter, whose choice of V. I. Arnold's stimulating masterpiece as textbook for classical mechanics course reminded me of the beauty of differential geometry, and encouraged me through the frustrating first year here in UH. That course was actually the only one in which I got an A in my first year.

I am thankful to my college classmates Jinlong Yang and Di Chang, and my high-school classmate Chuan Shen. The somewhat unexpected continuation of friendship

on the other side of earth is nothing but amazing. I thank them and all my other classmates in UH for making my life experience in Houston enriched and fun. I specially thank Jinlong Yang, who provided generous help in perhaps the hardest time in my life. I also thank Si Xu, Yan Yang, and Iris Zhu, for their accompanying me during the memorable period of time that I spent in New Mexico.

I am grateful to Professor Yong-Chang Huang, who introduced me to the wonderful world of theoretical physics, and built me a solid background in mathematics, which I found extremely helpful in my later career, although I have switched to more computationally focused research now. I want to thank one of the best friends of my mother, Meilin Yan and her husband Dr. Xuan-Min Shao, for their helping me to come to this country. I express my sincere gratitude to my parents for their indispensable support, patience, and encouragement.

Finally, I want to pay homage to Glenn Gould, who has been my spiritual master for many years. His philosophical viewpoint on music and art and his attitude towards life always serves as treasures for me to esteem. His performance and interpretation of Johann Sebastian Bach's music significantly improved my productivity in research work. I could not imagine a life or work environment without listening to him playing Bach's music. Living a lifestyle as he did is perhaps the biggest dream in my life.

STUDIES ON DYNAMICS OF FINANCIAL MARKETS AND REACTING FLOWS

An Abstract of a Dissertation

Presented to

the Faculty of the Department of Physics

University of Houston

In Partial Fulfillment

of the Requirements for the Degree

Doctor of Philosophy

By

Jia-Chen Hua

August 2014

Abstract

One of the central problems in financial markets analysis is to understand the nature of the underlying stochastic dynamics. Several intraday behaviors are analyzed to study trading day ensemble averages of both high frequency foreign exchange and stock markets data. These empirical results indicate that the underlying stochastic processes have nonstationary increments. The three most liquid foreign exchange markets and five most actively traded stocks each contains several time intervals during the day where the mean square fluctuation and variance of increments can be fit by power law scaling in time. The fluctuations in return within these intervals follow asymptotic bi-exponential distributions. Based on these empirical results, an intraday stochastic model with linear variable diffusion coefficient is proposed to approximate the real dynamics of financial markets to the lowest order, and to test the effects of time averaging techniques typically used for financial time series analysis. The proposed model replicates major statistical characteristics of empirical financial time series and only ensemble averaging techniques deduce the underlying dynamics correctly. The proposed model also provides new insight into the modeling of financial markets' dynamics in microscopic time scales.

Also discussed are analytical and computational studies of reacting flows. Many dynamical features of the flows can be inferred from modal decompositions and coupling between modes. Both proper orthogonal (POD) and dynamic mode (DMD) decompositions are conducted on high-frequency, high-resolution empirical data and their results and strengths are compared and contrasted. In POD the contribution of each mode to the flow is quantified using the latency only, whereas each DMD mode can be associated a latency as well as a unique complex growth rate. By

comparing DMD spectra from multiple nominally identical experiments, it is possible to identify "reproducible" modes in a flow. A similar differentiation cannot be made using POD. Time-dependent coefficients of DMD modes are complex. Even in noisy experimental data, it is found that the phase of these coefficients (but not their magnitude) exhibits repeatable dynamics. Hence it is suggested that dynamical characterizations of complex flows are best analyzed through the phase dynamics of reproducible DMD modes.

Contents

List of Figures

List of Tables

Part I

Variable Diffusion Model for Financial Markets

Chapter 1

Introduction

1.1 Motivation and Background

Sir Isaac Newton stated, "I can calculate the motions of the heavenly bodies, but not the madness of people [1]"; the dynamics of financial markets results from collective behavior of multiple interacting agents, which should be understood as a complex system. This complexity results in a stochastic dynamics. Understanding the stochastic processes underlying financial markets has been the central problem of both quantitative finance and econophysics. Early work proposed several models to explain financial time series (see, e.g., [2, 3] for a review). For example, the well-known Black and Scholes option pricing model [4, 5] assumed that the stochastic dynamics of the underlying asset was a geometric Brownian motion. However, analysis of high quality data of financial time series which became widely available in the past two decades made it clear that the assumptions underlying the Black-Scholes theory were invalid, and researchers conducted empirical analysis on the statistical properties of the underlying stochastic processes. Important statistical characteristics of a time series are its volatility as well as the distribution of fluctuation in returns and the autocorrelation function. It was reported that the empirical distributions contain power law (or fat) tails and scale in time [6, 7, 8, 9, 10, 11]. However, these studies assumed that the underlying process was stationary (i.e., identical at all times) and hence the statistical analysis was conducted by mixing increments of returns at different time (so-called sliding interval methods). However, it is unclear if financial markets are governed by stationary stochastic processes. For example, it is possible and reasonable that trading activity changes with time within a trading day (so-called intraday "seasonality"[7, 12, 13, 14]). Such empirical findings would

invalidate stationary increments assumption and make sliding interval techniques inappropriate for assessing financial time series.

In order to avoid spurious stylized facts resulting from applying inappropriate statistical methods, an alternative approach, i.e., method of ensemble averages over the set of trading days, has been discussed and proposed [15, 14, 16]. The validity of this approach has been justified in Ref. [17] by comparing the statistical characteristics from time and ensemble averages applied to both empirical high-frequency foreign exchange data and simulated time series. This finding also validates the variable diffusion model used in simulation, in that it exhibits key statistical properties of the empirical financial time series (so-called zeroth-order approximation [18]). Similar efforts have been extended to verify the variable diffusion model and re-emphasize the importance and validity of ensemble average methods based on empirical stock markets data [19], which also provides new insight and a macroscopic time scale limit for various stochastic models in microscopic time scale for financial market dynamics (in analogy to thermodynamic limit of statistical mechanics), for example, order book modeling [20] as discussed in 3.3.

1.2 Notations and Definitions

Before discussing the details of variable diffusion model, we need to introduce several key notations and definitions to avoid confusions that frequently appear in financial literature.

Financial time series are stochastic processes. Their dynamics are described by

the return $X_t = \ln\frac{P_t}{P_0}$, where P_t represents the price of a financial asset or contract, e.g., the Euro-Dollar exchange rate or stock price of Intel, and P_0 is a reference price. The dynamics of log return X_t are typically modeled as an Itō process

$$dX_t = \mu dt + \sigma dB_t, \tag{1.1}$$

where μ and σ can depend on X_t and t in general, either deterministically or stochastically. They degenerate to constants for geometric Brownian motion such that $P_t = P_0 e^{\mu t + \sigma B_t}$, and B_t is centered standard Brownian motion with zero mean $\mathbb{E}[B_t] = 0$ and $\mathrm{Var}(B_{t_2} - B_{t_1}) = t_2 - t_1$. We assess the underlying stochastic dynamics using increments of the return given by

$$X_{t_2;t_1} \equiv X_{t_2} - X_{t_1} = \ln\frac{P_{t_2}}{P_0} - \ln\frac{P_{t_1}}{P_0}, \tag{1.2}$$

so that $X_{0;0} = 0$. The advantages of this definition are that the return is dimensionless and additive, and it is in analogy to signal gain measured in decibels.

Scaling, as discussed later, i.e., $X_t \overset{d.}{=} t^H X_1$, where "d." denotes "in distribution", will require $X_0 = 0$ almost surely (i.e., with probability 1), so we usually write $X_{t;0}$ as X_t, $B_{t;0}$ as B_t, and also $\sigma = \sqrt{D}$ (see explanations in section 1.4).

In empirical analysis we are interested in the increments $X_{t+\tau;t}$ which is the growth of X during t to $t + \tau$. We choose τ to be 10 minutes [14] since there are short-term correlations in financial time series. Note that the increments $X_{t+\tau;t}$ may depend on both the time lag τ and time within the day t. The corresponding distribution of increments is denoted by $W(x, t + \tau; t)$. If the distribution $W(x, t + \tau; t)$ is independent of time t and only depends on τ, the process is said to have *s*tationary increments. Consider the well-known example of Geometric Brownian

Motion (GBM): The distribution of increments only depends on the time difference τ and is independent of t. The variance of GBM is linear in τ. However, generally $W(x, t+\tau; t)$ can depend on t and $W(x, t+\tau; t)$ can not be estimated by averaging over t ($s$liding interval methods).

1.3 Motivations of Variable Diffusion Model

Real financial markets are very hard to beat, if not impossible. Arbitrage possibilities are hard to find and once known, tend to disappear fast. Ref. [21] suggested that the efficient market hypothesis (EMH) is simply an attempt to formalize the idea that the market is very hard to beat. At least, at the level of simple averages and pair correlations, nothing that happened in an earlier time interval can be used to predict systematically the returns in a later time interval [22]. That means the pair correlation of non-overlapping increments will vanish and the underlying stochastic process has no memory at the lowest order.

Based on these facts, there are 3 possibilities for the underlying stochastic process: statistical independence, drift-free Markov process, and more general Martingales [21], sorted in an order of systematic reduction in restrictions. Statistical independence is ruled out by "volatility clustering" discussed later. And to distinguish between drift-free Markovian and Martingales, higher order correlations are required. Unfortunately, due to the limited amount of empirical data available, it is impossible to obtain a reliable higher order correlations. Nevertheless, even if

such correlations exist and could be traded on, they would be arbitraged away, making the market even more effectively Markovian. So drift-free Markovian is a good zeroth-order approximation of the underlying stochastic process. It is "efficient" in the strictest sense: it has no memory of any kind to exploit and impossible to beat. A drift-free Markovian can be expressed by a stochastic differential equation (SDE) $dX_t = \sqrt{D(\cdot)}dB_t$ [23], where $D(\cdot)$ has no dependence on history of any kind.

Volatility clustering means that autocorrelation of non-overlapping squared and absolute increments decays slowly. It implies that large fluctuations are likely to be followed by additional large ones; although the magnitude of fluctuations is pair correlated, the direction is not. Therefore it should not be confused with a memory effect on the return. Instead, it is a Markovian effect with a non-trivial variable diffusion coefficient [21], or more precisely, an $|X_t|$ dependent diffusion coefficient $D(|X_t|, \cdot)$ [24, 25]. This phenomenon rules out statistically independent processes including Lévy processes [25]. It also rules out other models proposed by mathematicians, e.g., stochastic volatility model.

Finally, scaling will require a t-dependent form of diffusion coefficient, as discussed below.

1.4 Scaling

A stochastic process X_t is said to scale with a Hurst exponent H if

$$X_t \stackrel{d.}{=} t^H X_1, \tag{1.3}$$

where equality is in distribution [26, 27]. Scaling (or more precisely, approximate scaling) is widely observed in financial market data. It can be used to simplify the model, but it bears no relation to pair correlation or efficient market hypothesis (EMH) [28, 23]. By a transformation of random variable, one can see that the distribution of X_t, or in other words, the probability density $W(x,t;0)$ scales as

$$W(x,t;0) = t^{-H}F(u), \tag{1.4}$$

where $u = \frac{X_t}{t^H}$ is called scaling variable and $F(u)$ is called scaling function. Note that scaling also implies $\mathrm{Var}(X_t) = t^{2H}\langle X_1^2\rangle$, where $\langle\cdot\rangle$ denotes an ensemble average. Combining the SDE $dX_t = \sqrt{D(X_t,\cdot)}dB_t$ by using Itō's calculus, one can obtain

$$D(X_t,\cdot) = t^{2H-1}D(u), \tag{1.5}$$

which means that diffusion coefficient depends on t explicitly and scales with index $(2H-1)$.

Given the scaling form of diffusion coefficient (1.5) and variable diffusion SDE

$$dX_t = \sqrt{D(X_t,t)}dB_t, \tag{1.6}$$

one can calculate the variance of increments $X_{t+\tau;t}$ as

$$\begin{aligned}\mathrm{Var}(X_{t+\tau;t}) &= \left\langle \left(\int_t^{t+\tau} \sqrt{D(X_s,s)}dB_s\right)^2 \right\rangle \\ &= \int_t^{t+\tau} \langle D(X_s,s)\rangle ds \\ &= \frac{\langle D(u)\rangle}{2H}[(t+\tau)^{2H} - t^{2H}] \xrightarrow{t\gg\tau} \langle D(u)\rangle \tau t^{2H-1},\end{aligned} \tag{1.7}$$

where in the second equality we used Itō's isometry $\mathbb{E}\left[\left(\int_0^T X_t\,\mathrm{d}B_t\right)^2\right] = \mathbb{E}\left[\int_0^T X_t^2\,\mathrm{d}t\right]$.

It can be seen that this variance explicitly depends on t, which indicates the increments are non-stationary (unless $H = \frac{1}{2}$). Therefore, in the empirical analysis, the use of sliding interval methods is invalid and ensemble average is required.

Notice that by definition (1.3), a scaling process will satisfy $X_0 = 0$ with probability 1. The distribution of increments from 0 to t, $W(x, t; 0)$, is the same as the transition density $p_2(x, t|0, 0)$ [29], which represents the probability density of X_t given the condition that $X_0 = 0$, and it will satisfy Fokker-Planck equation

$$\frac{\partial}{\partial t} W(x, t; 0) = \frac{1}{2} \frac{\partial^2}{\partial t^2} [D(X_t, t) W(x, t; 0)]. \tag{1.8}$$

Note that this can be also reasoned by the 1-to-1 correspondence of SDE $dX_t = \sqrt{D(X_t, t)} dB_t$ and Fokker-Planck equation (this also explains why we ususally write $\sigma = \sqrt{D}$ in SDE (1.1))[30, 31]. Given the scaling form of distribution (1.4) and diffusion coefficient (1.5), one can obtain a relation between scaling function $F(u)$ and scaled diffusion coefficient $D(u)$ [24, 25]

$$F(u) = \frac{C}{D(u)} \exp\left(-2H \int \frac{u du}{D(u)}\right). \tag{1.9}$$

Now consider an expansion of $D(u)$ in u

$$D(u) = D_0 \left(1 + \varepsilon_1 |u| + \varepsilon_2 u^2 + \mathcal{O}(|u|^3)\right). \tag{1.10}$$

It can be shown [24, 25] that following correspondences between $F(u)$ and $D(u)$

- $D(u) = 1, F(u) = \exp\left(-\frac{1}{2} u^2\right)$
- $D(u) = (1 + \varepsilon_2 u^2), F(u) = (1 + \varepsilon_2 u^2)^{-\left(1 + \left(\frac{1}{2\varepsilon_2}\right)\right)}$

- $D(u) = D_0(1+\varepsilon|u|), F(u) = \frac{\varepsilon\alpha^\alpha \mathrm{e}^\alpha}{2\Gamma(\alpha,\alpha)}(1+\varepsilon|u|)^{\alpha-1}\mathrm{e}^{-\varepsilon\alpha|u|}$, where $\alpha = \frac{2H}{D_0\varepsilon^2}$, and $\Gamma(s,x) = \int_x^\infty t^{s-1}\mathrm{e}^t dt$

- $D(u) = D_0(1+\varepsilon_1|u|+\varepsilon_2 u^2)$,
  $F(u) = \frac{C}{D_0}\left(1+\varepsilon_1|u|+\varepsilon_2 u^2\right)^{-1-\frac{H}{D_0\varepsilon_2}} \exp\left(\frac{2H\varepsilon_1 \arctan\left(\frac{2\varepsilon_2|u|+\varepsilon_1}{\sqrt{4\varepsilon_2-\varepsilon_1^2}}\right)}{D_0\varepsilon_2\sqrt{4\varepsilon_2-\varepsilon_1}}\right)$

Note that in the last case, where $D(u) = D_0(1+\varepsilon_1|u|+\varepsilon_2 u^2)$, the corresponding $F(u)$ has a power law tail, because $\arctan(x)$ is bounded if x is real, and $\arctan(x) = \frac{1}{2}i\left(\ln(1-ix) - \ln(1+ix)\right)$ if x is imaginary. So in order to get a bi-exponential tail of $F(u)$, we must have

$$D(u) = D_0(1+\varepsilon|u|). \tag{1.11}$$

The asymptotic bi-exponential distribution of $F(u)$ is reported in empirical studies [17, 16, 14, 19].

By fixing the form of (1.11) and corresponding

$$F(u) = \frac{\varepsilon\alpha^\alpha \mathrm{e}^\alpha}{2\Gamma(\alpha,\alpha)}(1+\varepsilon|u|)^{\alpha-1}\mathrm{e}^{-\varepsilon\alpha|u|}, \tag{1.12}$$

one can calculate the analytical form of $\langle D(u)\rangle = \int_{-\infty}^{\infty} D(u)F(u)du$
$= \frac{D_0^2\varepsilon^2\Gamma(1+\alpha,\alpha)}{2H\Gamma(\alpha,\alpha)}$, where $\alpha = \frac{2H}{D_0\varepsilon^2}$. This also fixes the analytical form of variance of increments $X_{t+\tau;t}$ according to (1.7), and in the limit of $\tau \ll t$, it goes to $\langle D(u)\rangle \tau t^{2H-1}$, which scales with the same exponent as $D(X_t,t)$.

Another quantity that can be obtained analytically is the moments of increments

$$\left\langle X_{t+\tau;t}^\beta \right\rangle^{\frac{1}{\beta}} \sim t^{H-\frac{1}{2}}, \tag{1.13}$$

which can be evaluated [14] by using Itō's calculus in the condition of scaling form of (1.5) and variable diffusion SDE (1.6), and taking the limit of $\tau \ll t$. This quantity is useful in empirical analysis in that it provides an alternative way to confirm the validity of scaling (in contrast to multi-scaling [32, 33, 34, 35]) of empirical time series, as discussed below.

1.5 Empirical Analysis and Parameter Estimation

In order to get an empirical drift-free process, we need to detrend return distributions. As discussed in [29, 21], detrending of empirical time series can be non-trivial. In the case of currency markets, the mean is nearly constant during the day. However, in the stock prices, this is not true (for example, see Figure 3.1). Nevertheless, the best that can be done empirically is to remove the ensemble mean $\mathbb{E}[X_t]$ from the log return, and thus detrend all increments empirically.

Since the assumption of stationary increments is not valid in general, one has to calculate almost all statistical quantities by using the ensemble average. The ensemble consists of the daily variations in the return. For example, to extract the sample variance of increments from t to $t+\tau$, one has to calculate

$$\langle X^2_{t+\tau;t} \rangle = \frac{1}{N} \sum_{k=1}^{N} X^2_{t+\tau;t}(k), \tag{1.14}$$

where $X_{t+\tau;t}(k)$ is the increment from t to $t+\tau$ of the k-th day, and N is the number of trading days, with $\tau = 10$ minutes.

Empirically, the best evidence for scaling is a data collapse of the form (1.4).

However, due to the limited amount of empirical data, the collapse cannot be observed definitely for all cases. The next best but weaker evidence is to look for scaling in a finite number of the moments $\left\langle X_{t;0}^{\beta} \right\rangle^{\frac{1}{\beta}}$ [28], or to avoid the sensitivity in the beginning of scaling time interval, look for scaling in (1.13) where $\tau = 10$ minutes.

Parameters H, D_0, and ε in the linear variable diffusion model (1.6) with (1.11) are estimated as follows: the Hurst exponent H can be estimated by linear fit of the power law scale of $\mathrm{Var}(X_{t+\tau;t}) \sim t^{2H-1}$. The other two parameters can be estimated by fit of distribution $F(u)$ (1.12).

Finally, to empirically and numerically explore volatility clustering, one needs to evaluate the autocorrelation function of absolute and squared increments. The ensemble-averaged autocorrelation of increments is defined as

$$\mathcal{A}_{X_{t+\tau;t}}(t_1, t_2; \tau) = \frac{\left\langle \left(X_{t_1+\tau;t_1} - \langle X_{t_1+\tau;t_1} \rangle\right) \left(X_{t_2+\tau;t_2} - \langle X_{t_2+\tau;t_2} \rangle\right) \right\rangle}{\sigma(X_{t_1+\tau;t_1}) \sigma(X_{t_2+\tau;t_2})}, \tag{1.15}$$

where σ is the square root of variance (1.14), and is often called the volatility. By its definition, ensemble-averaged autocorrelation can depend on both t_1 and t_2 in general. The ensemble-averaged autocorrelations of absolute and squared increments are simply

$$\mathcal{A}_{|X_{t+\tau;t}|}(t_1, t_2; \tau) = \frac{\left\langle \left(|X_{t_1+\tau;t_1}| - \langle |X_{t_1+\tau;t_1}| \rangle\right) \left(|X_{t_2+\tau;t_2}| - \langle |X_{t_2+\tau;t_2}| \rangle\right) \right\rangle}{\sigma(|X_{t_1+\tau;t_1}|) \sigma(|X_{t_2+\tau;t_2})|} \tag{1.16}$$

and

$$\mathcal{A}_{X^2_{t+\tau;t}}(t_1, t_2; \tau) = \frac{\left\langle \left(X^2_{t_1+\tau;t_1} - \langle X^2_{t_1+\tau;t_1} \rangle\right) \left(X^2_{t_2+\tau;t_2} - \langle X^2_{t_2+\tau;t_2} \rangle\right) \right\rangle}{\sigma(X^2_{t_1+\tau;t_1}) \sigma(X^2_{t_2+\tau;t_2})}. \tag{1.17}$$

The sliding interval autocorrelation is defined as

$$\mathcal{A}^{slide}_{X_{t+\tau;t}}(t_2 - t_1; \tau) = \frac{\left\langle \left(X_{t_1+\tau;t_1} - \langle X_{t_1+\tau;t_1} \rangle_{t_1}\right) \left(X_{t_2+\tau;t_2} - \langle X_{t_2+\tau;t_2} \rangle_{t_2}\right) \right\rangle_{t_1}}{\sigma(X_{t+\tau;t})^2}, \tag{1.18}$$

where $\langle\cdot\rangle_t$ denotes the time average over t by the sliding interval method, and the σ is also calculated by the sliding interval method. This autocorrelation only depends on the difference $t_2 - t_1$ by construction, and it relies on the assumption of stationary increments.

Bibliography

[1] J. O'Farrell, An Utterly Impartial History of Britain, or, 2000 Years of Upper-class Idiots in Charge, Doubleday, London, UK, 2007.

[2] A. Chakraborti, I. M. Toke, M. Patriarca, F. Abergel, Econophysics review: I. empirical facts, Quantitative Finance 11 (7) (2011) 991–1012.

[3] A. Chakraborti, I. M. Toke, M. Patriarca, F. Abergel, Econophysics review: II. agent-based models, Quantitative Finance 11 (7) (2011) 1013–1041.

[4] F. Black, M. Scholes, Pricing of options and corporate liabilities, Journal of Political Economy 81 (3) (1973) 637–654.

[5] R. C. Merton, Theory of rational option pricing, Bell Journal of Economics 4 (1) (1973) 141–183.

[6] B. Mandelbrot, The variation of certain speculative prices, Journal of Business 36 (4) (1963) 394–419.

[7] U. A. Müller, M. M. Dacorogna., R. B. Olsen, O. V. Pictet, M. Schwarz Z, C. Morgenegg, Statistical study of foreign-exchange rates, empirical-evidence

of a price change scaling law, and intraday analysis, Journal of Banking and Finance 14 (6) (1990) 1189–1208.

[8] P. Gopikrishnan, V. Plerou, L. A. N. Amaral, M. Meyer, H. E. Stanley, Scaling of the distribution of fluctuations of financial market indices, Physical Review E 60 (5) (1999) 5305–5316.

[9] S. Galluccio, G. Caldarelli, M. Marsili, Y. C. Zhang, Scaling in currency exchange, Physica A: Statistical Mechanics and its Applications 245 (3-4) (1997) 423–436.

[10] N. Vandewalle, M. Ausloos, Multi-affine analysis of typical currency exchange rates, European Physical Journal B 4 (2) (1998) 257–261.

[11] P. Gopikrishnan, V. Plerou, Y. Liu, L. A. N. Amaral, X. Gabaix, H. E. Stanley, Scaling and correlation in financial time series, Physica A: Statistical Mechanics and its Applications 287 (3-4) (2000) 362–373.

[12] M. M. Dacorogna, U. A. Müller, R. J. Nagler, R. B. Olsen, P. O. V., A geographical model for the daily and weekly seasonal volatility in the foreign-exchange market, Journal of International Money and Finance 12 (4) (1993) 413–438.

[13] B. Zhou, High-frequency data and volatility in foreign-exchange rates, Journal of Business and Economic Statistics 14 (1) (1996) 45–52.

[14] K. E. Bassler, J. L. McCauley, G. H. Gunaratne, Nonstationary increments, scaling distributions, and variable diffusion processes in financial markets, Proceedings of the National Academy of Sciences 104 (44) (2007) 17287–17290.

[15] J. L. McCauley, Time vs. ensemble averages for nonstationary time series, Physica A: Statistical Mechanics and its Applications 387 (22) (2008) 5518–5522.

[16] L. Seemann, J. L. McCauley, G. H. Gunaratne, Intraday volatility and scaling in high frequency foreign exchange markets, International Review of Financial Analysis 20 (3) (2011) 121–126.

[17] L. Seemann, J.-C. Hua, J. L. McCauley, G. H. Gunaratne, Ensemble vs. time averages in financial time series analysis, Physica A: Statistical Mechanics and its Applications 391 (23) (2012) 6024–6032.

[18] J. L. McCauley, K. E. Bassler, G. H. Gunaratne, Martingales, the efficient market hypothesis, and spurious stylized facts, arXiv:0710.2583.

[19] J.-C. Hua, L. Chen, J. L. McCauley, G. H. Gunaratne, Variable diffusion model for stock markets, (In preparation).

[20] F. Abergel, A. Jedidi, A mathematical approach to order book modeling, International Journal of Theoretical and Applied Finance 16 (05) (2013) 1350025.

[21] J. L. McCauley, K. E. Bassler, G. H. Gunaratne, Martingales, detrending data, and the efficient market hypothesis, Physica A: Statistical Mechanics and its Applications 387 (1) (2008) 202–216.

[22] K. E. Bassler, G. H. Gunaratne, J. L. McCauley, Empirically based modeling in financial economics and beyond, and spurious stylized facts, International Review of Financial Analysis 17 (5) (2008) 767–783.

[23] K. E. Bassler, G. H. Gunaratne, J. L. McCauley, Markov processes, Hurst exponents, and nonlinear diffusion equations: with application to finance, Physica A: Statistical Mechanics and its Applications 369 (2) (2006) 343–353.

[24] A. L. Alejandro-Quiñones, K. E. Bassler, M. Field, J. L. McCauley, M. Nicol, I. Timofeyev, A. Török, G. H. Gunaratne, A theory of fluctuations in stock prices, Physica A: Statistical Mechanics and its Applications 363 (2) (2006) 383–392.

[25] G. H. Gunaratne, J. L. McCauley, M. Nicol, A. Török, Variable step random walks and self-similar distributions, Journal of Statistical Physics 121 (5-6) (2005) 887–899.

[26] P. Embrechts, Selfsimilar Processes, Princeton University Press, Princeton, NJ, 2009.

[27] B. Mandelbrot, J. W. van Ness, Fractional Brownian motions, fractional noises and applications, SIAM Review 10 (4) (1968) 422–437.

[28] J. L. McCauley, G. H. Gunaratne, K. E. Bassler, Hurst exponents, Markov processes, and fractional Brownian motion, Physica A: Statistical Mechanics and its Applications 379 (1) (2007) 1–9.

[29] J. L. McCauley, Dynamics of Markets: The New Financial Economics, Cambridge University Press, Cambridge, UK, 2009.

[30] J. L. McCauley, Stochastic Calculus and Differential Equations for Physics and Finance, Cambridge University Press, Cambridge, UK, 2013.

[31] J. L. McCauley, Fokker-Planck and Chapman-Kolmogorov equations for Ito processes with finite memory, in: A. T. Skjeltorp, A. V. Belushkin (Eds.), Evolution from Cellular to Social Scales, NATO Science for Peace and Security Series B: Physics and Biophysics, Springer Netherlands, 2008, pp. 99–110.

[32] T. Di Matteo, Multi-scaling in finance, Quantitative Finance 7 (1) (2007) 21–36.

[33] S. Ghosh, P. Manimaran, P. K. Panigrahi, Characterizing multi-scale self-similar behavior and non-statistical properties of financial time series, Physica A: Statistical Mechanics and its Applications 390 (23-24) (2011) 4304–4316.

[34] F. Wang, K. Yamasaki, S. Havlin, H. Stanley, Multifactor analysis of multiscaling in volatility return intervals, Physical Review E 79 (1) (2009) 016103.

[35] F. Wang, K. Yamasaki, S. Havlin, H. E. Stanley, Indication of multiscaling in the volatility return intervals of stock markets, Physical Review E 77 (1) (2008) 016109.

Chapter 2

Ensemble vs. Time Averages in Financial Time Series Analysis

2.1 Introduction

Understanding the stochastic dynamics underlying financial markets has been a focus of physicists for around half a century. Early work by Osborne [1, 2] paved the path for Econophysics. Methods derived mainly from statistical physics are applied to assess the dynamics of financial time series. Important characteristics of a time series are its volatility as well as the distribution of increments and the autocorrelation. Several models have been proposed to explain financial time series (see, e.g., [3, 4] for a review). For example, the prominent Black and Scholes option pricing model [5, 6] assumed that the stochastic dynamics of the underlying asset was a geometric Brownian motion. However, later work revealed that the empirical distributions contain fat tails [7, 8, 9]. Studies also found that the distributions scale with the length of the time interval analyzed [10, 11, 12]. In addition, financial time series are characterized by their intraday "seasonality" [8, 13, 14].

The intraday volatility pattern of foreign exchange rates can be explained by hours of business in different geographical regions [14, 15, 16, 17]. Volatility (root mean square fluctuations), rate of transactions, and bid-ask spread, are highest during times when the European and North American markets are active. Ref.[18] analyzed intraday increments of the Euro-Dollar exchange rate and found several time intervals during the day where the standard deviation of increments exhibits power law behavior in time. Seemann et al.[17] extended the analysis of intraday scaling regions in foreign exchange markets and found similar scaling behavior in the Euro-Dollar, Dollar-Yen, and Sterling-Dollar markets.

Traditional analytical methods, which are predicated on stochastic processes with stationary increments, are not appropriate for assessing financial time series, because intraday volatility varies throughout a typical trading day. In particular, many statistical analyses of financial time series have been conducted applying sliding interval methods. An example is the finding that the distribution of returns scales with the time lag [19, 20, 21, 22]. However, sliding interval approaches implicitly assume that the underlying stochastic process has stationary increments. Empirical analysis invalidates this assumption [8, 14, 18].

Although the periodicity of intraday behavior has been noted [8, 13, 14], only recently have alternative approaches been discussed. Ensemble averages over the set of trading days have been proposed [23, 18, 17]. Immediately the following questions arise: How do results between time and ensemble averages differ? Assuming that the underlying dynamics of a time series are known a priori, which approach better characterizes the underlying dynamics of the stochastic process?

Since the dynamics underlying empirical financial data are not known, we construct and apply a model to produce time series with similar key characteristic as the empirical high-frequency foreign exchange data. The empirical data and the model exhibit intraday seasonality and we analyze differences of time averaging analysis and ensemble average analysis. The main finding of our work is that ensemble averaging techniques are able to assess the underlying dynamics correctly, whereas sliding interval approaches fail and moreover lead to spurious conclusions. We also find that the proposed intraday volatility model exhibits several stylized facts of foreign exchange time series.

2.2 Background

2.2.1 Foreign Exchange Data

For empirical analysis we used several years of tick by tick data of major exchange rates from Gain Capital. Before using the data we scrutinized the consistency and filtered ticks that were likely to be erroneous by applying a filtering window [24, 25]. We approximate the spot price p by the average of the bid and ask quotes: $p = (p_{bid} + p_{ask})/2$. For our analysis we used detrended increments by removing the time average over all available days. One problem is that a bid/ask pair is not recorded in every time interval of interest, e.g. both prices are needed in order to calculate the increment between the price at time t and (t+10) min. When one price is not available, the missing data are either linearly interpolated, or the last recorded value is used. Here, we take a strict approach and only analyze increments for which both trades are recorded, i.e., we omit all returns for which at least one of the prices is not known. Furthermore, we only considered trading days, i.e., we exclude data from weekends and holidays.

2.2.2 Definitions

Financial time series are stochastic processes. Their dynamics are described by the return $\log(P(t)/P_0)$, where $P(t)$ represents the price of a financial asset or contract, e.g., the Euro-Dollar exchange rate, and P_0 is a reference price. We assess the

underlying stochastic dynamics using increments of the return given by

$$X(\tau;t) \equiv \log P(t+\tau) - logP(t), \tag{2.1}$$

where we choose τ to be 10 min [18], since there are short-term correlations in financial time series. Note that $X(\tau;t)$ is dimensionless and additive. Also notice that the increments $X(\tau;t)$ may depend on both the time lag τ and time of the day t. The distribution of increments is denoted by $W(x,\tau;t)$. If the distribution $W(x,\tau;t)$ is independent of time t and only depends on τ, the process is said to have *s*tationary increments. Consider the prominent example of Geometric Brownian Motion (GBM): The distribution of increments only depends on the time difference τ and is independent of time t. The variance of GBM is linear in τ.

However, generally $W(x,\tau;t)$ can depend on t and $W(x,\tau;t)$ can not be estimated by averaging over t (*s*liding interval methods). Here we apply ensemble averages over all trading days since the stochastic dynamics of foreign exchanges rates are approximately the same between trading days [18, 17]. For ensemble average analyses we remove the mean over all trading days and define the volatility of stochastic dynamics as the root mean square (rms) fluctuations

$$\sigma(\tau;t) \equiv \sqrt{\langle X(\tau;t)^2 \rangle}, \tag{2.2}$$

where $\langle X(\tau;t)^2 \rangle$ is averaged over N trading days:

$$\langle X(\tau;t)^2 \rangle = \frac{1}{N} \sum_{k=1}^{N} X_k^2(\tau;t) \tag{2.3}$$

with $\tau = 10$ min.

We will show that the stochastic dynamics of financial processes are memoryless as their autocorrelation function decays rapidly. This observation strongly suggests

that the underlying dynamics are Markovian and that the time evolution of $W(x, \tau; t)$ is described by the diffusion equation with diffusion coefficient $D(x, \tau)$

$$\frac{\partial}{\partial \tau} W(x, \tau; 0) = \frac{1}{2} \frac{\partial}{\partial x^2} [D(x, \tau) W(x, \tau; 0)] \tag{2.4}$$

which is drift-free since $X(t; \tau)$ has been detrended.

2.2.3 Scaling

The volatility of stochastic processes underlying financial market fluctuations exhibits scaling. The three most actively traded currency pairs exhibit three scaling intervals during the day during which the root mean square fluctuations scale as power laws [18, 17]:

$$\sigma^2(t; 0) = \int_{-\infty}^{\infty} x(t; 0)^2 W(x, t; 0) dx = c t^{2H}, \tag{2.5}$$

where H is the Hurst exponent.

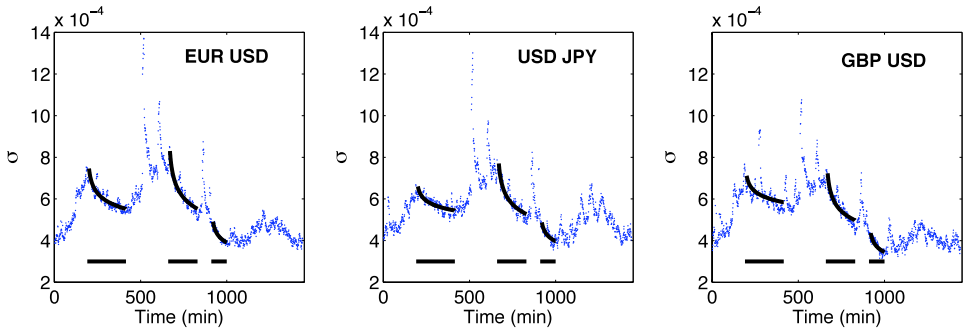

Figure 2.1: Intraday volatility behavior defined as the root mean square fluctuations of increments averaged over the years studied (Eq.2.2). Intraday increments are nonstationary in all three markets and exhibit similar scaling behavior. The scaling regions are indicated by horizontal bars. We found similar intraday seasonality in most actively traded foreign exchange rates.

The Hurst exponent is different for each interval but independent of the currency pair under study (Fig.2.1). This suggests that the distribution function scales according to

$$W(x,\tau;0) = \tau^{-H} F(u) \tag{2.6}$$

where the scaling variable u is defined by $u = \frac{x}{\tau^H}$. Itō's calculus requires the diffusion coefficient to scale as well in order to get Eq.2.5 [26, 27]

$$D(x,\tau) = \tau^{2H-1} D(u). \tag{2.7}$$

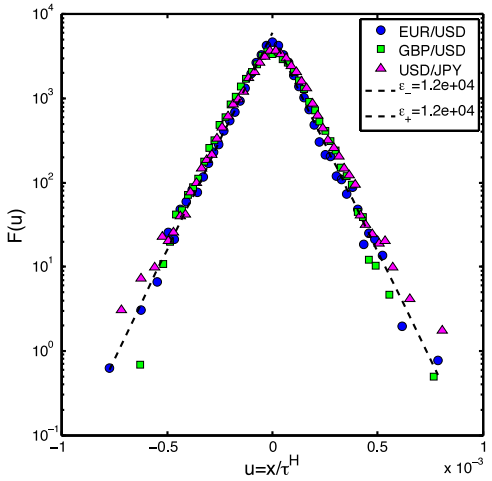

Figure 2.2: The scaling function $F(u)$ for the longest scaling interval from 190 min - 415 min GMT for all three currency pairs studied. The scaling function appears to be biexponential and identical for the three currency pairs under study. Evaluation of the other two scaling regions also shows the same scaling behavior for all three exchange rates. The scaling function F(u) was estimated through histograms with variable bin size. Each bin has a width of at least 2.5×10^{-5} and contains at least 15 observations.

Using high-frequency foreign exchange data we can extract the empirical scaling function F. We apply Eq.2.6 for different τ on each scaling region to estimate F, which is found to be approximately bi-exponential (Fig.2.2).

2.2.4 Autocorrelation

We also assess the autocorrelation. The autocorrelation of absolute increments is defined as

$$\mathcal{A}_{abs}(t_1, t_2; \tau) = \frac{\langle |X(t_1, \tau) - \langle X(t_1, \tau)\rangle| \; |X(t_2, \tau) - \langle X(t_2, \tau)\rangle| \rangle}{\sigma(\tau; t_1)\sigma(\tau; t_2)} \tag{2.8}$$

and the autocorrelation of squared increments as

$$\mathcal{A}_{sq}(t_1, t_2; \tau) = \frac{\langle (X(t_1; \tau) - \langle X(t_1; \tau)\rangle)^2 \, (X(t_2; \tau) - \langle X(t_2; \tau)\rangle)^2 \rangle}{\sigma(\tau; t_1)\sigma(\tau; t_2)}. \tag{2.9}$$

The average is to be understood as an ensemble average over trading days according to Eq.2.3 and the variance is defined as in Eq.2.2. If the increments are stationary, i.e., they are a function of τ only, the ensemble averages can be replaced with time averages. This yields to the more common definition of the autocorrelation coefficient [28]. The autocorrelation of absolute or squared increments decays slowly and studies suggest that the decay follows a power law [29, 28]. It implies that large fluctuations are more likely to be followed by large fluctuations, and the fact is coined "volatility clustering" [7]. Also characteristic is the 24-hour peak in absolute or squared increments, which is a reflection of the daily repetition of the stochastic process underlying the markets [13].

2.3 Intraday Volatility Model

2.3.1 Variable Diffusion Processes

The empirically observed scaling behavior can be modeled using variable diffusion processes. Using both scaling forms for distribution (Eq.2.6) and for the diffusion coefficient (Eq.2.7) in the diffusion equation (Eq.2.4) allows us to calculate the scaling function analytically

$$F(u) = \frac{C}{D(u)} \exp\left[-\frac{2H}{D_0}\int_0^u \frac{\tilde{u}}{1+\varepsilon|\tilde{u}|}d\tilde{u}\right], \tag{2.10}$$

where C is the normalization constant. Consider a diffusion process initiated at zero that scales according to Eq.2.7. Expansion of $D(u)$ in u results in

$$D(u) = D_0\left(1+\varepsilon_1|u|+\varepsilon_2 u^2+\mathcal{O}(|u|^3)\right) \tag{2.11}$$

where we assumed symmetry in u which is justified by the symmetry in the distribution of returns in financial markets [30, 31]. It can be shown that a linear expression for the diffusion rate gives rise to a bi-exponential scaling function[1]. Hence we will consider

$$D(x,\tau) = D_0\tau^{2H-1}(1+\varepsilon|u|). \tag{2.12}$$

Using this first order term in Eq.2.10 yields after integration and normalization

$$F(u) = \frac{\varepsilon\alpha^\alpha e^{-\alpha}}{2\Gamma(\alpha,\alpha)}(1+\varepsilon|u|)^{\alpha-1}e^{-\varepsilon\alpha|u|}, \tag{2.13}$$

where $\alpha \equiv \frac{2H}{D_0\varepsilon^2}$ and $\Gamma(s,x) \equiv \int_x^\infty t^{s-1}e^{-t}\,dt$ is the upper incomplete Gamma function.

[1] E.g., if $D(u)=1$ we get $F(u) = exp(-\frac{1}{2}u^2)$ (Gaussian) and $D(u) = 1+\varepsilon_2 u^2$ yields $F(u) = (1+\varepsilon_2 u^2)^{-(1+\frac{1}{2\varepsilon_2})}$

Note that in the special case $D_0 = \frac{2H}{\varepsilon^2}$, the scaling function F(u) is bi-exponential and and has the form $F(u) = \frac{\varepsilon}{2} e^{-\varepsilon|u|}$. The case $\varepsilon \to 0$ gives a Gaussian scaling function as can be seen from Eq.2.10.

2.3.2 Scaling Regions

We use our intraday volatility model to generate a time series generated by repetition of the intraday stochastic process. Each model trading day comprises of six scaling regions that approximately replicate the activity pattern exhibited in foreign exchange markets (Fig.2.3). Each scaling regions obeys $\sigma^2(t;0) = ct^{2H}$ (Eq.2.5). The volatility at the beginning and at end of the trading day are set equal as required for the continuity of the characteristics of the stochastic process.

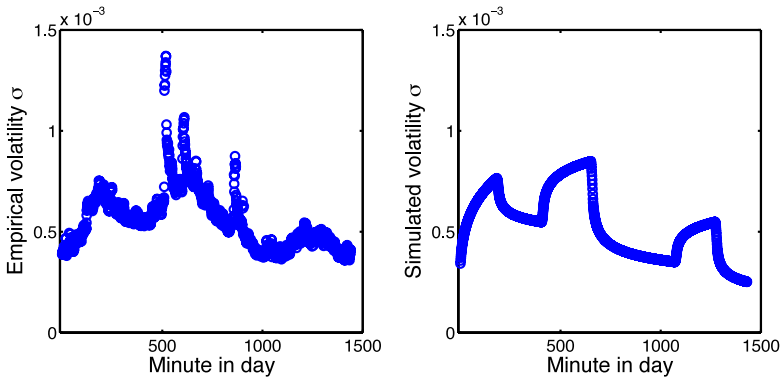

Figure 2.3: Empirical and modeled intraday volatility patterns. Every trading day exhibits three waves of volatility. After the European markets open, the North-American markets become active. Lastly the Tokyo markets open. The activity is highest when European and North-American markets are open.

2.3.3 Parameter Estimation

The model parameters can be estimated empirically using high-frequency foreign exchange data. Each scaling region in our model is simulated using a variable diffusion process (Eq.2.13). Three parameters need to be estimated for each scaling region: the Hurst exponent H and the parameters ε and D_0. The Hurst exponent H is given by the empirical scaling of the volatility. The parameters ε and D_0 are related through $D_0\varepsilon^2 = 2H$ because the empirical scaling function $F(u)$ is bi-exponential, hence $\alpha = 1$ (Eq.2.13, Fig.2.2). Within each scaling region ε can be estimated by the tail exponent of $F(u)$ (Fig.2.2). Table 2.1 summarizes the parameter estimates. We want to emphasize that our aim is not to fit the intraday seasonality pattern but to build a continuous intraday volatility model that contains three regions of high activity (Fig.2.3), which correspond to opening hours in Europe, America, and Japan. Although we estimated our parameters based on empirical data, the results presented below do not depend on the particular set of parameters.

Table 2.1: Model parameters according to Eqs.2.12 and 2.13. The scaling intervals are described in minutes since the start of the trading day.

Scaling interval	α	H	ε
0-190	1	0.714	21382
190-415	1	0.437	5435
415-660	1	0.579	8750
660-1080	1	0.353	4421
1080-1280	1	0.585	13823
1280-1440	1	0.345	6754

2.4 Results

2.4.1 Scaling

Each trading day in our simulation contains six scaling regions. To assess if and how the distribution of increments of our model data scales, we determined the scaling function $F(u)$ for each scaling interval individually. $F(u)$ is calculated using Eq.2.6 with the Hurst exponents given in Table 2.1. We use multiple values of τ, whereas τ is a multiple of 10 and smaller than the length of the scaling interval. Note that according to Eq.2.6 time t is set to zero at the beginning of each scaling region. Results indicate that for each scaling region the rescaled distributions of increments collapse into one scaling function (Fig.2.4A). The results indicate consistency between the

model and empirical data within each scaling region. The scaling function for each scaling interval agrees with the theoretical calculations according to Eq.2.13 (shown as dashed lines).

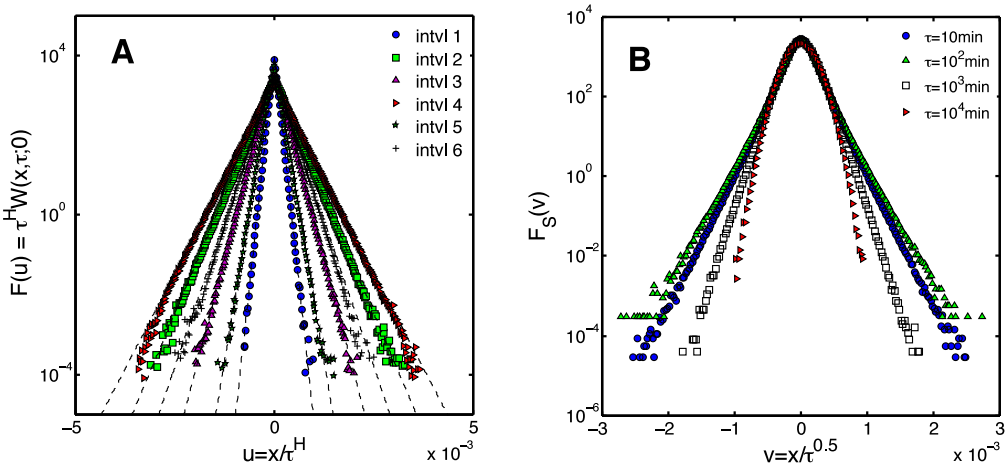

Figure 2.4: Collapse of the distribution function of increments. (**A**) Analysis of model data illustrating the correct detection of the underlying dynamics. The scaling function $F(u)$ is calculated for each scaling interval and compared with the expected result from Eq. 2.13 (dashed line). The empirical data agree with the model. (**B**) Applying time averaging sliding windows on the same time series yields to spurious results. Although the center of the distribution seems to scale well, the tails indicate that the distributions do not collapse. Note short time lags result in scaling distributions with wide tails, whereas bigger time lags result in distributions which appear to be parabolic. This finding agrees with reports that with increasing time lag the empirical return distribution converges to Gaussian behavior [9]. The results shown are from analyzing 10^8 modeled trading days.

Since financial time series analyses is mostly conducted using sliding interval methods, we also calculate the scaling function using non overlapping sliding intervals of different length. Sliding interval methods average the return distribution over time

$$W_S(x,\tau) \equiv \langle W(x,\tau;t)\rangle_t, \tag{2.14}$$

where $\langle\cdot\rangle_t$ indicates the time average, and thereby assume stationary increments. Many studies applying these sliding interval techniques report scaling with a Hurst exponent of $H_S \approx 0.5$. That motivated us to assess our model dynamics using sliding intervals using $H_S = 0.5$ and different interval length. We found that the rescaled distributions of increment do not collapse in the tails whereas the center of the distributions might suggest scaling (Fig.2.4B). Note that we simulated 10^8 trading days to emphasize differences of the distribution in the tails. Real world data will provide much smaller samples and hence the differences will not be as significant as shown here. Although the center of the rescaled distributions of return seem to scale well with $H_S = 0.5$, our results indicate that time averaging does not allow to deduce the underlying dynamics correctly. We also observed that the shape of the rescaled return distribution change qualitatively. Note that for lags bigger than 10^3 min (corresponding to lags longer than one trading days) the rescaled distribution shape becomes parabolic, indicating a scaling function closer to a normal distribution.

2.4.2 Autocorrelation

Similarly to the return distribution, the autocorrelation in most studies is assessed using sliding intervals. First, we determined our model's behavior when analyzed

using a sliding interval technique.

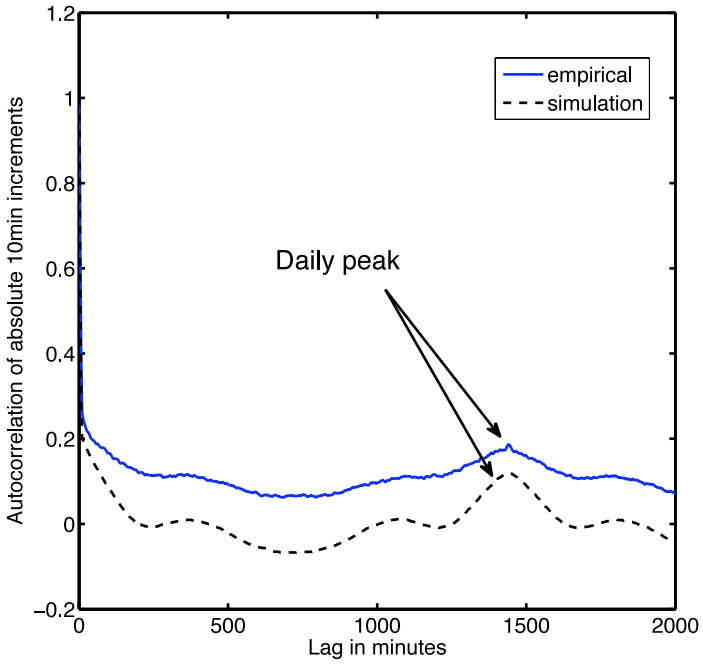

Figure 2.5: Autocorrelation of absolute increments calculated classically using a sliding window. The autocorrelation of absolute increments of the model data reproduces the characteristic daily peak, which arises from the daily repetition of the stochastic process underlying financial markets.

Similar to empirical foreign exchange data, our model results in a slowly decaying autocorrelations of square increments. Time lags below 200 min result in significant correlations (Fig 2.5). The daily peak is also reproduced. It results from the periodic intraday behavior. These results suggest that our model reproduces characteristic behavior of foreign exchange autocorrelations.

We also assess the model data using an ensemble of trading days because the assumptions for sliding interval techniques are not met, as discussed above. Hence assessment of the autocorrelation using ensemble averages according to Eqs.2.8,2.9 are appropriate. However, the scaling intervals are short and do not allow assessing the long term behavior of the autocorrelation of increments for variable diffusion processes. Therefore, we also investigate the dynamics of variable diffusion processes according to Eq.2.12 individually. The results illustrated in Fig.2.6A show that variable diffusion processes produce time series with long term autocorrelation of absolute (not shown here) and squared increments. Using an ensemble average according to Eq.2.9, we found that the autocorrelation of squared and absolute increments of variable diffusion processes decays slowly. Earlier studies of similar variable diffusion processes reported power law decays according to $T^{\varepsilon-1}$[32]. Here we did not find a linear relationship between the parameters ε and H (Fig.2.6B).

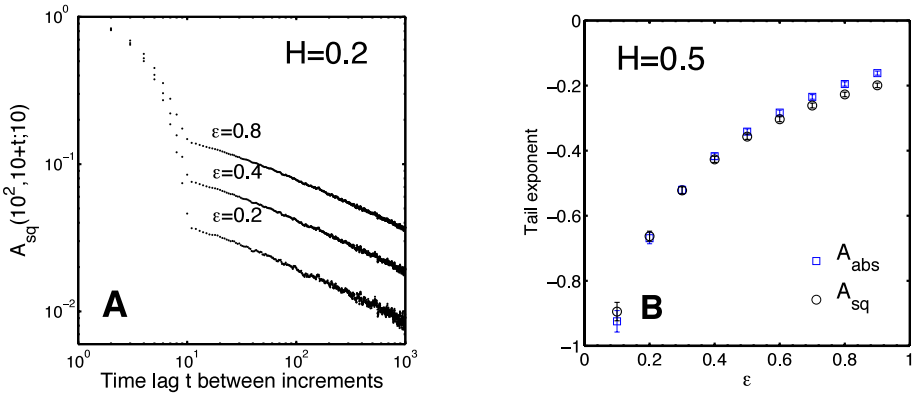

Figure 2.6: Autocorrelation of squared increments calculated through an ensemble according to Eq.2.9 (**A**) The autocorrelation of squared increments of variable diffusion processes is slowly decaying. Shown are the long term correlations for constant Hurst exponent H and different ε. Because the increments are calculated using a time lag of 10, a time lag of less than 10 between increments results in overlapping increments, which results in large correlations. Hence the significant autocorrelation values for squared increments for time lags less than 10. (**B**) Estimating the relationship between the parameters of the variable diffusion process and the long term behavior of the autocorrelation of squared increments, the exponent capturing the slow decay. For all Hurst exponents we studied ($0 < H \leq 1$) the slope in the log-log plot (Fig.A) is not a linear function of ε, as it was reported for variable diffusion processes with $D(u) = 1 + \varepsilon \frac{x^2}{t}$ [32]. Shown here is the non-linear behavior for $H = 0.5$.

2.5 Discussion and Conclusions

Our findings emphasize the need to design analytical techniques for financial time series that allow for the stochastic process to have non-stationary increments. Here we explicitly showed that traditional sliding interval methods, which implicitly assume that the increments are stationary, give rise to spurious findings. In particular we analyzed the scaling function of returns and the autocorrelation of processes with non-stationary increments using time averaging techniques and were not able to deduce the true underlying dynamics. In contrast, ensemble averages over trading days yielded the underlying model dynamics correctly.

Financial time series exhibit strong intraday seasonality. Our analysis of intraday volatility of foreign exchange data, whose characteristic pattern is explained by opening hours of the global financial centers, is in agreement with earlier findings [13, 14]. Our work expands earlier findings as we found that the intraday volatility patterns are similar between different markets and exhibit scaling regions.

The intraday volatility pattern is evidence for non-stationary increments of the underlying stochastic process, which is in contradiction with the assumption of stationary increments needed for time averaging techniques. Several approaches have been suggested to overcome this problem. One set of approaches redefines "time" in the stochastic process. Instead of using physical time, other time measures have been proposed that are based on characteristic financial events [33, 34, 35, 3, 4]. Oomen [34] reports advantages in using transaction time, which increases by one unit for each reported transaction. Tick time increases time by one unit for each

price change [35, 3, 4]. Another approach suggested by Dacorogna et al. introduces ϑ-time which accounts for the seasonal intraday and intra-week aspect of volatility [13, 25].

Fig.2.7 suggests that using event-based transaction time results in time series with approximately stationary increments during active markets. The intraday behavior of the average number of ticks is similar to that of volatility; moreover, they peak at the same time, leading to an intuitive conclusion that the price fluctuations increase with a higher trading frequency. Additional evidence for this assertion was made previously [36, 37, 38], where it was found that in an event-based ε time scale defined by local extreme values in price, the volatility of price, trading volume, and frequency of trading (equivalently, the number of ticks per unit time) peak at the same time, which is the end of an interval during which the price exhibits an increasing or decreasing trend, corresponding to local extreme values in the price.

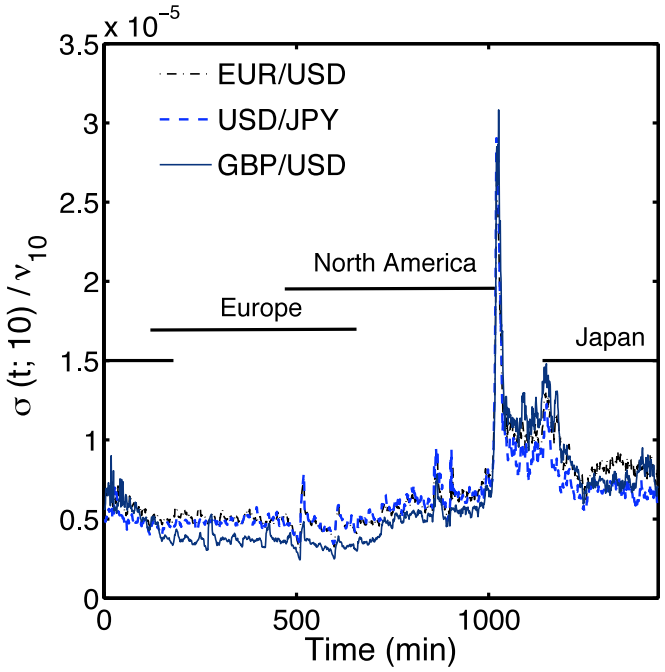

Figure 2.7: Volatility per tick. Dividing the intraday volatility $\sigma(t;10)$ (see Fig.2.1) by the number of ticks ν_{10} within the same 10min intervals reveals an almost constant ratio during active trading in the three main financial centers. The aberrant behavior between 1000 and 1200 minutes coincides with the time interval during the day at which the three main markets are closed.

However, when applying sliding interval techniques to event-based or rescaled time, the assumption of stationary increments needs to be verified for the rescaled time series as well. It is not clear that the rescaled times series result in processes with stationary increments. For example, Fig.2.7 indicates that event-based transaction time results in time series with non-stationary increments when the main markets are closed. Our ensemble averages provides an alternative by averaging over trading

days; here, the assumption of non-stationary increments is not needed.

Here we introduced a model that decomposes the intraday volatility into the three main continental markets. Each modeled volatility interval scales in time as suggested by empirical studies of foreign exchange data. It can be regarded as an extension of the polynomial volatility model introduced in [13].

The time series of our model was assessed using both time averages and ensemble averages. As the underlying dynamics of our model are known, we were able to compare the results of both approaches. We determined the distribution of returns and its scaling and found that only the ensemble averages correctly determines the underlying dynamics.

The autocorrelation function of our model exhibits stylized facts reported in previous empirical studies. Using time averages our model reproduced volatility clustering, i.e., the autocorrelation of squared and absolute increments decays slowly, as reported in [29, 28]. Our model also reproduced the characteristic high correlation between of absolute of squared increments that lag exactly one day [13, 25]. The peak is caused by repetition of the intraday intraday stochastic process.

We wish to emphasize that our conclusions do not depend on particular parameters used. Specifically, we found similar results when we chose a model with only four instead of six scaling regions. Our choice of parameters here was guided by empirical data from the most actively traded foreign exchange rates.

We analyzed the intraday volatility of the most actively traded exchange rates and found repeating behavior of intraday volatility. Although the empirical patterns

may differ from the particular pattern reported here (Fig.2.1), the presence of non-stationary increments implies that most foreign exchange rates should be analyzed using ensemble averages instead of time averages. Empirical studies of stocks have also reported non-stationary stochastic behavior [39, 40]. These include characteristic U-shaped patterns within the trading day [39, 40, 41]. We hypothesize that many, if not most, markets which are actively traded exhibit intraday seasonality and therefore also have non-stationary increments.

In summary, our work reveals that time average techniques are not appropriate to analyze time series with non-stationary increment, like foreign exchange data. Neither the scaling behavior of the returns nor the autocorrelations of an intraday activity model were identified correctly. However, repeating behavior of intraday activity/volatility allows to regard each detrended trading day as a repetition of the same experiment and average over an ensemble over trading days. That approach allowed us to infer the underlying dynamics correctly. Our results imply that analyzing financial time series which exhibit repeating behavior of activity via ensemble averages can be used to derive new insight into the underlying dynamics.

Bibliography

[1] M. F. M. Osborne, Brownian-motion in the stock market, Operations Research 7 (2) (1959) 145–173.

[2] M. F. M. Osborne, The Stock Market and Finance From a Physicist's Viewpoint, Crossgar Press, Minneapolis, 1977.

[3] A. Chakraborti, I. M. Toke, M. Patriarca, F. Abergel, Econophysics review: I. empirical facts, Quantitative Finance 11 (7) (2011) 991–1012.

[4] A. Chakraborti, I. M. Toke, M. Patriarca, F. Abergel, Econophysics review: II. agent-based models, Quantitative Finance 11 (7) (2011) 1013–1041.

[5] F. Black, M. Scholes, Pricing of options and corporate liabilities, Journal of Political Economy 81 (3) (1973) 637–654.

[6] R. C. Merton, Theory of rational option pricing, Bell Journal of Economics 4 (1) (1973) 141–183.

[7] B. Mandelbrot, The variation of certain speculative prices, Journal of Business 36 (4) (1963) 394–419.

[8] U. A. Müller, M. M. Dacorogna., R. B. Olsen, O. V. Pictet, M. Schwarz Z, C. Morgenegg, Statistical study of foreign-exchange rates, empirical-evidence of a price change scaling law, and intraday analysis, Journal of Banking and Finance 14 (6) (1990) 1189–1208.

[9] P. Gopikrishnan, V. Plerou, L. A. N. Amaral, M. Meyer, H. E. Stanley, Scaling of the distribution of fluctuations of financial market indices, Physical Review E 60 (5) (1999) 5305–5316.

[10] S. Galluccio, G. Caldarelli, M. Marsili, Y. C. Zhang, Scaling in currency exchange, Physica A: Statistical Mechanics and its Applications 245 (3-4) (1997) 423–436.

[11] N. Vandewalle, M. Ausloos, Multi-affine analysis of typical currency exchange rates, European Physical Journal B 4 (2) (1998) 257–261.

[12] P. Gopikrishnan, V. Plerou, Y. Liu, L. A. N. Amaral, X. Gabaix, H. E. Stanley, Scaling and correlation in financial time series, Physica A: Statistical Mechanics and its Applications 287 (3-4) (2000) 362–373.

[13] M. M. Dacorogna, U. A. Müller, R. J. Nagler, R. B. Olsen, P. O. V., A geographical model for the daily and weekly seasonal volatility in the foreign-exchange market, Journal of International Money and Finance 12 (4) (1993) 413–438.

[14] B. Zhou, High-frequency data and volatility in foreign-exchange rates, Journal of Business and Economic Statistics 14 (1) (1996) 45–52.

[15] U. A. Müller, M. M. Dacorogna, O. V. Pictet, R. R. Davé, D. M. Guillaume, From the bird's eye to the microscope: A survey of new stylized facts of the intra-daily foreign exchange markets, Finance Stochastics 1 (2) (1997) 95–129.

[16] T. Ito, Y. Hashimoto, Intraday seasonality in activities of the foreign exchange markets: Evidence from the electronic broking system, Journal of the Japanese and International Economies 20 (4) (2006) 637–664.

[17] L. Seemann, J. L. McCauley, G. H. Gunaratne, Intraday volatility and scaling in high frequency foreign exchange markets, International Review of Financial Analysis 20 (3) (2011) 121–126.

[18] K. E. Bassler, J. L. McCauley, G. H. Gunaratne, Nonstationary increments, scaling distributions, and variable diffusion processes in financial markets, Proceedings of the National Academy of Sciences 104 (44) (2007) 17287–17290.

[19] R. N. Mantegna, H. E. Stanley, Scaling behavior in the dynamics of an economic index, Nature 376 (6535) (1995) 46–49.

[20] R. N. Mantegna, H. E. Stanley, Turbulence and financial markets, Nature 383 (6601) (1996) 587–588.

[21] C. Renner, J. Peinke, R. Friedrich, Evidence of markov properties of high frequency exchange rate data, Physica A: Statistical Mechanics and its Applications 298 (3-4) (2001) 499–520.

[22] L. Borland, Option pricing formulas based on a non-gaussian stock price model, Physical Review Letters 89 (9) (2002) 098701.

[23] J. L. McCauley, Time vs. ensemble averages for nonstationary time series, Physica A: Statistical Mechanics and its Applications 387 (22) (2008) 5518–5522.

[24] C. T. Brownlees, G. M. Gallo, Financial econometric analysis at ultra-high frequency: Data handling concerns, Computational Statistics and Data Analysis 51 (4) (2006) 2232–2245.

[25] M. M. Dacorogna et al., An Introduction to High-Frequency Finance, Academic Press, San Diego, CA, 2001.

[26] L. Arnold, Stochastic Differential Equations: Theory and Applications, Krieger Pub Co, Malabar, FL, 1992.

[27] K. E. Bassler, G. H. Gunaratne, J. L. McCauley, Markov processes, hurst exponents, and nonlinear diffusion equations: With application to finance, Physica A: Statistical Mechanics and its Applications 369 (2) (2006) 343 – 353.

[28] R. Cont, G. Teyssière, A. Kirman, Volatility clustering in financial markets: Empirical facts and Agent-based models, Springer Berlin Heidelberg, 2007, pp. 289–309.

[29] Y. Liu, P. Cizeau, M. Meyer, C. K. Peng, H. Eugene Stanley, Correlations in economic time series, Physica A: Statistical Mechanics and its Applications 245 (3-4) (1997) 437–440.

[30] J. McCauley, G. Gunaratne, An empirical model of volatility of returns and option pricing, Physica A: Statistical Mechanics and its Applications 329 (1-2) (2003) 178–198.

[31] A. L. Alejandro-Quiñones, K. E. Bassler, M. Field, J. L. McCauley, M. Nicol, I. Timofeyev, A. Török, G. H. Gunaratne, A theory of fluctuations in stock prices, Physica A: Statistical Mechanics and its Applications 363 (2) (2006) 383–392.

[32] G. H. Gunaratne, M. Nicol, L. Seemann, A. Torok, Clustering of volatility in variable diffusion processes, Physica A: Statistical Mechanics and its Applications 388 (20) (2009) 4424–4430.

[33] A. C. Silva, V. M. Yakovenko, Stochastic volatility of financial markets as the fluctuating rate of trading: An empirical study, Physica A: Statistical Mechanics and its Applications 382 (1) (2007) 278–285.

[34] R. C. A. Oomen, Properties of realized variance under alternative sampling schemes, J. Bus. Econ. Statist. 24 (2) (2006) 219–237.

[35] J. E. Griffin, R. C. A. Oomen, Sampling returns for realized variance calculations: Tick time or transaction time?, Econometric Reviews 27 (1-3) (2008) 230–253.

[36] T. Preis, H. Stanley, Switching phenomena in a system with no switches, Journal of Statistical Physics 138 (1) (2010) 431–446.

[37] T. Preis, J. J. Schneider, H. E. Stanley, Switching processes in financial markets, Proceedings of the National Academy of Sciences 108 (19) (2011) 7674–7678.

[38] H. E. Stanley, S. V. Buldyrev, G. Franzese, S. Havlin, F. Mallamace, P. Kumar, V. Plerou, T. Preis, Correlated randomness and switching phenomena, Physica A: Statistical Mechanics and its Applications 389 (15) (2010) 2880–2893.

[39] P. C. Jain, G.-H. Joh, The dependence between hourly prices and trading volume, Journal of Financial and Quantitative Analysis 23 (3) (1988) 269–283.

[40] K. Chan, Y. P. Chung, H. Johnson, The intraday behavior of bid-ask spreads for nyse stocks and cboe options, Journal of Financial and Quantitative Analysis 30 (3) (1995) 329–346.

[41] A. C. Silva, Applications of physics to finance and economics: Returns, trading activity and income, Ph.D. thesis, University of Maryland, College Park (2005).

Chapter 3

Variable Diffusion Model for Stock Markets

3.1 Stock Markets Data

We obtained our minute data for the 328 most actively traded symbols, including stocks in the US market from PiTrading.com (`http://pitrading.com/intraday_ascii_data_market_edition.htm`). Availability of most stocks data can be traced back to 1991∼1992; however, due to technical limitations at that time, the quality of data is not comparable to that of data after 2002. So we restrict ourselves on the most reliable data, i.e., the most recent 2500 trading days, which approximately correspond to the recent decade. The data provide open, close, high, and low prices within every minute, together with trading volume. One problem is that not every minute's price is recorded, perhaps due to technical problems or errors (most likely before 2000) or the fact that price did not change during the interval (most likely after 2000). When this happened, we substituted the missing data by the last recorded data, and set the trading volume to 0, because the probability that a stock is traded but the price does not change is less than the probability that the stock is not traded, given the condition that the price does not change within one minute. In our analysis, we focused on five representative stocks, whose trading symbols are INTC, MSFT, IBM, XOM, and CVX, corresponding to Intel Corp., Microsoft Corp., International Business Machines Corp., Exxon Mobil Corp., and Chevron Corp., respectively. These five stocks are among the most actively traded stocks among our data.

3.2 Results

3.2.1 Intraday Seasonality

Before performing the statistics, we detrended the centered increments process of log return $X_{t;0}$ by subtracting ensemble averaged mean $\mathbb{E}[X_{t;0}]$, where $X_{0;0} = 0$ by construction and $\mathbb{E}[X_{t;0}]$ depends explicitly on time. After this detrending, the increments $X_{t+\tau;t}$ are detrended automatically, so we can compute their variance by ensemble average. We also compared them to sum of trading volume from t to $t+\tau$, and the result is shown in Figure 3.1. We found that other stocks exhibit similar intraday seasonality shown in Figure 3.2. The intraday variance pattern is evidence for non-stationary increments of the underlying stochastic process, which is in contradiction with the assumption of stationary increments needed for time averaging techniques. Several approaches have been suggested to overcome this problem. One set of approaches redefines "time"in the stochastic process. Instead of using physical time, other time measures have been proposed that are based on characteristic financial events [1, 2, 3, 4, 5]. Oomen [2] reports advantages in using transaction time, which increases by one unit for each reported transaction. Tick time increases time by one unit for each price change [3, 4, 5]. Another approach suggested by Dacorogna et al. introduces ϑ-time which accounts for the seasonal intraday and intra-week aspect of volatility [6, 7].

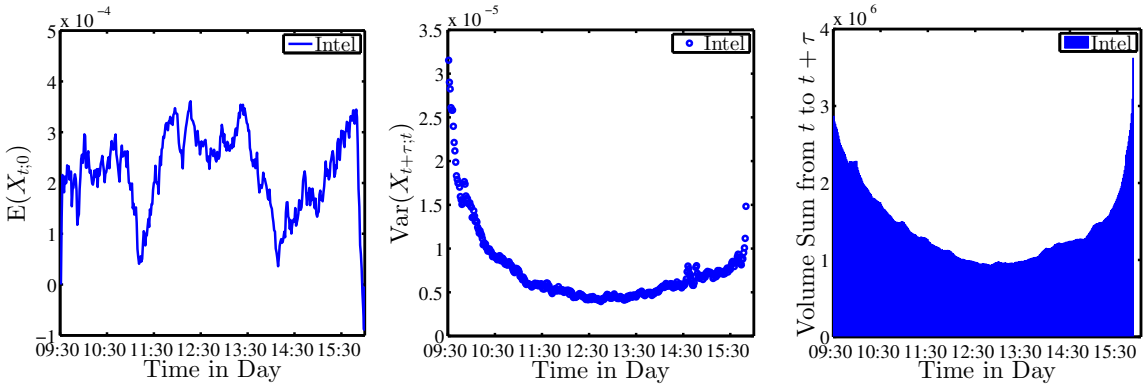

Figure 3.1: Intraday seasonality of INTC. (left) Ensemble averaged mean of centered increments of log returns. (middle) Ensemble averaged variance of increments from t to $t+\tau$ where $\tau = 10$ minutes. This U-shaped pattern has been reported previously [8, 9, 10]. (right) Sum of trading volume from t to $t+\tau$. The pattern is similar to the variance of increments.

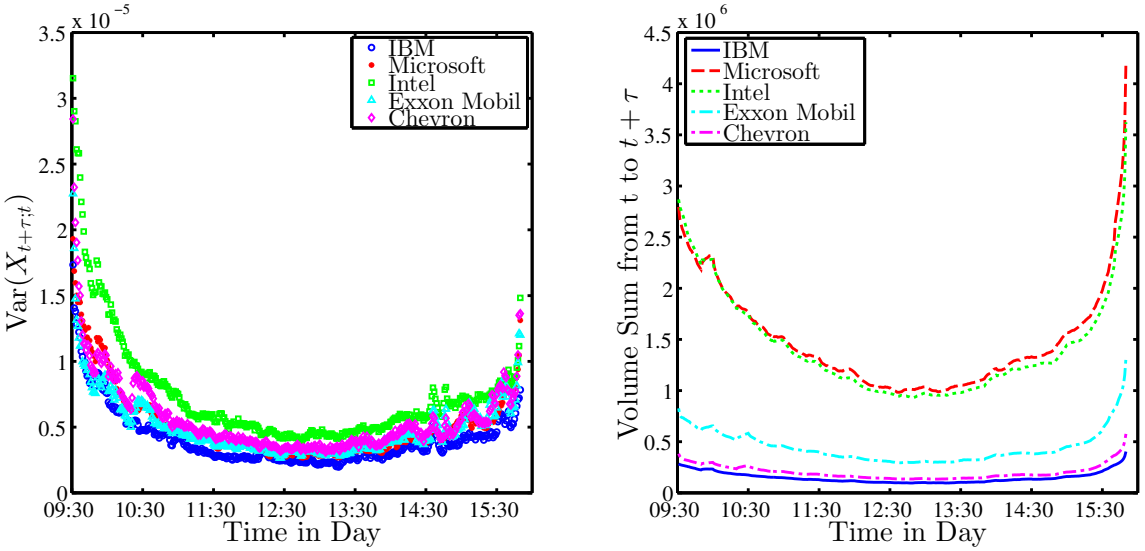

Figure 3.2: Variance and volume sum of all 5 stocks. Notice that there are two anomalous peaks appeared around 2:30PM in the variance of increments and absented in volume sum.

Because of the similarity between the patterns of variance and trading volume, we may expect they are strongly correlated and the quotient will approximate a horizontal line. The empirical result is shown in Figure 3.3. This may suggest that using event-based transaction time results in time series with approximately stationary increments during active markets. The intraday behavior of the average number of ticks (hence the trading volume) is similar to that of volatility (hence the variance); moreover, they peak at the same time, leading to an intuitive conclusion that the price fluctuations increase with a higher trading frequency. Additional evidence for this assertion was made previously [11, 12, 13], where it was found that in an event-based ε time scale defined by local extreme values in price, the volatility

of price, trading volume, and frequency of trading (equivalently, the number of ticks per unit time) peak at the same time, which is the end of an interval during which the price exhibits an increasing or decreasing trend, corresponding to local extreme values in the price.

However, when applying sliding interval techniques to event-based or rescaled time, the assumption of stationary increments needs to be verified for the rescaled time series as well. It is not clear that the rescaled times series results in processes with stationary increments. For example, Figure 3.3 may indicate that event-based transaction time results in time series with non-stationary increments at the beginning of day and also around 2:30PM. Our ensemble averages provides an alternative by averaging over trading days; here, the assumption of non-stationary increments is not needed.

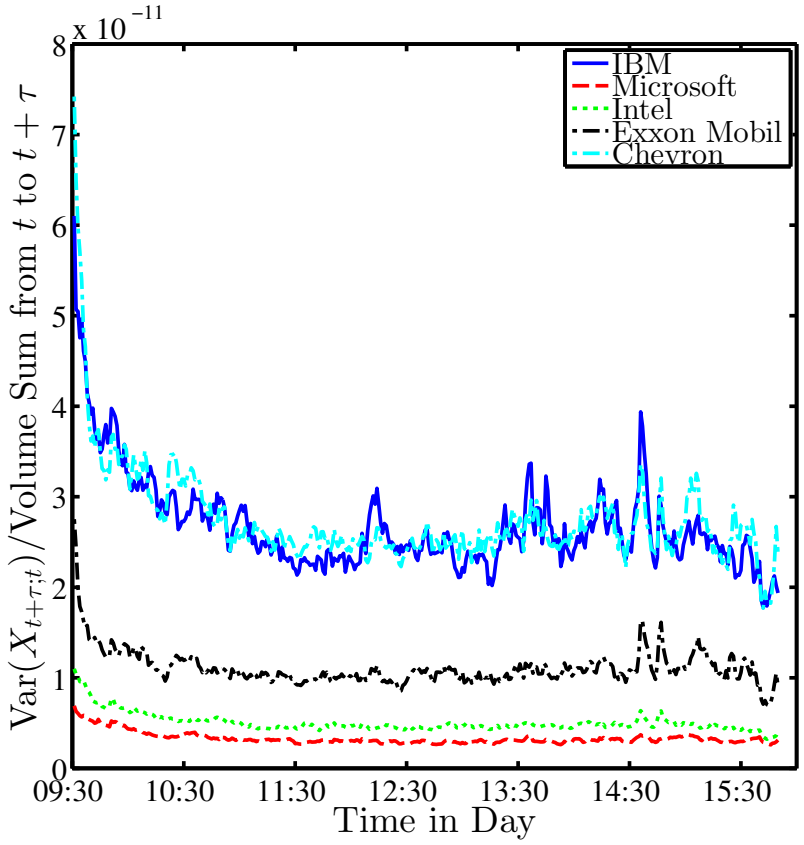

Figure 3.3: Dividing the variance of increments from t to $t+\tau$ by the sum of trading volume during the same time interval. Notice that although the curve is flat in most time in day, there are two anomalous peaks appearing around 2:30PM for all 5 stocks.

3.2.2 Scaling

The variance $\mathrm{Var}(X_{t+\tau;t})$ scales as power law during two intervals within the day. Power law fits to the data are shown in Figure 3.4, where the horizontal bars indicate the starts and ends of intervals. Notice that we only fit the data when $t \gg \tau$, since according to (1.7), $\mathrm{Var}(X_{t+\tau;t}) = \frac{\langle D(u)\rangle}{2H}[(t+\tau)^{2H} - t^{2H}] \xrightarrow{t\gg\tau} \langle D(u)\rangle \tau t^{2H-1}$, where t

is measured from the beginning of interval. Similar scaling behaviors and power law fits for other stocks are shown in Figure 3.5.

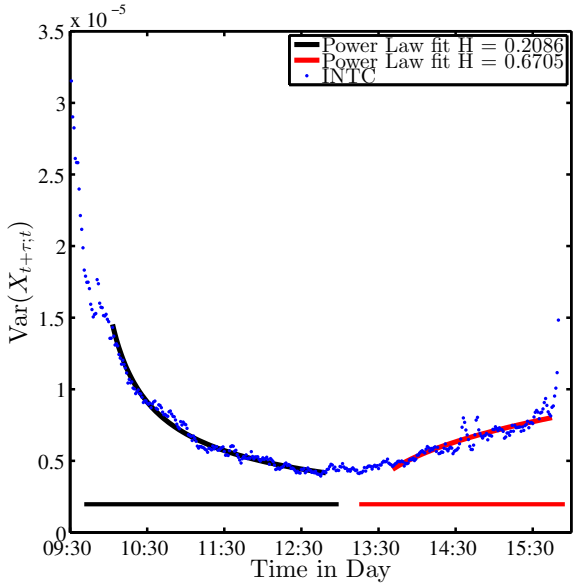

Figure 3.4: Intraday variance and scaling intervals with power law fit for INTC. Two scaling intervals where intraday variance of increments $X_{t+\tau;t}$ v.s. t can be fitted by power law $\mathrm{Var}(X_{t+\tau;t}) \sim t^{2H-1}$

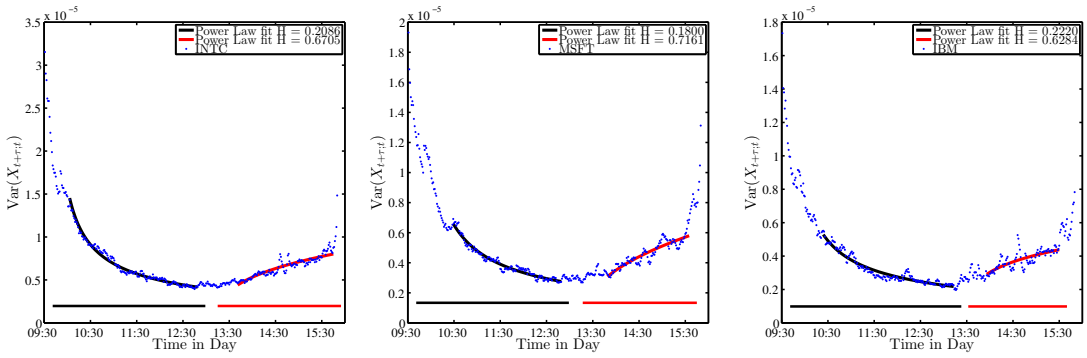

(a) INTC (b) MSFT (c) IBM

Figure 3.5: Intraday increments are nonstationary in three stocks and exhibit similar scaling behavior. The scaling regions are indicated by horizontal bars. We found similar intraday seasonality in other most actively traded stocks.

The scaling in variance of increments is merely a necessary but not sufficient condition of scaling. To confirm the validity of scaling, one needs to check whether there is data collapse of the form (1.4). Unfortunately, the available data are insufficient to observe this data collapse. Instead, an alternative verification of scaling is to check whether the moments $\left\langle X_{t;0}^{\beta} \right\rangle^{\frac{1}{\beta}}$ scales as t^H for all β (in practical, a finite number of β) [14], or to avoid the sensitivity in the beginning of scaling time interval, check whether the moments of increments $\left\langle X_{t+\tau;t}^{\beta} \right\rangle^{\frac{1}{\beta}}$ scales as $t^{H-\frac{1}{2}}$ [15], as shown in Figure 3.6. Notice that the fluctuations in moments of increments are larger in the second scaling interval, hence the fluctuations in exponent η of t^{η} for different β are larger.

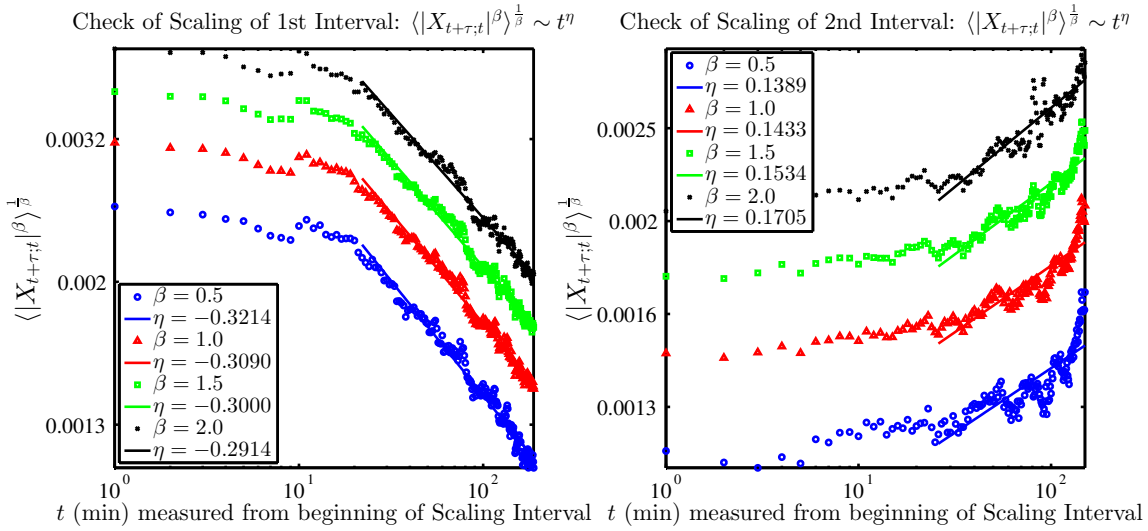

Figure 3.6: Moments of increments scale in time for INTC. Log-log plots of $\left\langle X^{\beta}_{t+\tau;t} \right\rangle^{\frac{1}{\beta}} \sim t^{H-\frac{1}{2}}$ v.s. t, where t is measured from the beginning of scaling interval. Notice that since the fluctuation in variance v.s. time for the second scaling interval is larger, the difference in exponents for different β's is larger than the first scaling interval.

The nearly uniform scaling of moments of increments shown in Figure 3.6 does confirm scaling, which means that the return distribution itself scales in time $W(x,t;0) = t^{-H}F(u)$. As mentioned above, the available data are insufficient to determine $F(u)$ accurately using the usual method of collapsing $W(x,t;0)$ for each value of t. However, since we have determined H independently from power law fit shown in Figure 3.5, we can use (1.4) for multiple values of t inside the interval to determine $F(u)$. The result is shown in Figure 3.7, where we used variable bin size to regulate the behavior in tail, and separated different t by $\tau = 10$ minutes to avoid unnecessary

correlation [16, 15]. Notice that $F(u)$ is asymptotically bi-exponential in two intervals, which suggests a linear variable diffusion process with $D(u) = D_0(1+\varepsilon|u|)$ and $F(u) = \frac{\varepsilon\alpha^\alpha e^\alpha}{2\Gamma(\alpha,\alpha)}(1+\varepsilon|u|)^{\alpha-1}e^{-\varepsilon\alpha|u|}$, where $\alpha = \frac{2H}{D_0\varepsilon^2}$, and $\Gamma(s,x) = \int_x^\infty t^{s-1}e^t dt$, as discussed in section 1.4. This finally fixes the form of our linear variable diffusion model.

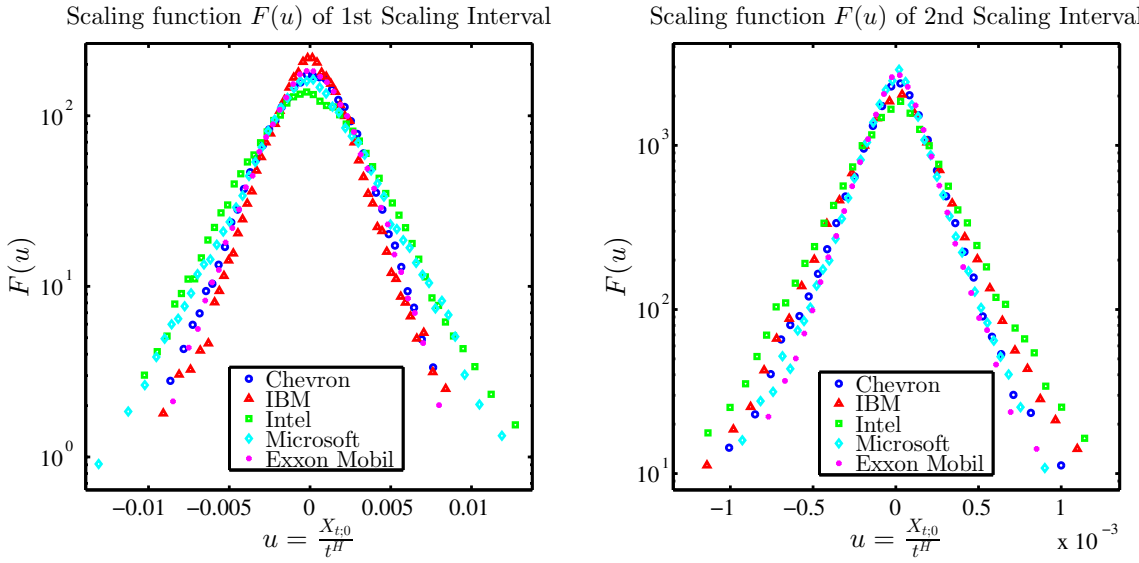

Figure 3.7: Scaling function $F(u)$ of five stocks in first and second scaling interval. The computation was performed by mixing increments $X_{t;0}$ of different $t = n\tau$, where $n = 0, 1, 2\ldots$ until the end of each scaling interval [16, 15]. The scaling function $F(u)$ was estimated through histograms with variable bin size, which specifies a minimum bin width and a minimum number of observations within each bin. It can be seen that $F(u)$'s are asymptotically bi-exponential in both scaling intervals.

3.2.3 Autocorrelation

We also calculated the autocorrelation function by using the ensemble average, as defined in 1.5. The result is shown in Figure 3.8. Autocorrelation of linear increments decays rapidly when $t_2 - t_1 > \tau$ (non-overlapping increments) as expected, which eliminates stochastic processes with memory as a description for the underlying dynamics, such as fractional Brownian motion [17]. Autocorrelation of absolute and squared increments decays slowly, which indicates "volatility clustering", and rules out statistically independent processes including Lévy processes [18]. Unfortunately, the available data are insufficient to determine the asymptotic behavior of this slow decay, as discussed in Ref. [19, 20].

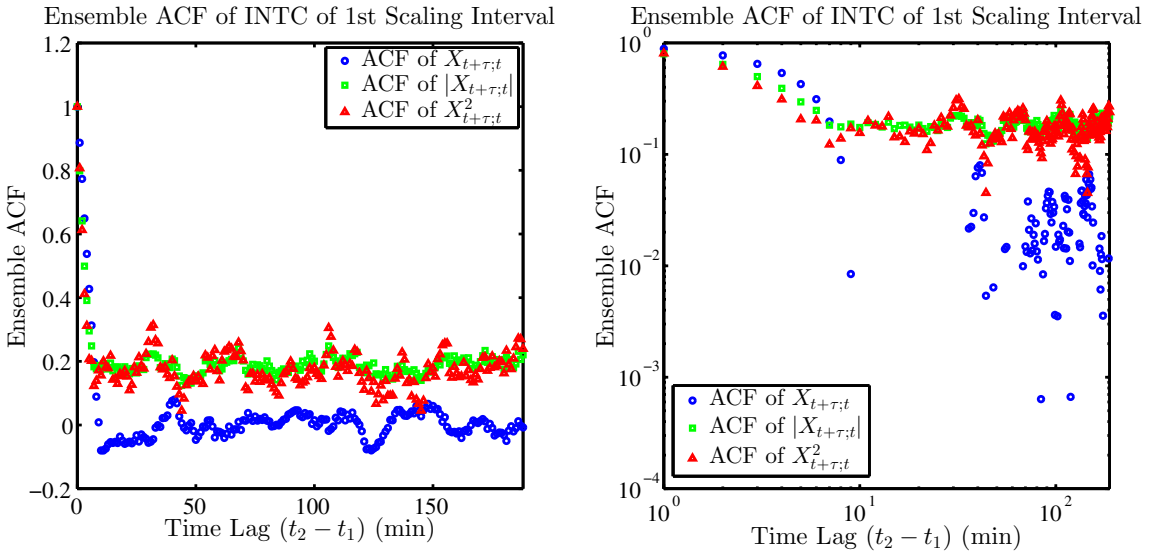

Figure 3.8: Ensemble autocorrelation function (ACF) of INTC in the first scaling interval, in both linear plot and log-log plot. The autocorrelation of linear increments drops down to zero for non-overlapping increments as expected. The autocorrelation of absolute and squared increments decay slowly, which indicates the volatility clustering. However, due to the limited amount of empirical data, there are too many fluctuations to identify the asymptotic behavior of this decay.

3.2.4 Parameter Estimation

There are three parameters in our linear variable diffusion model, H, D_0, and ε. H has been determined independently from a power law fit of $\mathrm{Var}(X_{t+\tau;t}) \sim t^{2H-1}$. D_0 and ε can be estimated by the fit of $F(u) = \frac{\varepsilon\alpha^\alpha \mathrm{e}^\alpha}{2\Gamma(\alpha,\alpha)}(1+\varepsilon|u|)^{\alpha-1}\mathrm{e}^{-\varepsilon\alpha|u|}$. One can perform this fit by naive curve fit of $F(u)$ and setting the normalization constant $\frac{\varepsilon\alpha^\alpha \mathrm{e}^\alpha}{2\Gamma(\alpha,\alpha)}$ as a free parameter, and renormalizes $F(u)$ after the estimations of D_0 and ε.

However, this fit depends on the variable bins used in estimation of $F(u)$. So a more sophisticated distribution fit is employed by maximum likelihood estimation (MLE) with the analytical form of $F(u)$ as a priori. The results are shown in Figure 3.9.

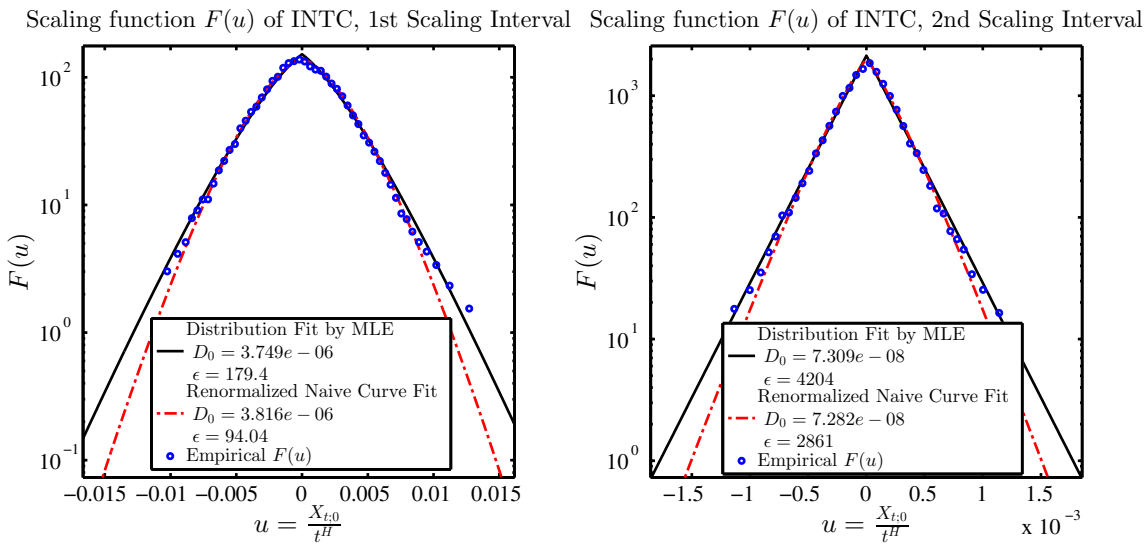

Figure 3.9: Estimation of D_0 and ε by curve fit and distribution fit. Notice that the major difference between curve fit and distribution fit by MLE lies in the tail.

3.2.5 Simulation and Comparison

After estimating all three parameters in our model, we simulated a set (10^6 trading days) of independent time series by combining two different scaling intervals with corresponding parameters. Unlike the foreign exchange markets where trading happens 24/7, stock markets open and close everyday, so every trading day can be naturally considered as an independent member of ensemble. We also found that an increase of number of days simulated ($> 10^6$) will not yield different results. The comparison

of empirical and simulated intraday variance patterns is shown in Figure 3.10.

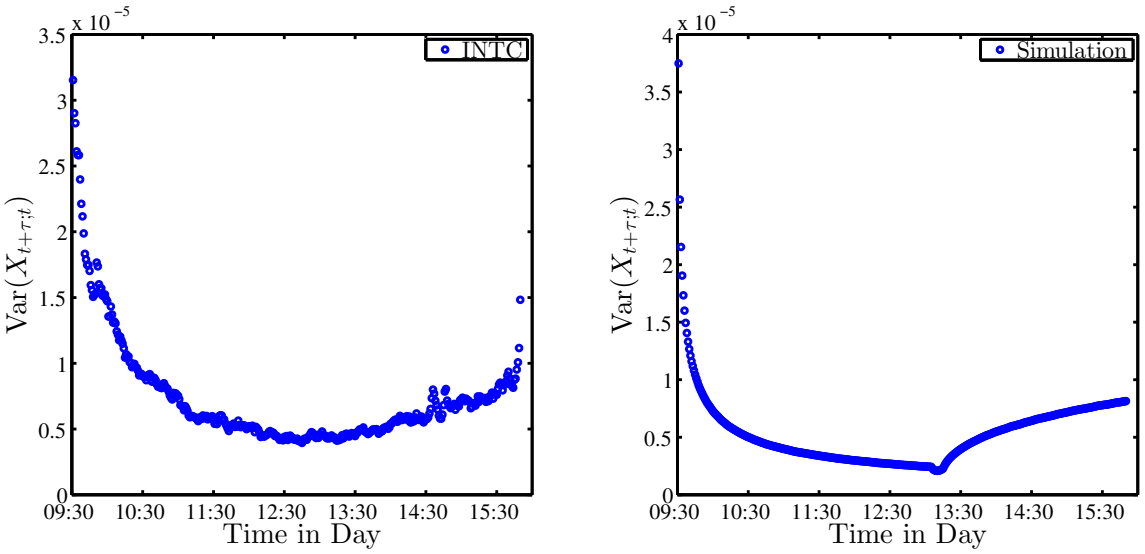

Figure 3.10: Empirical and simulated intraday variance of increments. Note that in simulation, every trading day consists of two scaling interval with different parameters.

We also compared the scaling function $F(u)$ for empirical and simulated time series in two scaling intervals, as shown in Figure 3.11. The results indicate consistency between the model and empirical data within each scaling interval.The scaling function for each scaling interval agrees with the analytical form $F(u) = \frac{\varepsilon\alpha^{\alpha}\mathrm{e}^{\alpha}}{2\Gamma(\alpha,\alpha)}(1+\varepsilon|u|)^{\alpha-1}\mathrm{e}^{-\varepsilon\alpha|u|}$.

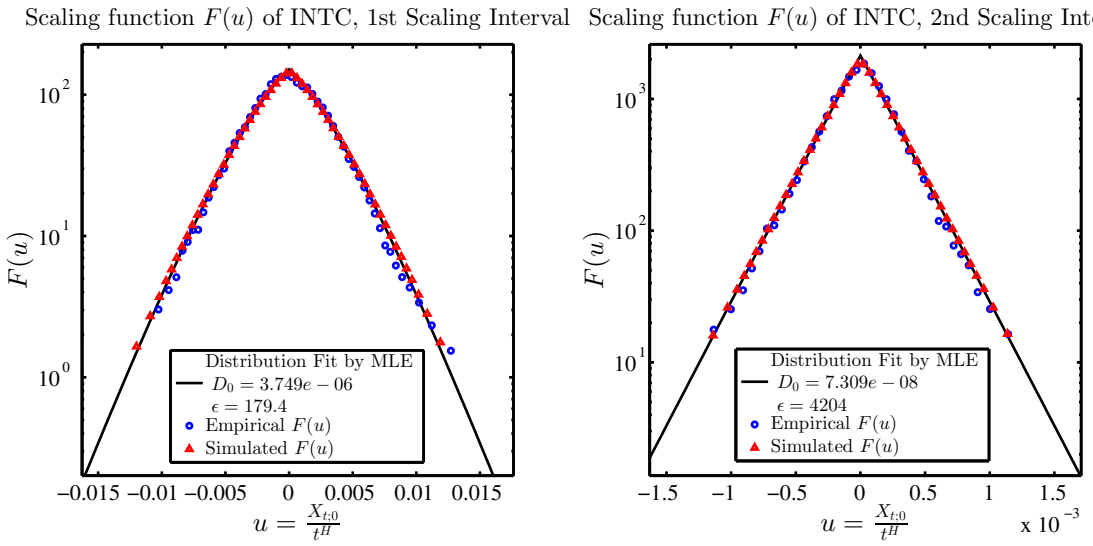

Figure 3.11: Comparison of empirical and simulated scaling function $F(u)$ in the first and second scaling interval.

Statistical analyses of financial markets have often been conducted by using sliding interval methods, which implicitly assume that the underlying stochastic process has stationary increments. For example, they compute the distribution

$$W_S(x,t) = \langle W(x, t_0 + t; t_0) \rangle_{t_0}, \tag{3.1}$$

where $\langle \cdot \rangle_{t_0}$ denotes time average over t_0. Many of these studies have reported that $W_S(x,t)$ scales as

$$W_S(x,t) = \frac{1}{t^{H_S}} F_S(v), \tag{3.2}$$

where $v = \frac{X_{t_0+t;t_0}}{t^{H_S}}$ and $H_S \approx \frac{1}{2}$. This $H_S \approx \frac{1}{2}$ is merely a spurious result of inappropriate using of sliding interval method. Because if we average the variance of increments $\mathrm{Var}(X_{t+\tau,t}) \xrightarrow{t \gg \tau} \langle D(u) \rangle \tau t^{2H-1}$ over t by a sliding window, we will get

$$\langle \mathrm{Var}(X_{t+\tau,t}) \rangle_t \sim \langle D(u) \rangle \tau \langle t^{2H-1} \rangle_t, \tag{3.3}$$

hence $\langle \mathrm{Var}(X_{t+\tau,t})\rangle_t$ grows linearly as τ^{2H_S}, where $H_S = \frac{1}{2}$ regardless of the value of H. This motivated us to assess our simulated time series using both ensemble average and sliding interval with $H_S = 0.5$ and different interval lengths. The results are shown in Figure 3.12. It can be seen that ensemble average can deduce the underlying dynamics correctly, since for simulation where we have enough amount of data, we observed data collapse in $W(x,t;0) = t^{-H}F(u)$. However, time average cannot yield correct deduction of the underlying dynamics because our results showed that distributions $W_S(x,t)$ do not scale, and hence that F_S is not well defined.

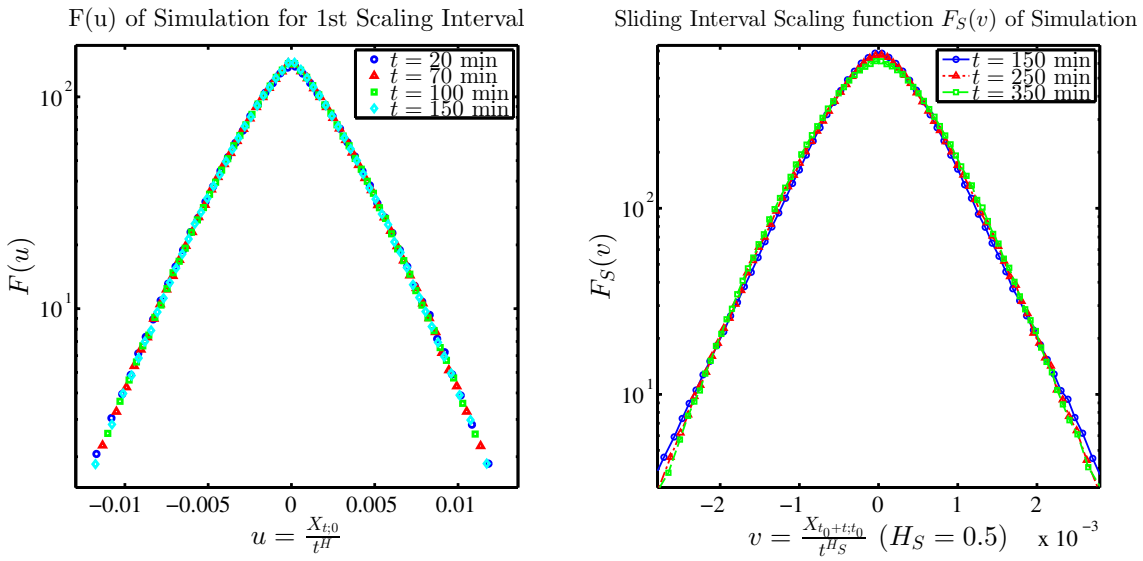

Figure 3.12: Comparison of ensemble and time averaged $F(u)$ of simulated time series in the first scaling interval. (left) The collapse of scaling function $F(u)$ is observed, where $F(u)$ is calculated by ensemble average. (right) Sliding interval scaling function $F(u)$ does not scale. For different t, when averaging over starting time $t_0 = nt$ where $n = 0, 1, 2 \ldots$ until $t_0 + t$ reaches the end of scaling interval, the corresponding $F(u)$ lies on different curve. This indicates that the sliding interval method is not appropriate for non-stationary increments.

3.3 Discussion and Conclusion

Now with variable diffusion SDE (1.6) in the log return variable $X_t = \ln \frac{P_t}{P_0}$, we can transform back to an SDE in price variable $P_t = P_0 \mathrm{e}^{X_t}$ by using Itō's lemma [21]

$$dP_t = P_t dX_t + \frac{1}{2} P_t (dX_t)^2 = \frac{1}{2} P_t D(X_t, t) dt + P_t \sqrt{D(X_t, t)} dB_t. \tag{3.4}$$

The dynamics of $P_t = \frac{P^A + P^B}{2}$ is driven by buy and sell orders, where P^A and P^B are ask and bid price, respectively. Recent studies [22, 23] have attempted to model order book dynamics by Poisson processes, and they show that this discrete time process will converge to a diffusion process under continuous limit. Our variable diffusion model provides a macroscopic time scale limit (i.e., a continuous time limit) for such models, as we argue.

Consider a simplest, proof-of-concept agent-based order book model introduced in [23]:

- The order book starts in a full state: all limits above $P^A(0)$ and below $P^B(0)$ are filled with one limit order of unit size q. The spread $S \equiv P^A - P^B$ initiates at 1 tick;
- The flow of market orders is modeled by two Poisson processes M_t^+ (buy orders) and M_t^- (sell orders) with arrival rates (or intensities) λ^+ and λ^-;
- There is one liquidity provider, who reacts immediately after a market order arrives so as to maintain the spread always equal to 1 tick. The provider places a limit order on the same side as the market order (i.e., a buy limit order after a buy market order and vice versa) with probability u and on the opposite side with probability $1 - u$.

Then the price dynamics can be expressed as

$$dP_t = \Delta P(dM_t^+ - dM_t^-) \cdot Z, \tag{3.5}$$

where ΔP is the discrete price resolution, or the tick, and Z is a Bernoulli random variable with

$$Z = \begin{cases} 0 & \text{with probability } 1-u \\ 1 & \text{with probability } u \end{cases}, \tag{3.6}$$

and M_t^+ and M_t^- are Poisson processes, which represent total number of buy and sell market orders counted from 0 to t, respectively. Hence dM_t^+ and dM_t^- are number of events in time interval $(t, t+dt]$ which follow Poisson distribution with parameters $\lambda^+ dt$ and $\lambda^- dt$

$$\begin{cases} \Pr(dM_t^+ = k) = \dfrac{\mathrm{e}^{-\lambda^+ dt}(\lambda^+ dt)^k}{k!} \\ \Pr(dM_t^- = k) = \dfrac{\mathrm{e}^{-\lambda^- dt}(\lambda^- dt)^k}{k!} \end{cases}. \tag{3.7}$$

Since dt is infinitesimal, in analogy to Brownian motion dB_t, we keep only the first order in dt, so that

$$\Pr(dM_t = k) = \begin{cases} \mathrm{e}^{-\lambda dt} = 1 - \lambda dt, & k = 0 \\ \mathrm{e}^{-\lambda dt}\lambda dt = \lambda dt, & k = 1 \\ 0, & k \geq 2 \end{cases}. \tag{3.8}$$

With these equations, one can calculate mean and variance of dP_t

$$\begin{cases} \mathbb{E}[dP_t] = \Delta P u(\lambda^+ - \lambda^-)dt \\ \mathrm{Var}(dP_t) = \Delta P^2 u(\lambda^+ + \lambda^-)dt \end{cases}, \tag{3.9}$$

and conditional average of $df(P_t)$, where $f(P_t)$ is a test function introduced in Ref. [23].

Following the derivation in Ref. [23], one can show that if

$$\begin{cases} u(\lambda^+ - \lambda^-)\Delta P \to \mu & \text{when } \Delta P \to 0 \\ u(\lambda^+ + \lambda^-)\Delta P^2 \to \sigma^2 & \text{when } \Delta P \to 0 \end{cases}, \tag{3.10}$$

then

$$\mathbb{E}\left[df(P_t)|P_t = p\right] \to \left(\mu\frac{\partial f}{\partial p} + \frac{1}{2}\sigma^2\frac{\partial^2 f}{\partial p^2}\right)dt, \tag{3.11}$$

which is a classical diffusion operator corresponding to a Brownian motion with drift, because for a classical Itō process $dX_t = \mu dt + \sigma dB_t$, one must have

$$\mathbb{E}\left[df(X_t)|X_t = x\right] = \mathbb{E}\left[\frac{\partial f}{\partial x}dX_t + \frac{1}{2}\frac{\partial^2 f}{\partial x^2}(dX_t)^2\right] = \left(\mu\frac{\partial f}{\partial x} + \frac{1}{2}\sigma^2\frac{\partial^2 f}{\partial x^2}\right)dt. \tag{3.12}$$

By using functional central limit theorem, one can generally show that dP_t converges in distribution to $u(\lambda^+ - \lambda^-)\Delta P dt + \sqrt{u(\lambda^+ + \lambda^-)}\Delta P dB_t$ in continuous limit.

In order for this microscopic time scale model converging to a lowest order approximation of real market dynamics in macroscopic time scale, as described by our variable diffusion model in price variable (3.4), one must have

$$\begin{cases} u(\lambda^+ - \lambda^-)\Delta P \to \dfrac{1}{2}P_t D(X_t, t) \\ u(\lambda^+ + \lambda^-)\Delta P^2 \to P_t^2 D(X_t, t) \end{cases}, \tag{3.13}$$

or in other words

$$\begin{cases} u\lambda^+ \to \dfrac{1}{2}D(X_t, t)\left[\left(\dfrac{P_t}{\Delta P}\right)^2 + \dfrac{1}{2}\dfrac{P_t}{\Delta P}\right] \\ u\lambda^- \to \dfrac{1}{2}D(X_t, t)\left[\left(\dfrac{P_t}{\Delta P}\right)^2 - \dfrac{1}{2}\dfrac{P_t}{\Delta P}\right] \end{cases}. \tag{3.14}$$

So our model provides a macroscopic limit for microscopic model, which is in analogy with thermodynamic limit of statistical mechanics.

In summary, by comparison of statistical results of empirical and simulated time series, we can conclude that our variable diffusion model is a good zeroth order approximation of the real dynamics of stock markets, because the simulated time

series in terms of our model can replicate the major statistical characteristics of empirical time series. Meanwhile, we justify again the importance of using ensemble average method since we observed strong intraday seasonality which contradict the assumption of stationary increments. Our variable diffusion model also provides new insight into stochastic models in microscopic time scale for financial market dynamics.

Finally, we may inquire whether and how we can distinguish between a drift-free Markovian from a Martingale. A possible direction is to extend the definition of Joseph exponents to be able to calculate them for non-stationary processes by using ensemble average. A successful extension of this definition may help us to detect higher order correlations in stochastic processes, and it will finally clarify the relationship between Joseph or Hurst exponents and efficient market hypothesis (EMH). We are currently working towards addressing this issue.

Bibliography

[1] A. C. Silva, V. M. Yakovenko, Stochastic volatility of financial markets as the fluctuating rate of trading: An empirical study, Physica A: Statistical Mechanics and its Applications 382 (1) (2007) 278–285.

[2] R. C. A. Oomen, Properties of realized variance under alternative sampling schemes, J. Bus. Econ. Statist. 24 (2) (2006) 219–237.

[3] J. E. Griffin, R. C. A. Oomen, Sampling returns for realized variance calculations: Tick time or transaction time?, Econometric Reviews 27 (1-3) (2008) 230–253.

[4] A. Chakraborti, I. M. Toke, M. Patriarca, F. Abergel, Econophysics review: I. empirical facts, Quantitative Finance 11 (7) (2011) 991–1012.

[5] A. Chakraborti, I. M. Toke, M. Patriarca, F. Abergel, Econophysics review: II. agent-based models, Quantitative Finance 11 (7) (2011) 1013–1041.

[6] M. M. Dacorogna, U. A. Müller, R. J. Nagler, R. B. Olsen, P. O. V., A geographical model for the daily and weekly seasonal volatility in the foreign-exchange market, Journal of International Money and Finance 12 (4) (1993) 413–438.

[7] M. M. Dacorogna et al., An Introduction to High-Frequency Finance, Academic Press, San Diego, CA, 2001.

[8] P. C. Jain, G.-H. Joh, The dependence between hourly prices and trading volume, Journal of Financial and Quantitative Analysis 23 (3) (1988) 269–283.

[9] K. Chan, Y. P. Chung, H. Johnson, The intraday behavior of bid-ask spreads for nyse stocks and cboe options, Journal of Financial and Quantitative Analysis 30 (3) (1995) 329–346.

[10] A. C. Silva, Applications of physics to finance and economics: Returns, trading activity and income, Ph.D. thesis, University of Maryland, College Park (2005).

[11] T. Preis, H. Stanley, Switching phenomena in a system with no switches, Journal of Statistical Physics 138 (1) (2010) 431–446.

[12] T. Preis, J. J. Schneider, H. E. Stanley, Switching processes in financial markets, Proceedings of the National Academy of Sciences 108 (19) (2011) 7674–7678.

[13] H. E. Stanley, S. V. Buldyrev, G. Franzese, S. Havlin, F. Mallamace, P. Kumar, V. Plerou, T. Preis, Correlated randomness and switching phenomena, Physica A: Statistical Mechanics and its Applications 389 (15) (2010) 2880–2893.

[14] J. L. McCauley, G. H. Gunaratne, K. E. Bassler, Hurst exponents, Markov processes, and fractional Brownian motion, Physica A: Statistical Mechanics and its Applications 379 (1) (2007) 1–9.

[15] K. E. Bassler, J. L. McCauley, G. H. Gunaratne, Nonstationary increments, scaling distributions, and variable diffusion processes in financial markets, Proceedings of the National Academy of Sciences 104 (44) (2007) 17287–17290.

[16] L. Seemann, J. L. McCauley, G. H. Gunaratne, Intraday volatility and scaling in high frequency foreign exchange markets, International Review of Financial Analysis 20 (3) (2011) 121–126.

[17] B. Mandelbrot, J. W. van Ness, Fractional Brownian motions, fractional noises and applications, SIAM Review 10 (4) (1968) 422–437.

[18] G. H. Gunaratne, J. L. McCauley, M. Nicol, A. Török, Variable step random walks and self-similar distributions, Journal of Statistical Physics 121 (5-6) (2005) 887–899.

[19] L. Seemann, J.-C. Hua, J. L. McCauley, G. H. Gunaratne, Ensemble vs. time averages in financial time series analysis, Physica A: Statistical Mechanics and its Applications 391 (23) (2012) 6024–6032.

[20] G. H. Gunaratne, M. Nicol, L. Seemann, A. Török, Clustering of volatility in variable diffusion processes, Physica A: Statistical Mechanics and its Applications 388 (20) (2009) 4424–4430.

[21] J. L. McCauley, Stochastic Calculus and Differential Equations for Physics and Finance, Cambridge University Press, Cambridge, UK, 2013.

[22] F. Abergel, A. Jedidi, A mathematical approach to order book modelling, in: F. Abergel, B. Chakrabarti, A. Chakraborti, M. Mitra (Eds.), Econophysics of Order-driven Markets, Springer Milan, 2011, pp. 93–107.

[23] F. Abergel, A. Jedidi, A mathematical approach to order book modeling, International Journal of Theoretical and Applied Finance 16 (05) (2013) 1350025.

Part II

Empirical-based Studies on Reacting Flows

Chapter 4

Introduction

4.1 Motivation and Background

Reacting flows are governed by nonlinear PDEs, specifically, the Navier-Stokes equations and reaction-diffusion equations. The major problems in trying to characterize the properties of solutions to these equations include unknown parameters, complicated boundary conditions, and the chaotic nature of the fluid flows. These make the analytical solution to the model system impossible, and numerical simulation not very helpful. Because the flows are chaotic, any initial tiny inaccuracy will be blown-up exponentially. In addition, the energy cascading to systematically smaller and smaller scales will require extremely fine grid to simulate the system.

However, high quality empirical data, such as measurements of temperature fields through *planner laser-induced florescence* (PLIF) and of velocity fields through *particle image velocimetry* (PIV) are becoming routinely available. The data can be used to perform modal decompositions and dimensional reductions of the flows to empirically characterize at least major qualitative properties of the flows.

4.2 Formulation

The typical task of modal decomposition is to empirically find a set of basis functions such that the observed evolution of a dynamical system can be expressed as a sum of "modes " by projecting the original observed time evolution of a secondary field (a vector evolving in time on a grid) onto the empirical basis. One example is the Fourier series expansion, where we need an infinite number of basis functions. To be efficient

for application purposes, we require a small number of basis vectors to capture the primary information contained in the dynamics, and filter out experimental noise and non-reproducible features.

Consider a (nonlinear) dynamical system evolving on a manifold M

$$\dot{\mathbf{z}} = \mathcal{F}(\mathbf{z}) \qquad (\text{or } \mathbf{z}_{t+\Delta t} = S(\mathbf{z}_t) \text{ for discrete time}), \tag{4.1}$$

where $\mathbf{z}_t \in M$ describes the state of dynamical system at time t. A time evolution operator S^t evolves, or maps the system initiated at state $\mathbf{z}_0$ to state $\mathbf{z}_t = S^t(\mathbf{z}_0)$, so it can be considered as a map from the state space manifold M to itself $S^t : M \to M$. The empirical data are observations or measurements of $\mathbf{z}_t$, which are secondary "fields" in that they are typically parameterized in space; for example, pixels in case of recorded video. Denote the secondary field by $[u(\mathbf{z}_t)](\mathbf{x})$, where $\mathbf{x}$ is the grid. Since $[u(\mathbf{z}_t)](\mathbf{x})$ is a field, u can be understood as a map from M to $\mathbb{R}^n$, where $[u(\mathbf{z}_t)](\mathbf{x})$ is a vector and n is the total number of grid points. For three-dimensional observations, e.g., velocity fields, u will map M to $\mathbb{R}^{3n}$. When $\mathbf{z}_0$ evolves to $\mathbf{z}_t = S^t(\mathbf{z}_0)$, the observed vector $[u(\mathbf{z}_0)](\mathbf{x})$ evolves to $[u(\mathbf{z}_t)](\mathbf{x}) = [u(S^t(\mathbf{z}_0))](\mathbf{x})$. By convention, we write $[u(\mathbf{z}_t)](\mathbf{x})$ (or for simplicity, ignore the $\mathbf{x}$ and write $u(\mathbf{z}_t)$) to emphasize it is an observation or map of state $\mathbf{z}_t$ to a vector $u(\mathbf{z}_t) \in \mathbb{R}^n$, whereas we write $u(\mathbf{x}, t)$ to emphasize it is an empirical data matrix where every row corresponds to a grid point, and every column corresponds to a snapshot.

The task of modal decomposition is to expand the empirical data matrix as a (finite) sum

$$u(\mathbf{x}, t) = \sum_k a_k(t)\varphi_k(\mathbf{x}) \tag{4.2}$$

by projecting every column in $u(\mathbf{x}, t)$ (which is an observed vector $u(\mathbf{z}_t)$ at time t) onto empirically determined basis $\{\varphi_k(\mathbf{x})\}$, and $\{a_k(t)\}$ are the corresponding projection coefficients.

4.3 Proper Orthogonal Decomposition

4.3.1 Formulation

In proper orthogonal decomposition, or principal-components analysis, the basis $\{\varphi_k(\mathbf{x})\}$ consists of normalized eigenvectors of the correlation matrix C given by $C_{\mathbf{x},\mathbf{x}'} \equiv \langle u(\mathbf{x}, t)u(\mathbf{x}', t)\rangle_t$, where $\mathbf{x}$ and $\mathbf{x}'$ are two grid points and the average $\langle\cdot\rangle_t$ is over time (from now on, $\langle\cdot\rangle$ will denote spatial averages over $\mathbf{x}$, and $\langle\cdot\rangle_t$ will represent a time average). Since C is real and symmetric, its eigenvectors $\{\varphi_k(\mathbf{x})\}$ are real and orthogonal. It can be always normalized, so we have the orthonormality condition

$$\langle\varphi_i(x)|\varphi_j(x)\rangle = \delta_{ij}. \tag{4.3}$$

These $\{\varphi_k(\mathbf{x})\}$ are called coherent structures or "topos". The $a_k(t)$ are time-dependent projection coefficients of $u(\mathbf{x}, t)$ on coherent structures $a_k(t) = \langle\varphi_k(x)|u(\mathbf{z}_t)\rangle$. $\varphi_0(\mathbf{x})$ is the time-averaged field. For observed fields in two spatial dimensions, denote the number of pixels in the two directions by H and W. Then the empirical spatio-temporal data matrix can be expanded as

$$u(\mathbf{x}, t) = \sum_{k=0}^{HW-1} a_k(t)\varphi_k(\mathbf{x}). \tag{4.4}$$

Fluctuations in $u(\mathbf{x}, t)$ can be quantified by "energy"

$$E_u = \sum_t \sum_x u(\mathbf{x}, t)^2 = \sum_k \sum_t a_k(t)^2, \tag{4.5}$$

where in the second equality, we used the expansion (4.4) and orthonormal condition (4.3). The "latency",

$$\lambda_k = \sum_t a_k(t)^2, \tag{4.6}$$

can be interpreted as the contribution of the k^{th} mode to the dynamics. The expansion is sorted in a non-increasing order of λ_k. By truncating the expansion (4.4) at an appropriate order n ($< HW$), one can obtain a reduced-order approximation [1] of the flow $u_n(\mathbf{x}, t) \equiv \sum_{k=0}^{n-1} a_k(t)\varphi_k(\mathbf{x})$. The "quality" of the approximation is given by

$$\beta_n = \frac{\sum_{k=0}^{n-1} \lambda_k}{E_u}. \tag{4.7}$$

Larger values of β_n correspond to better approximations of the empirical data matrix.

4.3.2 Properties of POD

The basis of POD are the most efficient ones in the sense that, for a given n, β_n is maximized. In other words, no other decomposition of the form $\sum_{k=0}^{n-1} \tilde{a}_k(t)\tilde{\varphi}_k(\mathbf{x})$ has a larger value of β_n [2, 3, 4, 5].

On the other hand, the problem of POD is that it can not be used to separate different flow constituents from a single or a set of coherent structures, because every single coherent structure can be a result of combination of different flow constituents. The order of coherent structure in expansion (4.4) is sorted solely by latency (4.6)

and nothing else. Therefore, the POD mode itself does not represent any dynamical information tied to a specific flow constituent. An example is the von Karman vortex shedding, which is asymmetric but not anti-symmetric. However, POD modes are either symmetric or anti-symmetric, and the anti-symmetric modes are combinations of von Karman vortices and symmetric vortices. So it is not possible to separate von Karman vortices from anti-symmetric modes, although the presence of anti-symmetric coherent structures can be considered as an indicator of onset of von Karman vortices.

The computation of POD modes are performed by calculation of eigenvalues and eigenvectors of correlation matrix $C_{\mathbf{x},\mathbf{x}'} \equiv \langle u(\mathbf{x},t)u(\mathbf{x}',t)\rangle_t$, which thus is a second-order statistics. It does not contain dynamical information and it is sensitive to experimental noise. POD can not distinguish non-reproducible patterns from noise either. If given a large enough truncation order n, we can effectively consider the rest of the flow $u(\mathbf{x},t) - u_n(\mathbf{x},t) = u(\mathbf{x},t) - \sum_{k=0}^{n-1} a_k(t)\varphi_k(\mathbf{x})$ as noise, but we cannot determine whether a specific $a_k(t)\varphi_k(\mathbf{x})$ where $k < n$ is non-reproducible or noise because, as shown in the next section, the latency λ_k does not provide this information.

Despite these disadvantages of POD, we successfully identify the onset of von Karman vortices as a flow constituent [6] by using symmetry broken coherent structures, combined with Lyapunov exponents and characteristics of unstable periodic orbits. However, we need to emphasize that this separation of flow constituents depends on the specific symmetry of experimental equipment, hence it is not possible

to perform this separation for flows in arbitrary domains. Furthermore, the qualitative characteristics of the dynamics indicated by Lyapunov exponents and unstable periodic orbits are sensitive to the noise in that POD is a second-order statistics. Dynamic mode decomposition avoids many of these problems.

4.4 Koopman Operator and Dynamic Mode Decomposition

4.4.1 Formulation of Koopman Operator

Consider again the time evolution operator $S^t : M \to M$ and empirical observation $u : M \to \mathbb{R}^n$. Now, define another operator

$$U^t \stackrel{\text{def.}}{=} S^{t*} : S^{t*}u = u \circ S^t, \tag{4.8}$$

which is the pullback of the time evolution operator S^t. Hence $U^t u(\mathbf{z}_0) = u \circ S^t(\mathbf{z}_0) = u(\mathbf{z}_t)$, which means that operator U^t maps the observation vector $u(\mathbf{z}_0)$ at time 0 to observation vector $u(\mathbf{z}_t)$ at time t. Since $u(\mathbf{z}_t) \in \mathbb{R}^n$, U^t is a linear map in $\mathbb{R}^n$. It can be shown that the spectrum of $\mathcal{F}$ in (4.2) is contained in that of U^t under very general conditions [7, 8], even when $\mathcal{F}$ and S^t are nonlinear; hence the stability and structure of solutions $\mathbf{z}_t$ of the system $\mathcal{F}$ can be inferred through the analysis of the operator U^t, which is called the Koopman operator.

Since U^t is a linear map in $\mathbb{R}^n$, it makes sense to consider its eigenvalues and

eigenvectors

$$U^t\phi(\mathbf{z}_0) = \phi(S^t(\mathbf{z}_0)) = \phi(\mathbf{z}_t) = \mathrm{e}^{\lambda t}\phi(\mathbf{z}_0), \tag{4.9}$$

where $\phi(\cdot)$ are special observables evolving with $\mathrm{e}^{\lambda t}$. Suppose the set of $\{\phi_k(\cdot)\}$ is complete or large enough such that all other observables $u(\cdot) \in \mathrm{span}\{\phi_k(\cdot)\}$, or in other words, $u(\mathbf{z}_0) = \sum_k \phi_k(\mathbf{z}_0)\alpha_k$, then $u(\mathbf{z}_t) = U^t u(\mathbf{z}_0) = \sum_k \mathrm{e}^{\lambda_k t}\phi_k(\mathbf{z}_0)\alpha_k$. The evolution of other observables are characterized by $\alpha_k \mathrm{e}^{\lambda_k t}$, where α_k are called Koopman modes.

4.4.2 Dynamic Mode Decomposition (DMD) and its Algorithm

Dynamic mode decomposition [9, 10, 11] is an efficient algorithm to compute approximations for the eigenvalues and eigenvectors of U^t from secondary fields $u(\mathbf{x}, t)$, namely, experimental snapshots, recorded with uniform time gap Δt. One can represent the linear map of the secondary field during the time interval $[t, t + \Delta t]$ as

$$u(\mathbf{x}, t + \Delta t) = \mathbf{A}u(\mathbf{x}, t), \forall t, \tag{4.10}$$

where $\mathbf{A}$ is an $n \times n$ matrix ($3n \times 3n$ in case of three dimensional vector observation). If $\mathbf{A}\Phi_k(\mathbf{x}) = \mathrm{e}^{\lambda_k \Delta t}\Phi_k(x)$, then $\mathbf{A}^m\Phi_k(\mathbf{x}) = \mathrm{e}^{\lambda_k m\Delta t}\Phi_k(x) \xrightarrow{\text{continuous limit}} U^t\phi_k(\mathbf{z}_0)$. The $\Phi_k(\mathbf{x})$ and λ_k are approximation of eigenvectors and eigenvalues of U^t.

Denoting by u_n the field corresponding to the snapshot taken at time $t = n\Delta t$, Eqn. (4.10) can be re-written as $u_{n+1} = \mathbf{A}u_n$. Thus,

$$\mathbb{V}_1^{n+1} \equiv [u_1, u_2, \ldots, u_{n+1}] = \mathbf{A}\,[u_0, u_1, u_2, \ldots, u_n] \equiv \mathbf{A}\mathbb{V}_0^n. \tag{4.11}$$

Note that for sufficiently large n (certainly for n larger than the number of pixels in each snapshot), u_{n+1} is linearly dependent on all the previous u_k's; write $u_{n+1} = \sum_{k=1}^{n} c_k u_k$. Thus, we can write $\mathbb{V}_1^{n+1} = \mathbb{V}_0^n \mathbf{B}$, where the *companion matrix* is [9, 10, 11, 7]

$$\mathbf{B} = \begin{pmatrix} 0 & 0 & \dots & 0 & c_0 \\ 1 & 0 & \dots & 0 & c_1 \\ 0 & 1 & \dots & 0 & c_2 \\ \dots & \dots & \dots & \dots & \dots \\ 0 & 0 & \dots & 1 & c_n \end{pmatrix}. \tag{4.12}$$

Since $\mathbf{A}\mathbb{V}_0^n = \mathbb{V}_0^n \mathbf{B}$, the spectrum of $\mathbf{B}$ is equal to that of $\mathbf{A}$. Even in cases where the expansion of u_{n+1} can only be approximated by a linear combination of u_k's, eigenvalues of $\mathbf{B}$ are approximations to those of $\mathbf{A}$ [9, 10, 7]. The spectrum of $\mathbf{B}$ can be computed using the (fast) Arnoldi method [12, 9]. Eigenfunctions of $\mathbf{A}$ are referred to as *dynamic modes* of the flow [9, 10, 11]. Dynamic mode decomposition provides a subset of the Koopman spectrum λ_k and the corresponding eigenfunctions $\phi_k(\mathbf{x})$.

The efficient algorithm introduced by [10] is to project $\mathbf{A}$ onto the POD modes, and then calculate the eigenvalues and eigenvectors of the projected operator. By setting up a threshold in singular value decomposition (SVD) when calculating the POD modes, one can automatically filter out some amount of noise. Since $\mathbf{A}\mathbb{V}_1^{N-1} = \mathbb{V}_2^N$, where $\mathbb{V}_1^{N-1}$ as defined in (4.11), now perform an SVD on $\mathbb{V}_1^{N-1} = U\Sigma W^T$, then $\mathbf{A}U\Sigma W^T = \mathbb{V}_2^N$, finally $U^T\mathbf{A}U = U^T\mathbb{V}_2^N W\Sigma^{-1} \equiv S$. The projected linear operator

S has eigenvalues and eigenvectors μ_i and y_i

$$Sy_i = \mu_i y_i, \tag{4.13}$$

such that $U^T \mathbf{A} U y_i = \mu_i y_i$, or $\mathbf{A} U y_i = \mu_i U y_i$, which means that $\Phi_i(\mathbf{x}) \equiv U y_i$ and μ_i are eigenvectors and eigenvalues of $\mathbf{A}$: $\mathbf{A}\Phi_i(\mathbf{x}) = \mu_i \Phi_i(\mathbf{x})$. Since $\mu_k = \mathrm{e}^{\lambda_k \Delta t}$, $\lambda_k = \frac{1}{\Delta t} \ln \mu_k$.

4.4.3 Properties of DMD

Because of nonlinear coupling between dynamic modes and driving of the system, the dynamics modes $\{\Phi_k(\mathbf{x})\}$ are merely an approximation of the Koopman eigenvectors $\{\phi_k(\mathbf{x})\}$, which means that $u(\mathbf{z}_t) = \sum_k \mathrm{e}^{\lambda_k t} \phi_k(\mathbf{z}_0) \alpha_k \approx \sum_k \mathrm{e}^{\lambda_k t} \Phi_k(\mathbf{z}_0) \alpha_k$. To get more accurate time evolution of dynamic modes $a_k(t)\Phi_k(\mathbf{x})$, we need to project the empirical data matrix onto $\{\Phi_k(\mathbf{x})\}$ directly, in analogy to the case of POD. However, the matrix $\mathbf{A}$ is not symmetric, so λ_k are complex and $\Phi_k(\mathbf{x})$ are not orthonormal in general. To extract $a_k(t)$, one has to project $u(\mathbf{x}, t)$ onto another basis $\{\Psi_k(\mathbf{x})\}$ orthonormal to $\{\Phi_k(\mathbf{x})\}$, where $\langle \Psi_i(\mathbf{x}) | \Phi_j(\mathbf{x}) \rangle = \delta_{ij}$ and $\Psi_k(\mathbf{x})$ are normalized eigenvectors of $\mathbf{A}^\dagger$, the Hermitian conjugate of $\mathbf{A}$

By constructing the basis $\{\Psi_k(\mathbf{x})\}$, one can extract $a_i(t)$ by projection $\langle \Psi_i(\mathbf{x}) | u(\mathbf{x}, t) \rangle = \sum_k a_k(t) \langle \Psi_i(\mathbf{x}) | \Phi_k(\mathbf{x}) \rangle = a_i(t)$, and decompose the $u(\mathbf{x}, t)$ in both $\{\Phi_k(\mathbf{x})\}$ and $\{\Psi_k(\mathbf{x})\}$

$$u(\mathbf{x}, t) = \sum_k a_k(t) \Phi_k(\mathbf{x}) = \sum_k b_k(t) \Psi_k(\mathbf{x}). \tag{4.14}$$

In analogy to POD, one can define total energy as $E_u = \sum_t \sum_x u(\mathbf{x}, t)^2$, and by using the decomposition (4.14), one can obtain $E_u = \sum_k \sum_t a_k(t) b_k^*(t)$. Notice that $a_k(t)$

and $b_k^*(t)$ are complex in general, so the latency associated to the k^{th} dynamics mode defined similarly as $\sum_t a_k(t)b_k^*(t)$ is not positive definite. Although $\sum_t a_k(t)b_k^*(t)$ can be complex, DMD modes appear in complex conjugation pairs. After a sum of its complex conjugated modes, only the real parts remain.

Unlike POD which uses second-order statistics, DMD modes are calculated using first order statistics, which are less sensitive to experimental noise. Unlike POD which only provides latency of every mode, DMD also provides an eigenvalue λ_k for every mode. Interestingly, these eigenvalues can be used to select modes associated with a specific flow constituent. Specifically, such eigenvalues are found to lie on a smooth curve in the complex plane [9, 10, 11]. An alternative scheme is as follows: recall that the primary dynamic mode (i.e., that with the highest latency) has a single frequency, which is $\mathrm{Im}(\lambda_k)$. One may expect dynamic modes with harmonics of this frequency to be associated with the same flow constituent.

The idea of eigenvalues lying on a smooth curve in complex plane can be illustrated by an example: flame or fluids flows are mostly drift and diffusion of patterns, which can be modeled by Fokker-Planck equation. Assume patterns mainly drift in x direction:

$$\frac{\partial \xi(\mathbf{x},t)}{\partial t} = -a\partial_x \xi + \frac{b}{2}(\partial_x^2 + \partial_y^2)\xi. \tag{4.15}$$

Now consider a trial solution $\xi_0 \mathrm{e}^{i\mathbf{k}\cdot\mathbf{x}+\lambda t} = \xi_0 \mathrm{e}^{ik_x x + ik_y y + \lambda t}$, such that the general solution $\xi = \sum_k \xi_{0k} \mathrm{e}^{i\mathbf{k}\cdot\mathbf{x}+\lambda_k t}$. Substituting this form of solution into (4.15), one can obtain $\lambda = -ak_x i - \frac{b}{2}(k_x^2 + k_y^2)$, and $\mathrm{Re}(\lambda) = -\frac{b}{2}(k_x^2 + k_y^2), \mathrm{Im}(\lambda) = -ak_x$. By eliminating the common k_x, one finally get $\mathrm{Re}(\lambda) = -\frac{b}{2a^2}[\mathrm{Im}(\lambda)]^2 - \frac{b}{2}k_y^2$. When k_x goes from $-\infty$ to $+\infty$, this equation becomes a curve in the complex plain of λ. Now, if

there are other patterns, or flow constituents governed by the same Fokker-Planck equation (4.15); however with different drift and diffusion coefficients, there will be different curves formed in the complex plain, and each curve will correspond to a specific flow constituent. Figure 4.1 shows one such, where the DMD eigenvalues are computed for a simulated solution of Fokker-Planck equation drifting to the negative x direction.

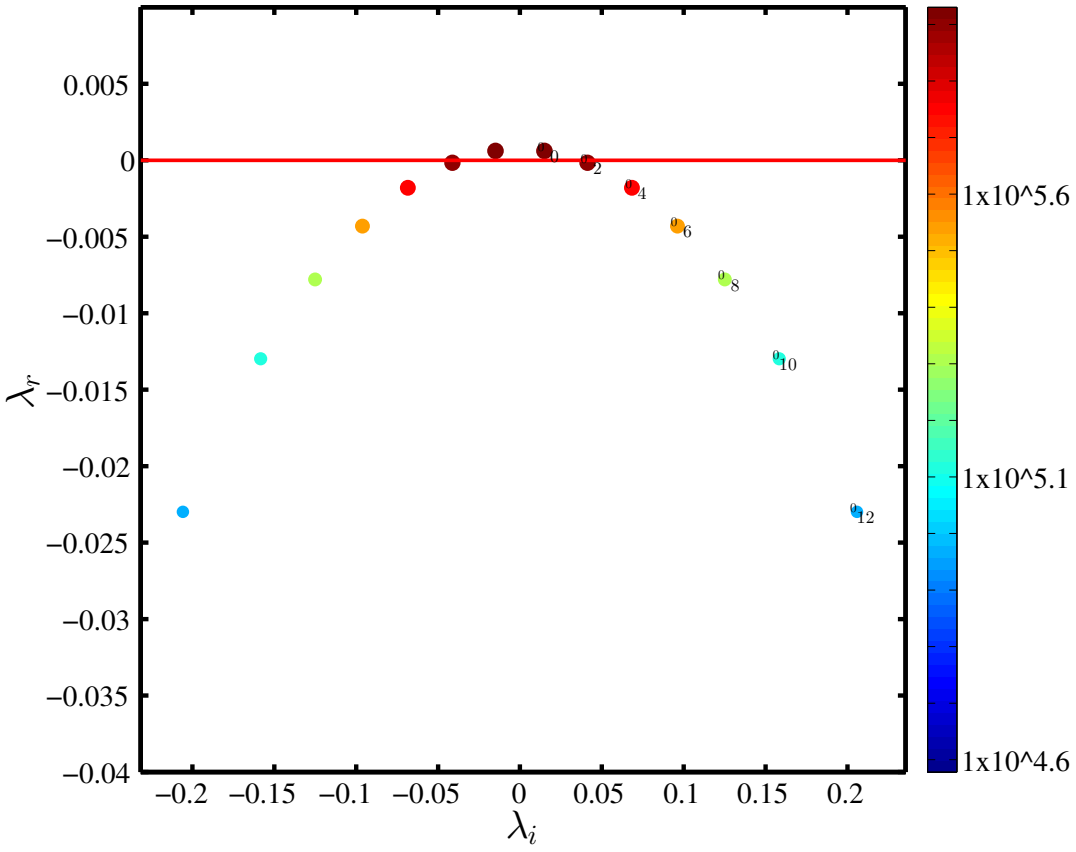

Figure 4.1: The DMD is performed on a simulated solution of Fokker-Planck equation, where a Gaussian-like peak is moving to the negative x direction and diffusing. Since there is only one pattern, or flow constituent, there is only one corresponding smooth curve.

Another important advantage of DMD is the ability to distinguish reproducible

modes from non-reproducible ones. DMD modes associated with reproducible features of a flow will be "robust", i.e., they will be found in multiple realizations of an experiment (for example, the first, middle, and last half of snapshots). In contrast, modes representing non-reproducible flow characteristics will change with the realization. The observation leads to the following conjecture: *it is possible to differentiate reproducible and non-reproducible aspects of a flow by comparing DMD spectra from multiple realizations of a set of nominally identical experiments.* We also observed [13] that some non-robust modes have higher latency than several robust modes, which indicates the failure of POD on this differentiation. Actually, POD can never achieve this goal in that the statistical averages are almost invariant with different set of snapshots $u(\mathbf{x}, t)$. Finally, we observe that in constructing reduced order models, we can discard the non-reproducible features, and only retain their statistical characteristics; in other words, we only need to consider the primary, robust flow constituents in reduced order models.

Another observation regarding DMD modes is that although $|a_i(t)|$ is highly irregular due to experimental noise, its "phase" is very regular

$$\theta_i(t) = \frac{\arctan \frac{\mathrm{Im}(a_i(t))}{\mathrm{Re}(a_i(t))}}{S(i)}, \tag{4.16}$$

where $S(i)$ is the spatial symmetry of the i^{th} dynamic mode (see examples in Chapter 6). The slope of $\theta_i(t)$ and the Lissajous curves $\sin\theta_i(t)$ v.s. $\sin\theta_j(t)$ can serve as an alternative to the harmonics-of-base-frequency identification of modes, whereas again, this task cannot be done in POD in general.

Bibliography

[1] M. Bergmann, C. H. Bruneau, A. Lollo, Enablers for robust pod models, Journal of Computational Physics 228 (2009) 516–538.

[2] L. Sirovich, Turbulence and the dynamics of coherent structures .1. coherent structures, Quarterly of Applied Mathematics 45 (1987) 561–571.

[3] L. Sirovich, Turbulence and the dynamics of coherent structures .2. symmetries and transformations, Quarterly of Applied Mathematics 45 (1987) 573–582.

[4] L. Sirovich, Turbulence and the dynamics of coherent structures .3. dynamics and scaling, Quarterly of Applied Mathematics 45 (1987) 583–590.

[5] J. L. Lumley, The structure of inhomogeneous turbulent flows, in: Atmospheric Turbulence and Radio Wave Propagation, Nauka, Moscow, 1967, pp. 166–178.

[6] J.-C. Hua, G. H. Gunaratne, S. Kostka, N. Jiang, B. V. Kiel, J. R. Gord, S. Roy, Dynamical-systems analysis and unstable periodic orbits in reacting flows behind symmetric bluff bodies, Physical Review E 88 (2013) 033011.

[7] C. W. Rowley, I. Mezic, S. Bagheri, P. Schlatter, D. S. Henningson, Spectral analysis of nonlinear flows, Journal of Fluid Mechanics 641 (2009) 115–127.

[8] I. Mezic, Analysis of fluid flows via spectral properties of the Koopman operator, Annual Review of Fluid Mechanics 45 (2013) 357–378.

[9] P. J. Schmid, Dynamic mode decomposition of experimental data, in: Proceedings of 8th International Symposium on Particle Image Velocimetry, PIV09-0141, Melbourne, Victoria, 2009.

[10] P. J. Schmid, Dynamic mode decomposition of numerical and experimental data, Journal of Fluid Mechanics 656 (2010) 5–28.

[11] S. Bagheri, P. Schlatter, P. J. Schmid, D. S. Henningson, Global stability of a jet in crossflow, Journal of Fluid Mechanics 624 (2009) 33–44.

[12] W. H. Press, S. A. Teukolsky, W. T. Vetterling, B. P. Flannery, Numerical Recipes in C++: the Art of Scientific Computing, Cambridge University Press, Cambridge, UK, 2002.

[13] S. Roy, J.-C. Hua, W. Barnhill, G. H. Gunaratne, J. R. Gord, Modal decompositions and deconvolution of flow dynamics using proper orthogonal and dynamical mode decompositions, (In preparation).

Chapter 5

Dynamical Systems Analysis and Unstable Periodic Orbits in Reacting Flows Behind Symmetric Blu Bodies

5.1 Introduction

High-Reynolds-number fluid flow [1, 2] and high-momentum combustion [3] are complex flows that couple dynamics on multiple spatial and temporal scales. Typically, large-scale structures are generated by external driving, and small-scale aspects are initiated by energy cascading [1, 2]. These small-scale features are highly sensitive to initial conditions and tiny disturbances and exhibit irregular, non-repeatable behavior; in addition, they affect the large-scale structures via feedback, thus complicating the overall flow as well as its analysis. This sensitive dependence on initial conditions, coupled with the nonlinearity of the underlying physical systems, makes it extremely difficult to conduct theoretical or computational analyses of flows [4, 5]. An alternative approach is to conduct a modal decomposition of experimental data and develop phenomenological models for the flows. The high-resolution, high-frequency data needed for such analyses are becoming more readily available with advances in technology [6]. In this paper, we introduce an approach whereby modal decomposition can be used for phase-space reconstruction and dynamical systems analysis to study large-scale flow and bifurcations therein as well as to extract characteristics of noise and irregular facets of the flows.

The application reported here is for flame-shedding dynamics in high-momentum bluff-body-stabilized flames that are transitioning from near-blow-off to stable and acoustically coupled conditions [7, 8, 9, 6]. The control parameter in the experiment is the equivalence ratio ϕ; i.e., the fuel-to-oxidizer ratio and the corresponding stoichiometric value. The physical systems analyzed are symmetric under reflection

about a line parallel to the flows, and symmetric vortex shedding [10, 11] is observed in the entire range of control parameters. As the equivalence ratio is reduced, the flows develop, in addition, the asymmetric von Karman vortices [6]. The approach outlined here, an extension of the principal-components analysis of Ref. [6], is geared toward the determination of the onset and characterization of the growth of von Karman vortices.

Acoustic instabilities can occur in a combustion environment when heat release and pressure fluctuations become coupled and exceed the system damping [3]. We employ bifurcation diagrams [12] and Lyapunov exponents [13] to quantify the shedding transitions for different flame holders. The information can be used to select flame holders that yield stable flow patterns under modifications in the upstream conditions. Such analyses may be valuable for bluff-body applications where a gross change in behavior is undesirable.

We also compute recurrent (or periodic) orbits embedded in the (state-space) neighborhood of the flows. It has been asserted, and demonstrated through examples, that chaotic motions are dense with unstable recurrent orbits [14, 15, 16, 17] and that dynamical invariants of the chaotic motion can be derived from the eigenvalues of these cycles [14, 18, 19, 20, 21]. The chaotic motion approaches a cycle, follows it closely for some time before moving away, returns close to another cycle, and the process is repeated. In this sense, irregular flows are organized around a "skeleton" of unstable cycles. Methods to extract periodic orbits from chaotic signals and spatio-temporally chaotic flows have been introduced [15, 22] and used to analyze experimental time series [23, 24, 25].

The experiment is described briefly in Section 5.2. In particular, we discuss possible sources of irregularity in the flow and highlight the presence of rapidly evolving small-scale structures. The analysis is presented in detail for flow across a bluff body in the shape of a v-gutter, and results for the remaining shapes are outlined in Section 5.7. The first step in the analysis, given in Section 5.3, is a preliminary temporal/spatial filtering of the flow. In Section 5.4 principal-components analysis [26, 27, 28, 29, 30, 31, 32, 33] and symmetry are used to eliminate some irregular facets and establish the modes associated with the flow. In Section 5.5 we propose a method to quantify the magnitude of the von Karman modes and present the bifurcation diagram in terms of ϕ. We also discuss the dynamics in a reduced phase-space and qualitative changes that accompany the onset of von Karman vortices. Section 5.6 presents the computation of periodic orbits embedded in the flow and their use in characterizing the noise and small-scale irregular facets of the flow. The implications of our analysis are discussed in the concluding section.

5.2 Experiment

Flame studies were conducted within an optically accessible, atmospheric-pressure combustion test section that contains a bluff-body flame holder for flame stabilization. Air is delivered into a 152-mm $\times$ 127-mm rectangular test section at a constant rate of 0.32 kg/s. While the air rate is maintained constant, propane fuel is added and mixed upstream of the flame holder to provide equivalence ratios that vary between $\phi = 0.6$ and 1.1. The flame holder is a v-gutter with a width of 38.1 mm

and an angle of 35^o, which is capable of holding the flame to a blow-off equivalence ratio of $\phi = 0.55$. Additional facility details and detailed flame-holder dimensions are provided in Ref. [6].

Flame-shedding behavior within the test section was studied using high-speed chemiluminescence imaging. Imaging was performed to capture the axial plane of the flames in such a way that the reaction fronts, recirculation zone, and reactant regions could be viewed simultaneously. The imaging setup is shown in Figure 5.1. A Phantom v7.1 camera is used to collect the chemiluminescence emitted from the test section by viewing the axial plane through an angled mirror. This stainless steel mirror with MgF_2 coating provides maximum reflection of emission from 300 to 900 nm and is required for imaging because of space limitations. The camera is equipped with a monochrome CMOS detector set to capture images with a resolution of 496×344 pixels at a rate of 10 kHz. The detector is sensitive only to light ranging from 400 to 900 nm. Therefore OH^* chemiluminescence is not collected, while CH^* and black-body radiation from soot are captured. An 85-mm Nikkor lens with an f-stop of 1.4 is coupled to the camera, resulting in a field of view of 165 mm $\times$ 102 mm within the test section.

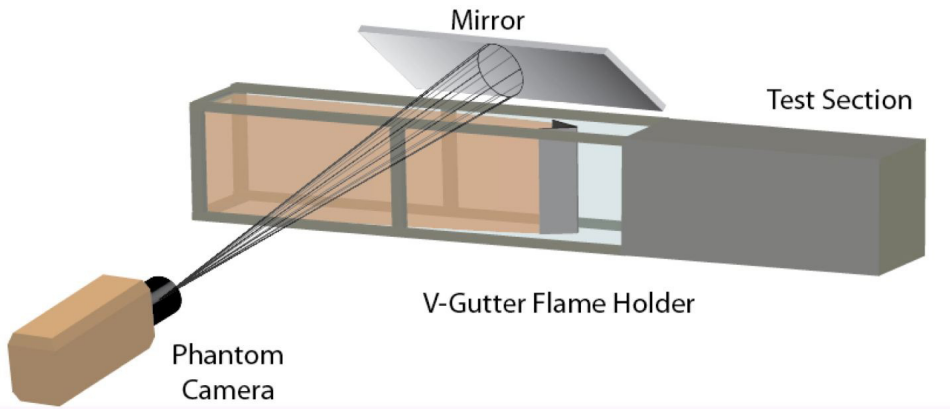

Figure 5.1: Side view of imaging setup with Phantom v7.1 high-speed camera and mirror.

For the present study, imaging of the chemiluminescence from the flame fronts is assumed to be an adequate representation of the flame-shedding mechanism. However, we should point out two drawbacks associated with this technique. First, when imaging flames at reduced equivalence ratios, signals decrease as emission from soot and CH^* is reduced. Although higher camera sensitivity at short wavelengths and enhanced signal could be achieved by increasing the exposure time, the camera has an inherent 95 microsecond frame rate. Since image intensifiers often compromise spatial resolution, we refrain from using them in an attempt to retain as much flame-shedding structure as possible. Signal-to-noise ratios along the reaction front varied from ~ 10 to ~ 20 when the equivalence ratio was changed from $\phi = 0.6$ to 1.1.

The second drawback of chemiluminescence imaging is that signals are collected over a line-of-sight and cannot typically be extended to three dimensions. The current experiment aimed to minimize these effects by establishing, as far as possible, inlet

conditions that were uniform along the depth axis; thus the flame flow would be nearly two dimensional. However, any non-uniformity in the fuel ratio/velocity field or symmetry breaking in the depth direction will result in slight asymmetries in the large structures of the flame. It should be noted that since turbulent flows are inherently three-dimensional, extremely small-scale structures along the shear layers will be captured in our two-dimensional images. Their collection along the line-of-sight of our imaging system will, therefore, contribute to measured flow irregularity and set a lower limit on the structural scales that can be analyzed.

5.3 Time Filtering

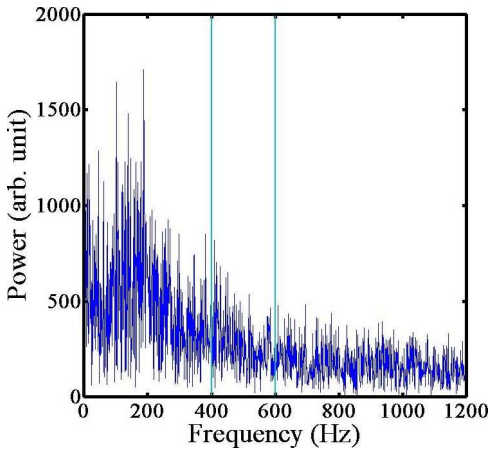

Figure 5.2: Power spectrum of time series for (chemiluminescence) intensities at a point $\mathbf{x}$ for flow at $\phi = 0.7$. Spectrum beyond 400 Hz does not appear to have a structure. Time filtering of the signal is implemented using the filter function given in Eq. (5.1).

First, we perform a preliminary temporal filtering intended to reduce the small-scale structures in regions of large flow gradients. We assume, and the experiment verifies, that the onset and dynamics of these rapidly evolving structures are irregular and may be attributed to line-of-sight imaging effects from the experiment. To filter them, we consider the time sequence $f_{\mathbf{x}}(t) \equiv U(\mathbf{x}, t)$ at a fixed location $\mathbf{x}$. Figure 5.2 displays the power spectrum of such a signal over 1 second of the flow (10,000 frames). The spectral components beyond 400 Hz appear to be irregular. Thus, we filter the signal using the filter function

$$\Theta(f) = \begin{cases} 1 & \text{if } f \ \leq \ 400 \ Hz \\ \frac{1}{2}\left[1 + \cos \pi \frac{f-400}{200}\right] & \text{if } 400 \ Hz < f \leq 600 \ Hz \\ 0 & \text{if } 600 \ Hz < f \end{cases} , \tag{5.1}$$

which retains all spectral components below 400 Hz and smoothly reduces the fraction of spectral components until 600 Hz. The signal is then inverse Fourier transformed to obtain the filtered dynamics at $\mathbf{x}$, and the time-filtered flow is constructed by combining the dynamics at all sites. Snapshots of the original and time-filtered flow at the 500^{th} panel (0.05 s into the video), Figure 5.3, show that some of the rapidly evolving, small-scale features of the flow have been eliminated.

Results of the analyses described below are robust against changes in the filter function. For example, none of the conclusions change if we shift the filter function by (say) 200 Hz. As $\Theta(f)$ is shifted more, it becomes progressively more difficult to compute periodic orbits of the flow.

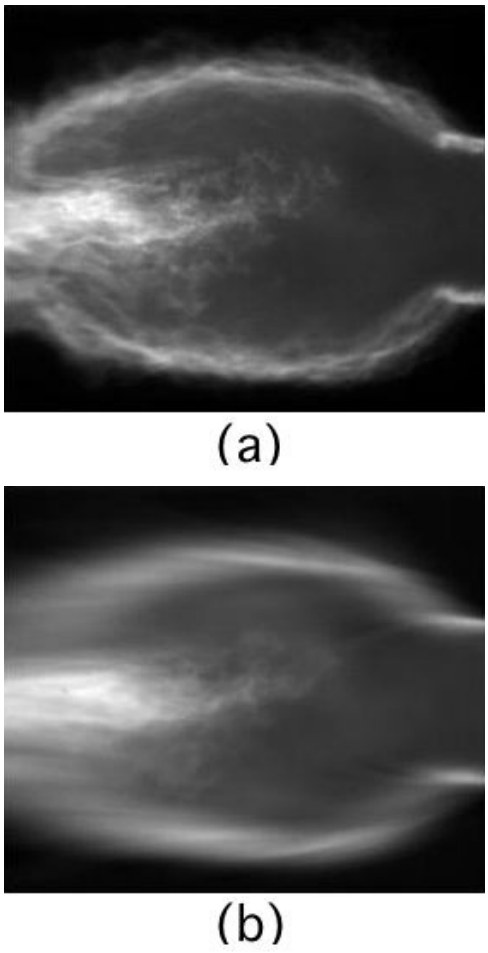

Figure 5.3: 500^{th} panel of original and time-filtered flow, illustrating that the rapidly evolving small-scale motions have been filtered. The size of the images is approximately 100 mm $\times$ 66 mm.

We also implemented spatial filtering as follows: each snapshot was Fourier transformed, and the high wave-vector components filtered. The spatio-temporal dynamics are a composite of these spatially filtered images. The results from the analysis, including the coherent structures, bifurcation diagram, and periodic orbits are similar

under temporal and spatial filtering. We also filtered the spatio-temporal dynamics both spatially and temporally and found comparable results.

5.4 Principal-Components Analysis

5.4.1 Preliminaries

For establishing the large-scale modes of the flow, it is necessary to reduce (or, if possible, eliminate) irregular small-scale features. We employed principal-components analysis (PCA) for this task [26, 27, 28, 29, 30, 31, 32, 33]; its use is facilitated by the presence of a reflection symmetry in the system. Other approaches such as dynamic-mode decomposition [34, 35] may be required for modal decomposition in systems with no such symmetry. The "data" consist of a video recording of the chemiluminescence of $N = 10,000$ successive snapshots of the flow taken at 10 kHz. The analysis is conducted within a region defined by a height H (300 pixels; 100 mm) and a width W (200 pixels; 66 mm) behind the bluff body. We found that oscillations of the mean and standard deviation of the intensity in a frame were (nearly) commensurate with vortex shedding and that the results from the PCA improved when the frame intensities were normalized (to zero mean and unit variance). PCA was implemented on the normalized matrix $U(\mathbf{x}, t)$ of N rows and $H \times W$ columns, where $\mathbf{x} = (x, y)$ and t is time. Here x represents the span-wise direction, and $y = 0$ is the central axis about which the system is reflection symmetric. In PCA this field

is decomposed as

$$U(\mathbf{x},t) = \sum_{k=0}^{HW-1} a_k(t)\Phi_k(\mathbf{x}) \tag{5.2}$$

where $\Phi_k(\mathbf{x})$ $(k = 0, 1, \ldots, HW-1)$ are referred to as the principal components or coherent structures and $a_k(t)$ are their time-dependent coefficients. $\Phi_0(\mathbf{x})$ is the time-averaged field. The coherent structures are normalized and form an orthonormal basis for expansion of the data. The terms in Eq. (5.2) are ordered such that their latencies (also referred to as "energies") $L_n = \langle a_n^2(t)\rangle$ are in non-increasing order. A reduced-order model [36] for the flow can be derived by truncating the series (5.2) at an appropriate order N to obtain an approximation $U_N(\mathbf{x},t) \equiv \sum_{k=0}^{N-1} a_k(t)\Phi_k(\mathbf{x})$. The"quality" of the approximation is given by

$$\beta_N = \frac{\sum_{k=0}^{N-1} L_k}{\sum_{k=0}^{HW-1} L_k}. \tag{5.3}$$

Larger values of β_N correspond to better approximations of the data.

Two modes of flame shedding are well established in these reacting flows behind bluff bodies. In our experiments the more intense is that where a pair of vortices is simultaneously released from the sides of a symmetric bluff body [6]. The symmetry of the flow can be expressed in terms of the reflection operator $\mathcal{R} : (x, y) \to (x, -y)$ as

$$U(\mathcal{R}\mathbf{x}, t) = U(\mathbf{x}, t). \tag{5.4}$$

Now, the uniqueness of the principal-components expansion shows that for a symmetric flow field, $\Phi_n(\mathcal{R}\mathbf{x}) = \Phi_n(\mathbf{x})$ and, hence, that every coherent structure of the expansion is symmetric about the central axis [30, 31].

The second mode of flame shedding is known as von Karman vortex shedding,

where two vortices are shed asymmetrically; specifically, a vortex shed from one side of the bluff body is followed by one shed from the opposite side. The flow field $V(\mathbf{x}, t)$ associated with von Karman shedding satisfies

$$V(\mathcal{R}\mathbf{x}, t + T) = V(\mathbf{x}, t), \tag{5.5}$$

where T is the time interval between successive shedding. If the vortices are shed periodically, T is constant. Because of the time delay T, the coherent structures for the flow are neither symmetric nor anti-symmetric. However, in any (suitably filtered) flow comprises (only) symmetric and von Karman vortex shedding, non-symmetric coherent structures are due to von Karman shedding. We assume that the intensity of the anti-symmetric components is a measure of the strength of the latter.

5.4.2 PCA for Flow at $\phi = 1.1$

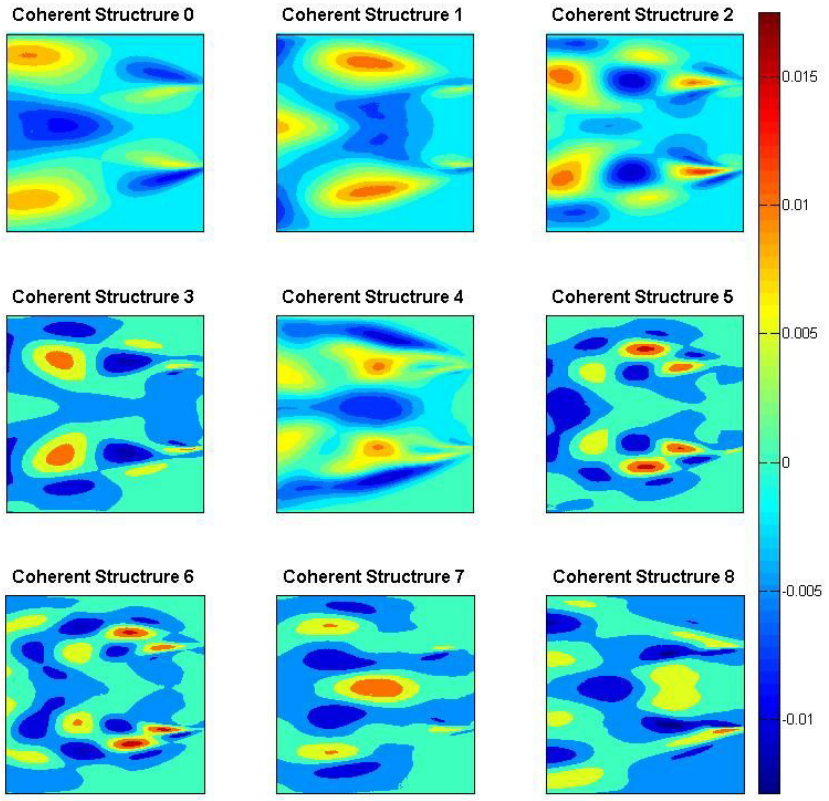

Figure 5.4: First nine coherent structures for flow at $\phi = 1.1$, all of which are nearly symmetric about the horizontal mid-line. Our analysis is predicated on the assumption that asymmetric components of these modes are due to slight experimental non-uniformities and dynamics of the small-scale irregular structures. The scale of individual images, and images in subsequent figures, is approximately 100-mm $\times$ 66-mm.

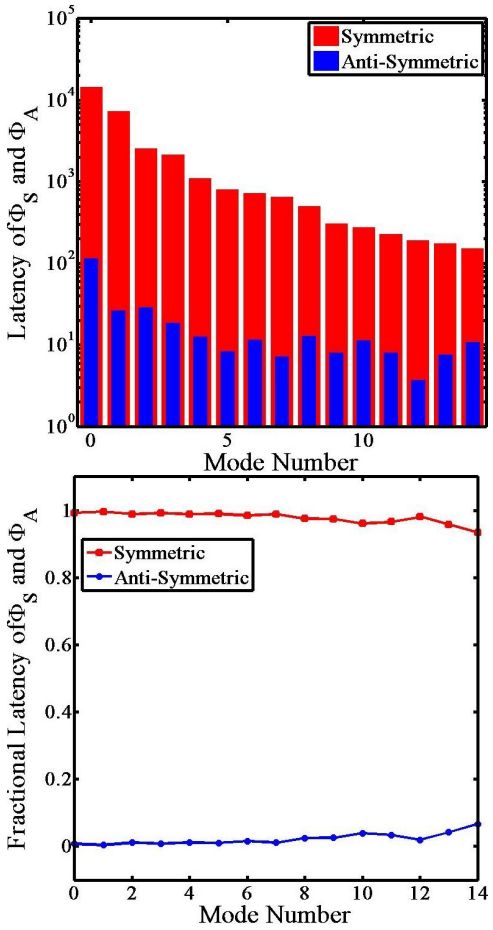

Figure 5.5: (a) Latency and (b) fractional latency of the symmetric (red) and anti-symmetric (blue) components of the first 15 coherent structures. Observe that latencies of the anti-symmetric components are small (by a factor of $\sim$100) compared to those of the corresponding symmetric components. Furthermore, they remain nearly unchanged as the mode number n increases, supporting our assertion that the anti-symmetric components are caused by experimental noise, irregular motions, and/or line-of-sight detection. The fractional latencies of the two components approach each other as n increases, indicating that for large n, the symmetric components are corrupted as well.

Visually, the flow appears to involve only symmetric vortex shedding. The first nine coherent structures, all of which are nearly symmetric about the y-axis, are shown in Figure 5.4. We posit that the small asymmetry in these modes is not due to the large-scale flow, but to experimental noise, irregularities from slight non-uniformities in the upstream inlet conditions, and/or deficiencies in the line-of-sight imaging. We introduce a symmetry-based method to filter some of these aspects.

The symmetric and anti-symmetric components of the n^{th} coherent structure $\Phi_n(x, y)$ are

$$\begin{aligned} \Phi_{n,S}(\mathbf{x}) &= \frac{1}{2}\left[\Phi_n(\mathbf{x}) + \Phi_n(\mathcal{R}\mathbf{x})\right], \\ \text{and} \qquad \Phi_{n,A}(\mathbf{x}) &= \frac{1}{2}\left[\Phi_n(\mathbf{x}) - \Phi_n(\mathcal{R}\mathbf{x})\right], \end{aligned} \tag{5.6}$$

respectively. If our assumption is valid that the small asymmetry in the coherent structures is not due to large-scale flow, then the anti-symmetric component $\langle|\Phi_{n,A}(x)|^2\rangle$, (1) would be small, and (2) would be nearly unchanged between coherent structures. As is evident from Figure 5.5, these expectations were indeed realized. The latency $\langle|\Phi_{n,S}(x)|^2\rangle$ of the symmetric components of the coherent structure decreases significantly with the mode number n, while that of $\langle|\Phi_{n,A}(x)|^2\rangle$ remains nearly unchanged. Furthermore, the fractional latency of $\langle|\Phi_{n,S}(x)|^2\rangle$ is larger by about a factor of 100 for the first few coherent structures. The difference decreases as n increases, signaling the enhanced role of noise (due to reductions in the latency of the coherent structures). Beyond $n \sim 15$, the latencies of the symmetric and anti-symmetric components are similar, and the symmetric components are probably corrupted as well.

Note that we eliminate the anti-symmetric components of the flow entirely in our analysis. Furthermore, we identify the cutoff in the PCA expansion by comparing the intensities of the symmetric and anti-symmetric components. As discussed later in this paper, these modifications to the analysis of Ref. [6] provide a clear identification of the onset of von Karman vortex shedding.

5.4.3 PCA for Flow at $\phi = 0.8$

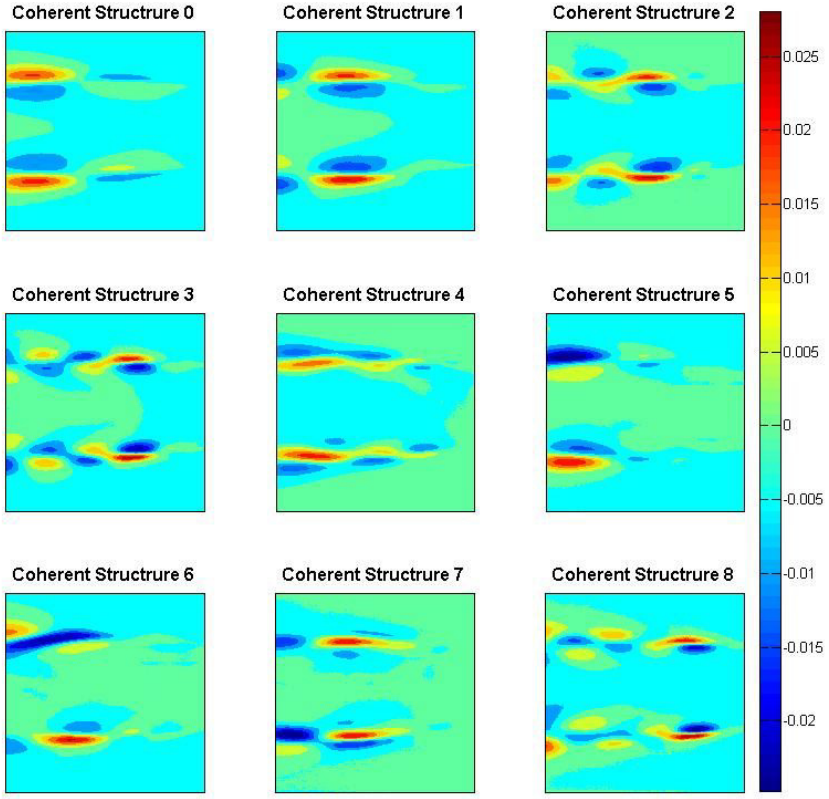

Figure 5.6: First nine coherent structures for flow at $\phi = 0.8$. Modes 5 and 6 (as well as 9 and 12, not pictured) appear to be primarily anti-symmetric.

Although the asymmetry in the flow is not easily observable, PCA selects modes that contain dominant anti-symmetric components (see Figure 5.6). The presence of the asymmetry implies that the motion contains structures outside of symmetric vortex shedding. The analyses of Section 5.4.2 show that the fractional latency of

the anti-symmetric components of Modes 5, 6, 9 and 12 is higher than those of the corresponding symmetric components (see Figure 5.7). Again, we assume that the non-dominant components are noise/irregular-motion-generated and remove them from consideration.

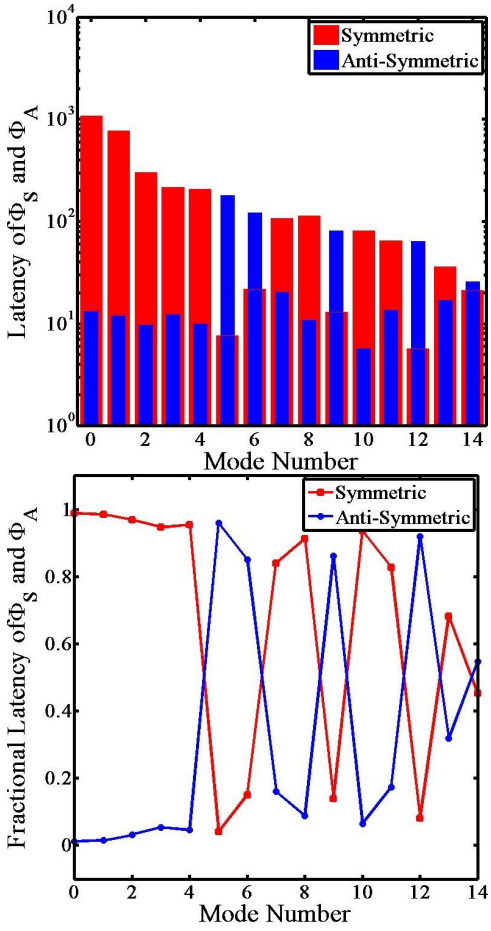

Figure 5.7: (a) Latency, and (b) fractional latency of symmetric and anti-symmetric components of Coherent Structures 0-14 for the flow at $\phi = 0.8$. Note that the dominant components of Modes 5, 6, 9, and 12 are anti-symmetric, suggesting the presence of von Karman vortex shedding.

5.5 Onset of von Karman Vortices: Bifurcation Diagram and Phase Portraits

5.5.1 Bifurcation Diagram

As discussed previously, in the absence of stochastic/irregular effects, the coherent structures of a flow that consists only of symmetric vortex shedding will be symmetric under the reflection $\mathcal{R}$. The anti-symmetric modes are assumed to arise from von Karman vortex shedding. In addition, as in Ref. [6], we assume that the strength of the von Karman vortices can be quantified by the fractional latency of the anti-symmetric coherent structures. The bifurcation diagram, Figure 5.8, shows that anti-symmetric modes appear as ϕ is reduced below 1.0 and that the latencies contained in the anti-symmetric modes increase as ϕ is reduced further. The smooth bifurcation diagram, as compared to the results in Ref. [6], may be attributed to the filtering scheme used in this study.

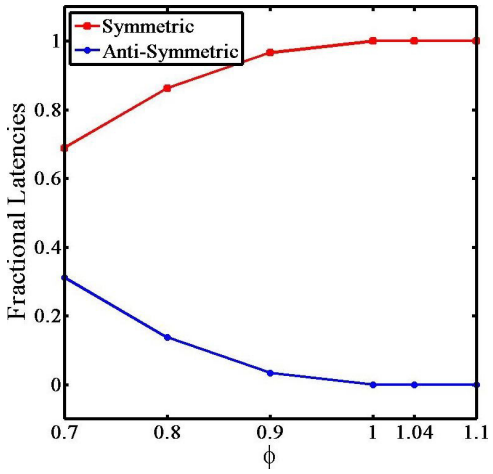

Figure 5.8: Bifurcation diagram for onset of von Karman vortex shedding.

5.5.2 Phase Portraits

The onset of von Karman shedding is accompanied by a re-organization in the configuration space defined by $a_n(t)$, $n = 0, 1, \ldots, 14$. The periodicity, quasi-periodicity, or aperiodicity of an orbit is reflected in the configuration space [4]. In Figure 5.9 we use the projection $(a_0(t), a_2(t))$ for visualization. Orbits prior to the onset ($\phi = 1.1,\ 1.04,\ 1.0$) appear to be noisy recurrent orbits, while those following the onset ($\phi = 0.9,\ 0.8,\ 0.7$) are more irregular (perhaps noisy quasi-periodic orbits). The width of the configuration-space orbits is a measure of the strength of irregular motions. The relatively narrow widths of the orbits at high equivalence ratios are attributed to the flame becoming more uniform across the cross-sectional plane of the rig as a result of acoustic coupling with the oscillating pressure field within the rig.

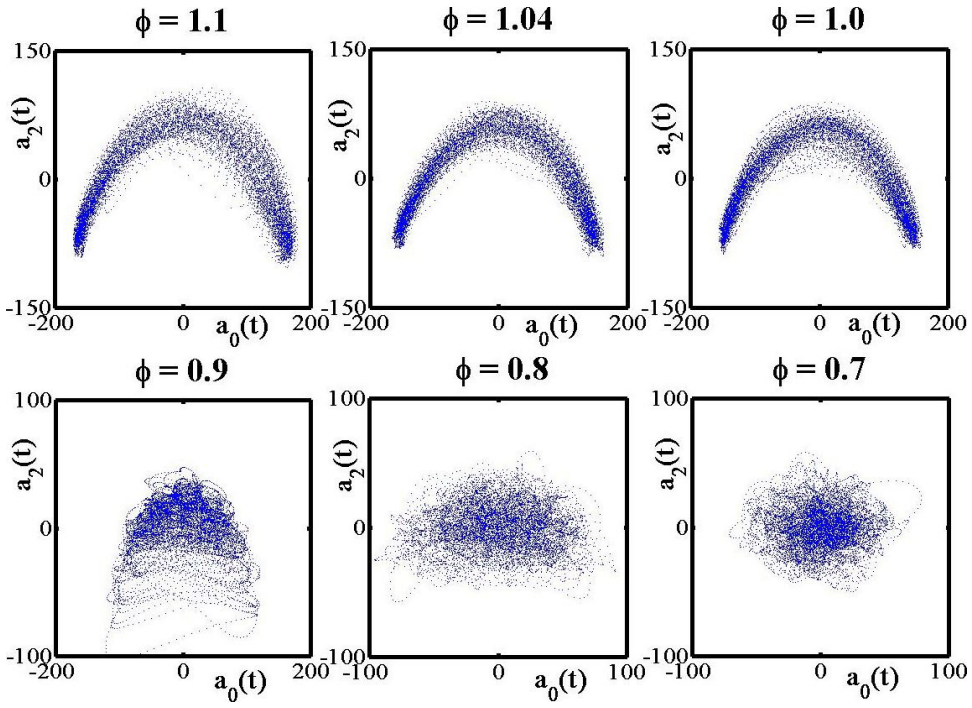

Figure 5.9: Changes in phase portrait [here the projection to $(a_0(t), a_2(t))$] as ϕ changes from 1.1 to 0.7. Transition to the onset of von Karman vortices is accompanied by the change of the phase portrait from an inverted-U structure to a filled-loop structure. Similar changes are observed in other projections as well.

5.5.3 Lyapunov Exponents

One of the defining characteristics of chaotic or irregular flows is the divergence of nearby points in configuration space of the flow [4]. Typically the largest deviations are along the direction of the flow. Lyapunov exponents [13, 4], which quantify the mean expansion of the dynamics along and across the flow, can be used as a measure of the "irregularity" of the flow. Lyapunov exponents and their dependence on the

equivalence ratio are computed using techniques introduced in Ref. [37]. We limit consideration to projections to the $(a_0(t), a_2(t))$ plane. (Variations of the exponent with the equivalence ratio do not depend on this choice.) We choose a small patch of the plane and identify points $\mathbf{x}_i$ of the orbit within it. The point $\mathbf{x}_i$ evolves to a point $\mathbf{y}_i$ (in a different patch) during the next time step (0.0001 s). We assume that the evolution of $\mathbf{x}_i \rightarrow \mathbf{y}_i$ can be approximated by a (locally) linear transformation $\mathcal{L}$, which is estimated by minimizing the least-square difference of $(\mathbf{y}_i - \mathbf{y}_j)$ and $\mathcal{L}(\mathbf{x}_i - \mathbf{x}_j)$, for all pairs of points $\mathbf{x}_i$ and $\mathbf{x}_j$ in the original patch. Now, we follow an orbit, constructing patches at each time step and computing the associated linearizations. The Lyapunov exponent is the logarithm of the largest eigenvalue of the product (per step) as the orbit length increases.

Figure 5.10 shows the variation in the Lyapunov exponent for the flow as the equivalence ratio is changed. The onset of von Karman vortex shedding is accompanied by an increase in the Lyapunov exponent, i.e., neighboring points on the phase diagram diverge faster following the transition.

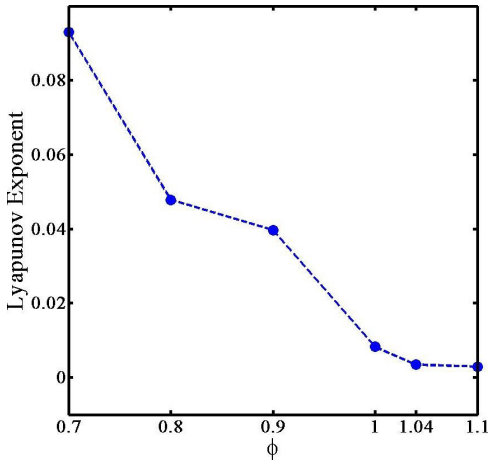

Figure 5.10: Lyapunov exponent of the flow in the range of equivalence ratios studied. Note that the exponent increases with the onset of von Karman vortex shedding.

Fractal properties [38] of an attractor can be used to characterize chaotic motions. However, the correlation dimension [39, 40] of all attractors shown in Figure 5.9 are found to be close to 2. Thus, due to experimental noise and irregular small-scale facets, it is not possible to derive fractal characterizations of our flow.

5.6 Periodic Orbits in the Flow

The computation of (unstable) periodic orbits will be illustrated in the context of bluff-body stabilized flames. As shown below, we find only one periodic orbit prior to the onset of von Karman vortex shedding and two following the transition. Interestingly, the period of the cycle prior to the transition is ~ 8 ms, which is representative of the 125-Hz acoustically coupled flame frequency. The presence of such rapid flow

components highlights the critical need for high-frequency imaging.

5.6.1 Preliminaries

Periodic orbits within the flow are most easily identified using a *Poincaré section*. Qualitative analysis of a dynamical system can be simplified by limiting consideration to intersections of the state-space orbit with a lower dimensional subspace (Poincaré section) that intersects it transversly; i.e., the section is not tangent to the orbit. The map from one such intersection (passing from a given side of the Poincaré section to the other) to the next is referred to as a *Poincaré map* [41, 4] (see Figure 5.11). The Poincaré map is discrete and has one less dimension than the flow.

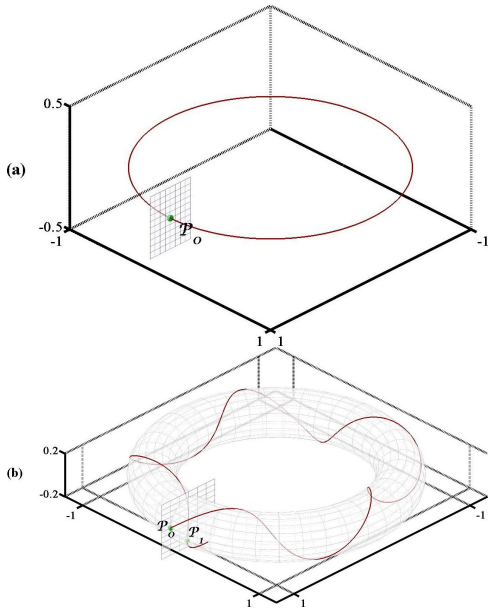

Figure 5.11: Schematic examples of Poincaré maps for flows. (a) Periodic orbit of the flow intersects a single point $\mathcal{P}_0$ on the Poincaré section repeatedly; $\mathcal{P}_0$ is a fixed point of the Poincaré map. (b) Quasi-periodic orbits of the flow intersects the Poincaré section on a curve. Two successive crossings $\mathcal{P}_0$ and $\mathcal{P}_1$ are shown. The Poincaré map $\mathcal{P}_0 \to \mathcal{P}_1$ is quasi-periodic.

In Figure 5.11 we provide two schematic examples. Figure 5.11(a) presents a two-dimensional periodic flow and a Poincaré section $y = 0$. The flow intersects the section at the same point $\mathcal{P}_0$ repeatedly; $\mathcal{P}_0$ is a fixed point of the Poincaré map. The one-dimensional flow has been reduced to a zero-dimensional map. The second example, illustrated in Figure 5.11(b), is a quasi-periodic flow on a torus. Its intersections with the Poincaré section lie on a circle, and the Poincaré map is quasi-periodic on the circle (i.e., similar to an irrational rotation). Here, the

two-dimensional, quasi-periodic flow has been reduced to a one-dimensional, quasi-periodic Poincaré map. Similarly, a chaotic flow will be reduced to a chaotic map of one less dimension on the Poincaré section, and the (closure of the) intersection will be a strange attractor [4].

Being unstable, periodic orbits are not directly observable; their presence and location must be inferred from the flow. To perform this task, we first note that nearby points in chaotic or irregular flows will diverge (the "butterfly effect"). The divergence is large along one direction, the mean growth rate being the (first) Lyapunov exponent [13]; typically, the divergence of the flow normal to the chaotic attractor (or the second Lyapunov exponent) is smaller. Consequently, an orbit that approaches close to a fixed point on the Poincaré section will maintain proximity to the corresponding periodic orbit of the flow for a finite time interval. Hence, a point sufficiently close to a fixed point of a Poincaré map is likely to make a close return [14, 23]. We search for all such close returns on the Poincaré section. Typically, such points cluster into a few groups, each of which is assumed to be associated with a fixed point of the Poincaré map; the fixed point is estimated to be the centroid of the cluster [23].

5.6.2 Periodic Orbits for $\phi = 1.1$

We select the Poincaré section $a_1(t) = 0$ for our analysis and search for crossings from $a_1 < 0$ to $a_1 > 0$. The data (which are available only on a discrete set of time points, i.e., the frames) are interpolated using a third-order spline to estimate the

crossing time t_c. The value of each remaining coefficient $a_n(t_c)$ $(n = 0, 2, \ldots, 14)$ at the crossing is also computed using a spline fit.

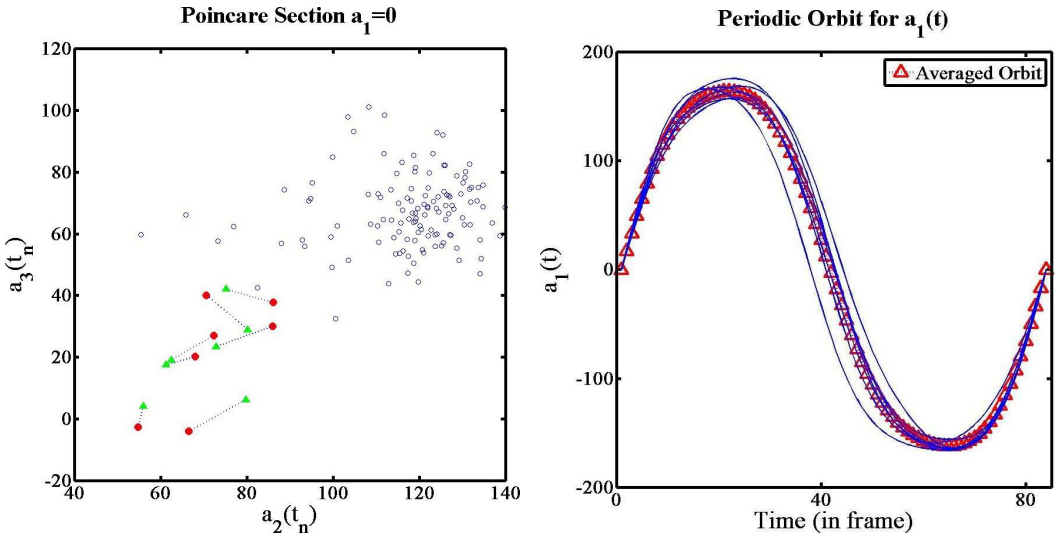

(a) (a) (b) (b)

Figure 5.12: (a) Intersections of the flow at $\phi = 1.1$ with the Poincaré section $a_1 = 0$. First crossings for close returns, defined by $\varepsilon = 0.01$, are shown by red closed circles, while returns to the section are shown by green closed triangles. Dashed lines join pairs of first crossings and returns; i.e., represent the Poincaré map. Open circles are the remaining crossings of the orbit with the Poincaré section, whose returns are farther than ε from the first crossing. (b) Dynamics of $a_1(t)$ between the first crossing and return for the seven close returns identified in (a). All seven appear to be organized around a single periodic orbit. The cycle, marked by red triangles, is estimated to be the mean of the seven close returns.

Our analysis was conducted on the reduced-order flow defined by using the first 15 coherent structures. Close returns on the Poincaré section are defined as orbits that

return to within a pre-specified distance $\varepsilon = 0.01$ from the first crossing. (Identical periodic orbits are found for a range of ε values.) Figure 5.12(a) shows the intersections of the periodic (or quasi-periodic) orbit of the flow (at $\phi = 1.1$) with the Poincaré section. When there is a close return, we mark the first crossing with a red circle and its iterate with a green triangle. Each such pair is connected by a dashed line. The blue open circles denote crossings whose iterates (i.e., next crossings) do not fall within ε. We find seven close returns of the Poincaré map. Notice that all seven first crossings (red circles) are clustered in one neighborhood; we assume that the proximity of their returns is due to the presence of a fixed point on the Poincaré section, and its location is estimated by the mean of the seven first crossings.

Next, we discuss an inference that can be made on the basis of the presence of only one periodic orbit in the flow. If the flow were chaotic, one would expect multiple periodic orbits to be embedded in the attractor and the orbit to follow distinct cycles in the course of the flow [15, 18, 14]. In this scenario, several periodic orbits would have been extracted by our algorithm. Our inability to find more than one orbit is the first indication that the large-scale flow, in the absence of noise and other irregular facets, is periodic and not chaotic; it also confirms that our flame oscillations are indeed acoustically coupled to the experimental rig.

Next, we consider the flows emanating from each of the seven first crossings [red circles in Figure 5.12(a)] and compute their dynamics at regular time intervals (using spline-fits as necessary). The dynamics of $a_1(t)$ for the seven orbits are shown in Figure 5.12(b). The proximity of the seven orbits justifies our assumption that the close returns are caused by a single neighboring periodic orbit. The location of

the periodic orbit $a_1^{(P)}(t)$ at time t is assigned as the centroid of the seven orbits at t. (Note that the periods of the seven close returns, although similar, are not identical. To compute the cycle, we linearly scale the period of each orbit so that all orbits have a common period.) The estimated periodic orbit is shown by red circles in Figure 5.12(b). Figure 5.13 displays two projections of the recurrent orbit.

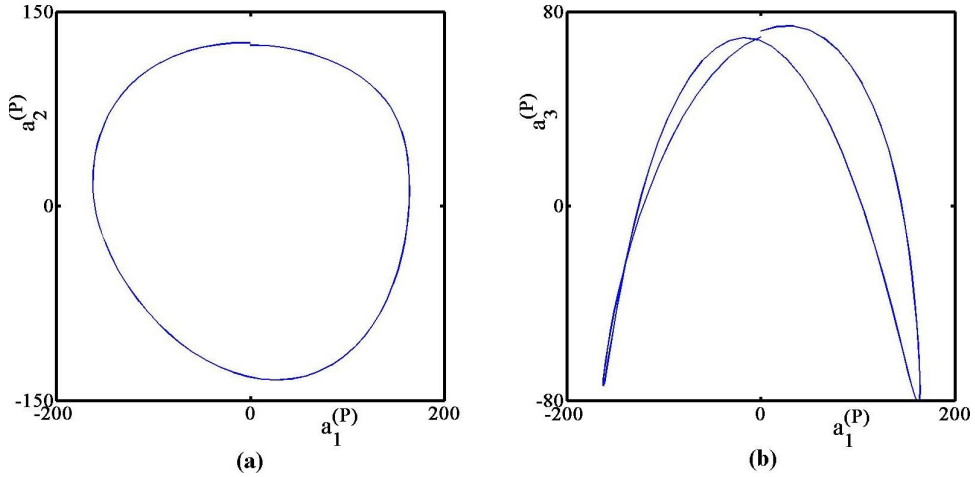

Figure 5.13: Projections of the periodic orbit of the flow at $\phi = 1.1$ to the (a_1, a_2) and (a_1, a_3) planes.

Analysis of the remaining flows prior to the onset of von Karman vortices (i.e., at $\phi = 1.04$ and $\phi = 1.0$) yields qualitatively similar results. Specifically, we find only one cycle in each case, and as can be seen from Figure 5.14 for $\phi = 1.04$, the periodic orbits for the three cases are qualitatively similar.

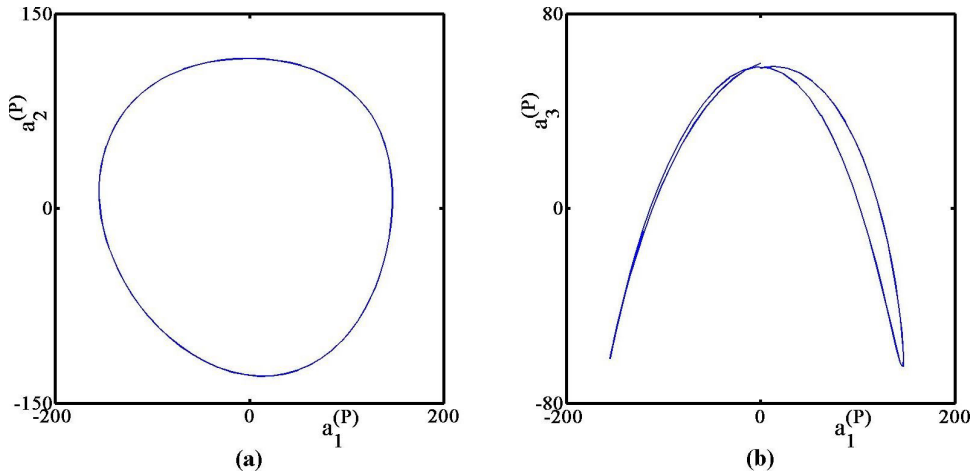

Figure 5.14: Projections of the periodic orbit of the flow at $\phi = 1.04$ to the (a_1, a_2) and (a_1, a_3) planes. Note that the projections are qualitatively similar to those for the flow at $\phi = 1.1$ (see Figure 5.13).

5.6.3 Periodic Orbits for $\phi = 0.8$

Poincaré sections for each flow beyond the onset of von Karman vortices (i.e., $\phi < 1.0$) show two clusters of close returns. A periodic orbit is associated with each cluster. Furthermore, the pairs of orbits for all equivalance ratios beyond the onset are qualitatively similar. Figure 5.15 shows the same pair of projections for each cycle for the flow at $\phi = 0.8$.

Beyond the onset of von Karman vortices, the flow is organized around two periodic orbits. Figures 5.15(a) and (b) show two projections of the first cycle and Figures 5.15(c) and (d) those of the other. Notice that the orbits do not close precisely because the centroid of the locations of the first crossings of the close returns are,

although nearby, not identical to those of the images.

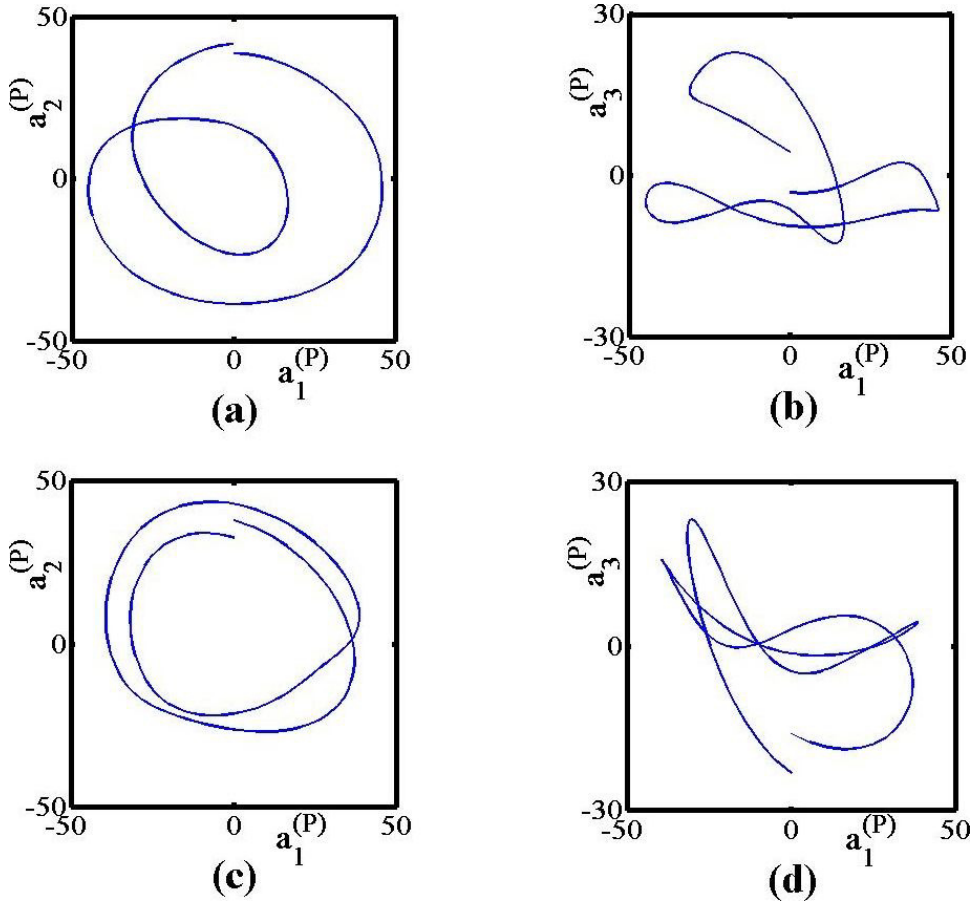

Figure 5.15: Projections of two periodic orbits of the flow at $\phi = 0.8$ to the (a_1, a_2) and (a_1, a_3) planes. (a) and (b) show projections of one cycle and (c) and (d) those of the other.

5.6.4 Unstable Periodic Orbits for the Flow

Thus far, we have the computed periodic orbits of the reduced model defined from the dynamics of the coefficients $a_n^{(P)}(t)$ of the first fifteen coherent structures. An

approximation to the corresponding flow itself can be derived using Eq. (5.2), i.e.,

$$U_P(\mathbf{x}, t) \approx \sum_{n=0}^{15} a_n^{(P)}(t)\Phi(\mathbf{x}). \tag{5.7}$$

Figure 5.16 provides snapshots (at the same time) to compare the original flow and the periodic (or recurrent) flow (i.e., the flow computed from the recurrent orbit). Note that the original flow contains small-scale structures and other irregular features, while the recurrent flow exhibits neither. In fact, a video of the same recurrent flow, provided in Supplementary Materials, shows an extremely clean flow that returns to its initial state following the shedding of a symmetric pair of vortices.

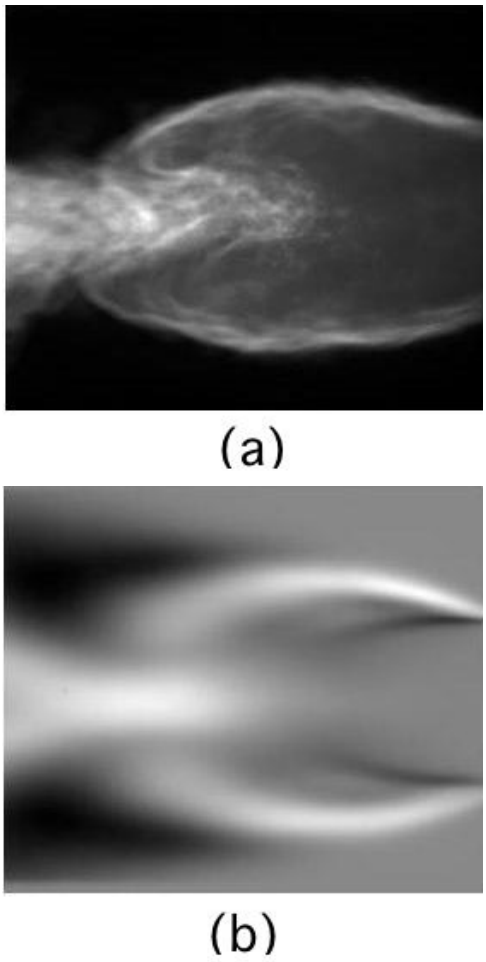

Figure 5.16: Simultaneous snapshots of (a) the original flow at equivalence ratio $\phi = 1.1$, and (b) recurrent flow. Note that the former contains noise and other irregular small-scale structures. The size of the images is approximately 100-mm $\times$ 66-mm.

The flame flow following the onset of von Karman vortices (i.e., for $\phi < 1$) can be de-convoluted in the same manner. Figures 5.17(a) and (b) show a snapshot of the flow at $\phi = 0.8$ and the corresponding snapshot of the recurrent flow. Observe that

the periodic flow does not have up/down symmetry. Figures 5.17(c) and (d) show the symmetric and anti-symmetric components of the latter.

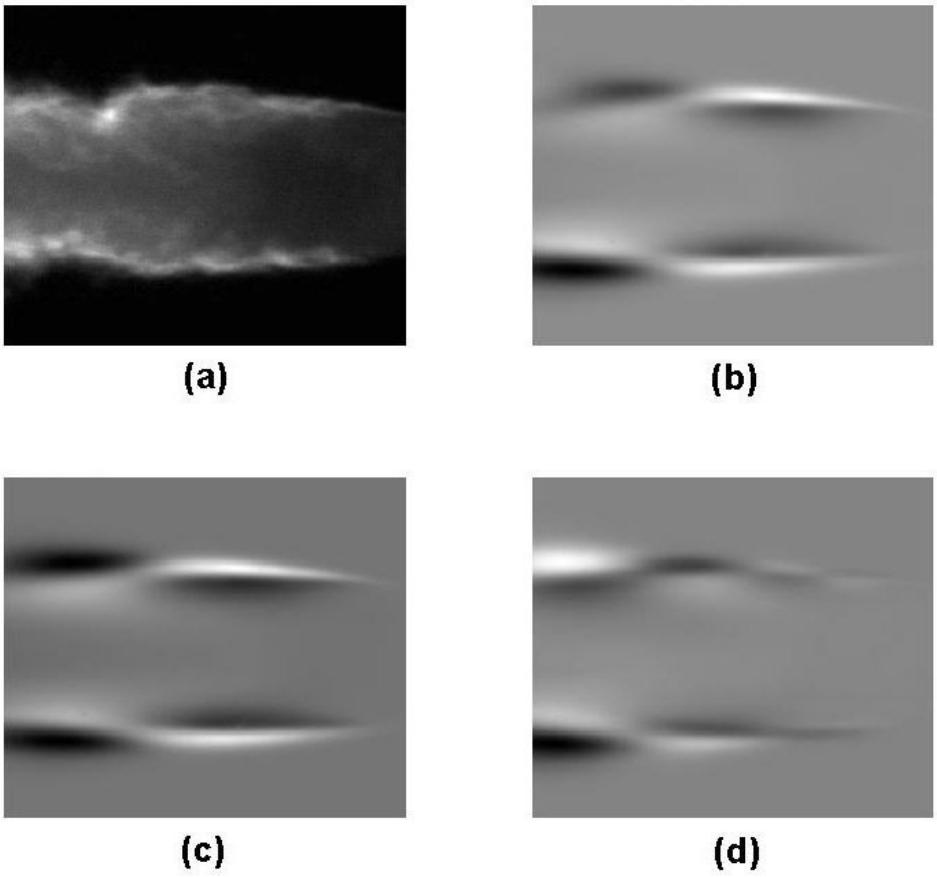

Figure 5.17: Simultaneous snapshots of (a) the flow at equivalence ration $\phi = 0.8$ and (b) recurrent flow. Symmetric and anti-symmetric components of the latter are given in (c) and (d) respectively.

The reconstruction of the periodic flow allows us to characterize the noise and

some other irregular features of the flow (an alternative to looking at PCA reconstruction in Ref. [6]). Specifically, the irregular facets can be defined as the difference between the original flow and the recurrent flow within the duration of the cycle. Figure 5.18 contains snapshots of the difference for four close returns used in computing the periodic flow at $\phi = 1.1$. Specifically, we consider four close returns and select a pre-specified point in state space (see Figure 5.13). We identify the corresponding snapshot of the flow and subtract the image of the recurrent flow from it. Two observations are in order: (1) The irregular motion is concentrated near the flow locations of large velocity gradients. This is to be expected since small-scale structures are generated by energy cascading, which is concentrated at locations with high velocity gradients, and (2) the precise deviations from the periodic flow depend on the specific close return analyzed. This justifies our nomenclature –irregular motion– for these small-scale facets of the flow. However, all four images appear to have similar qualitative features.

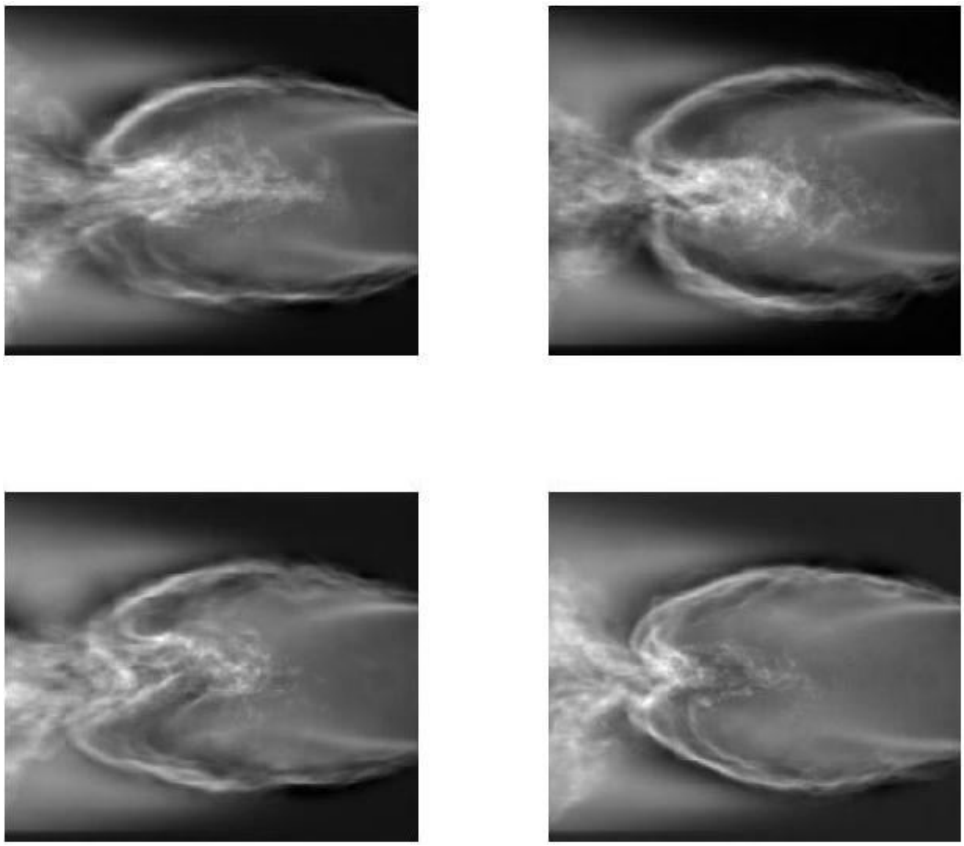

Figure 5.18: Differences in images from equivalent time points of four close returns and corresponding snapshots of periodic flow at $\phi = 1.1$. Images represent noise and other irregular facets of the flow. Note that the images have "similar" statistical features, but the precise structures depend on the close return.

One of the remaining tasks is to provide a comprehensive (and quantitative) statistical characterization of these irregular structures and their dynamics. We have conducted a pair of standard tests. First, the spectrum for the noise decays as a power-law in frequency, suggesting that the small-scale structures are not governed

by low-dimensional chaos [42]. Second, PCA of the corresponding spatio-temporal dynamics shows a slow decay of the latencies. Thus, a large number of coherent structures is needed to provide a good approximation to the noise. This pair of results indicates that the small-scale irregular flows are either stochastic or governed by high-dimensional dynamics.

5.7 Flow behind Other Symmetric Bluff Bodies

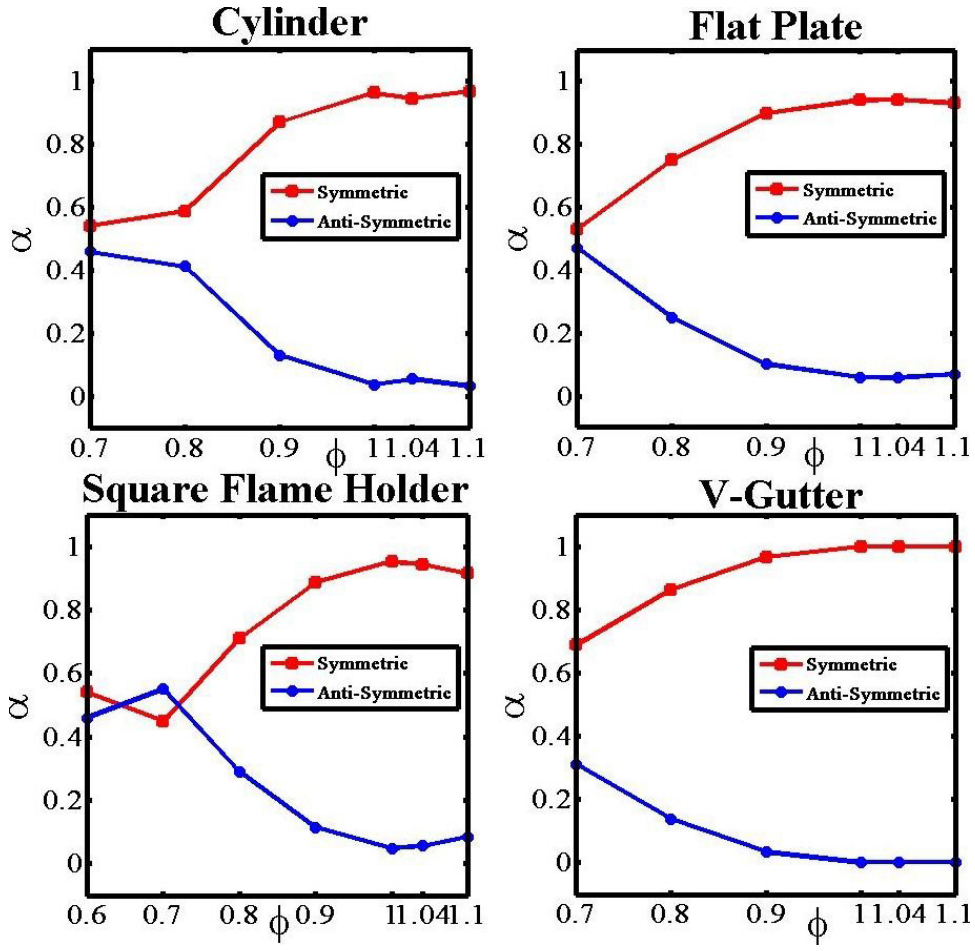

Figure 5.19: Bifurcation diagrams for onset and growth of von Karman vortex shedding with decreasing ϕ for bluff bodies of several shapes. In each case the bifurcation appears between equivalence ratios $\phi = 0.9$ and $\phi = 1.0$.

We highlight a collection of results derived from the analysis of reacting flows behind bluff bodies of other (symmetric) shapes. The analyses are identical to that described

in Sections 5.3–5.6. Flow characteristics remain unchanged, but the strength of the irregularities differs, being smallest for the v-gutter bluff body.

Figure 5.19 displays the bifurcation diagrams for the flow behind (a) cylindrical, (b) flat, (c) square, and (d) v-gutter bluff bodies. In each case, the estimated onset of von Karman vortices occurs at an equivalence ratio between $\phi = 1.0$ and $\phi = 0.9$. However, the growth of the anti-symmetric component following the onset (i.e., smaller ϕ) is smallest for the v-gutter and largest for the square flame holder. This may suggest that the bluff body in the shape of the v-gutter perturbs the flame flow minimally as the equivalence ratio is reduced below the onset of von Karman vortex shedding. Another factor that may be contributing to the shapes of the curves in Figure 5.19 is the acoustic coupling. It appears that, for square and cylindrical flame holders, the transition to acoustically coupled flames does not begin for $\phi < 0.7$ and $\phi < 0.8$, respectively. Differences in the downstream pressure field may prevent the coupling of the flames at these low equivalence ratios. However, once the equivalence ratio is increased, the transition to acoustically coupled conditions appears to be more abrupt. This sensitivity to equivalence ratio may prove to be problematic for active control systems that may not have sufficient time to alter upstream conditions to reduce or prevent the coupling. The frequency bandwidth of the pressure and heat-release fluctuations may be used in the future to understand how the differences in coupling could be caused by the overlap.

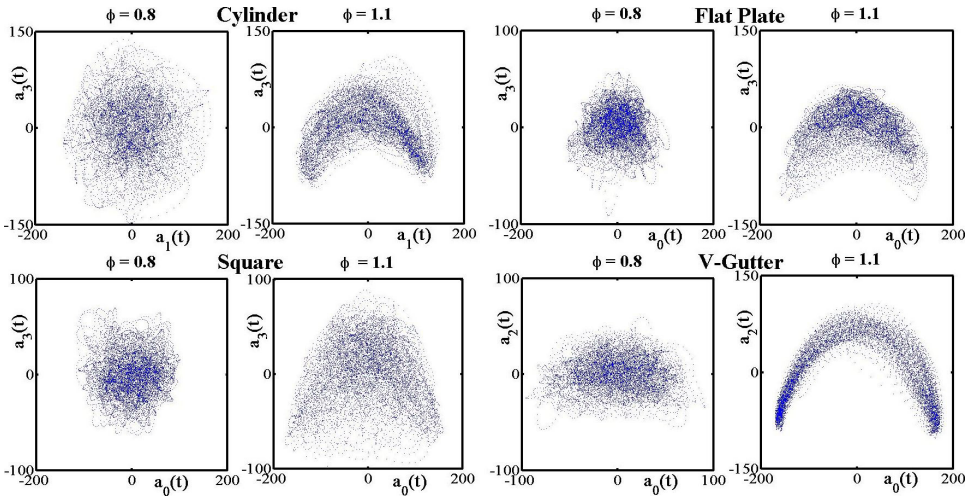

Figure 5.20: Projections to a subspace defined by two eigenvectors illustrate changes of the phase portrait prior to and following the onset of von Karman vortex shedding for four bluff bodies. Images suggest that the flow behind the v-gutter contains the least noise/irregularities.

Figure 5.20 shows projection to the (a_0, a_2) and (a_0, a_3) planes of the phase portrait prior to (i.e., larger ϕ) and following (i.e., smaller ϕ) the onset of von Karman vortex shedding for the four bluff bodies. Once again, it appears that the symmetric flow behind the v-gutter contains the lowest level of noise. The low noise in the v-gutter is in agreement with the fact that the symmetric energy for the v-gutter is highest in Figure 5.21 (see below). This suggests that heat-release fluctuations and shedding behind the v-gutter couple best with the pressure fluctuations in the rig. The remaining bluff-body shapes with more irregular shedding (symbolized by phase portraits with more irregularity) probably inherently provide additional damping of the acoustics [43].

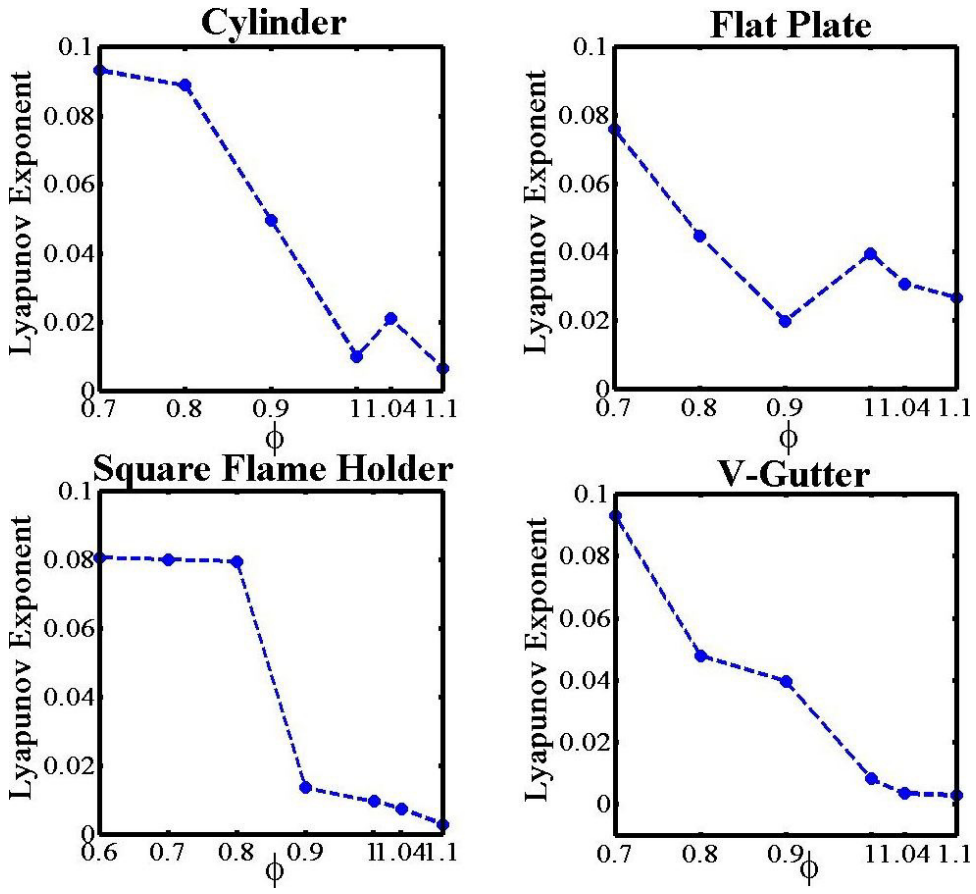

Figure 5.21: Growth of Lyapunov exponents for flow behind four bluff bodies as the equivalence ratio is reduced. Expansion rates for flow behind cylindrical, square, and v-gutter bluff bodies are similar. Flow behind the flat plate shows different behavior.

The flows behind all symmetric bluff bodies exhibit similar qualitative behavior both prior to and subsequent to the onset of von Karman vortex shedding, as can be observed from the phase portraits (Figure 5.20), Lyapunov exponents (Figure 5.21), and periodic orbits (Figure 5.22), although the second set of cycles for the flow behind the cylinder appear different. However, the flow behind the v-gutter exhibits

the least irregularity, confirming a more efficient coupling of the flame heat release with the acoustic field in the rig.

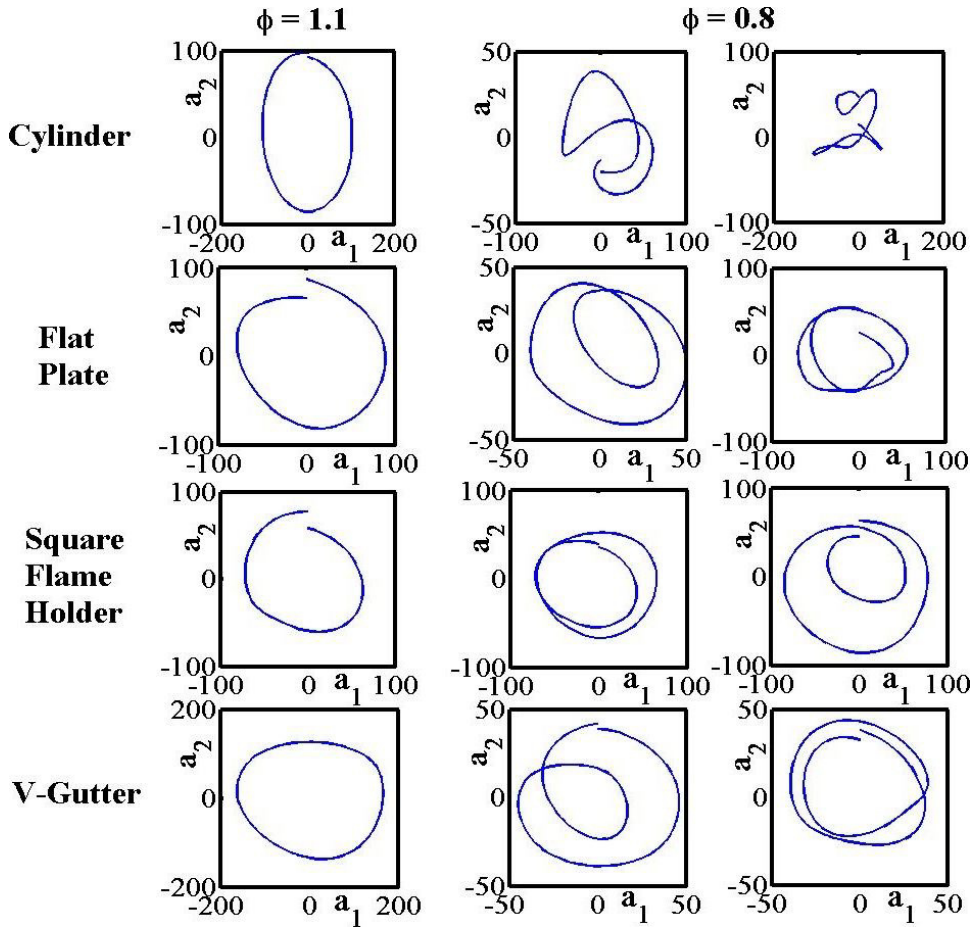

Figure 5.22: Periodic orbits prior to and subsequent to the onset of von Karman vortex shedding for the flow behind the four bluff bodies.

We find a larger number of close returns for the flow behind the v-gutter, which once again suggests that this flow is the most regular. In addition, periodic orbits for the flow behind other bluff bodies fail to make (sufficiently) close returns. For

example, for $\phi = 1.1$, we find five, four, and four close returns for the flow behind the cylindrical, flat, and square bluff bodies, respectively. We find only two periodic orbits for each flow following the onset, and they are similar for the flat plate, the square flame holder, and the v-gutter. The orbits for the lower equivalence ratio in Figure 5.22 also suggest that the cylindrical flame holder provides the least amount of acoustic coupling since the returns are farthest away there. However, we find the same number of periodic orbits (one prior to the onset -large ϕ- and two following the onset -small ϕ-) for the flow behind each bluff body.

5.8 Discussion and Conclusions

Enhancing the performance of combustion systems such as engines requires designs to minimize or delay flow instabilities. Unfortunately, higher efficiencies occur in leaner fuel/air mixtures –the very regime where flow instabilities are initiated. Theoretical approaches to addressing these issues encounter serious obstacles. Fundamental equations of fluid dynamics and chemical kinetics are nonlinear, and flow characteristics depend sensitively on their precise form and the values of control parameters and boundary conditions. Perturbation approaches also fail to yield reliable results in intensely driven nonlinear systems. In contrast, experimental techniques, particularly methods for extracting ultra-high-frequency, high-resolution flow patterns, have undergone rapid advances in recent years. Thus, the need is critical for data-based reduced-order models to analyze and control flow instabilities.

In this study, we introduced a modal decomposition of bluff-body-stabilized combustion flows. The energy in these flows is introduced through large-scale external actions, acoustic instabilities, or vortex shedding. In addition, the flow contains irregular, small-scale motions created through viscous-mediated energy cascading. These small-scale motions feed back and impose irregularities on the large-scale flows as well. Some of the questions that motivated our study were: 1) Are large-scale flows regular in the absence of feedback from the small scales? 2) If so, can transitions in these flows be identified and characterized? 3) What are the statistical descriptions appropriate to the small-scale flows?

We focused on high-momentum combustion behind bluff bodies under conditions that include symmetric vortex shedding. As the equivalence ratio of the mixture is reduced, the flow undergoes a transition beyond which the flow sheds von Karman vortices as well [6]. Since von Karman modes are observed at small equivalence ratios and will only increase with the upstream temperatures [44], their onset may signal the limits in optimizing the efficiency of engines, and designs that delay their onset may prove useful in enhancing engine efficiency.

The methods outlined in this paper are extensions of the proper orthogonal decomposition introduced in Ref. [6]. All experimental systems we analyzed had a reflection symmetry about an axis along the flow direction. Symmetric vortex shedding retains this symmetry, while von Karman shedding breaks it. Our deconvolution of the flow relied on this observation: First, when the vortex shedding is symmetric, all coherent structures in the expansion are necessarily symmetric under reflection;

hence, any asymmetry in the computed coherent structures is due to noise and irregular feedback from the small-scale motions. This observation provides a measure of the irregular motions and an algorithm for filtering them. Second, when the flow contains von Karman shedding as well, the strength of these vortices can be quantified by the anti-symmetric components of the coherent structures.

These assertions were used to identify the onset and growth of von Karman vortex shedding. The onset is illustrated with bifurcation diagrams and qualitative changes in the phase-space orbits. The growth of von Karman modes is characterized using bifurcation diagrams and Lyapunov exponents. We further characterized the transition by computing the (unstable) periodic orbits embedded in the flow. We found only one such orbit prior to the onset of von Karman vortices and a pair of orbits following the transition.

The presence of only one or two periodic orbits in the flow has an important consequence. If the flows were chaotic, one would expect multiple periodic orbits to be embedded in the attractor [15, 18, 14], and our algorithm would have yielded several periodic orbits. Our inability to find more than one orbit prior to the transition suggests that the large-scale flow is periodic (not chaotic) and that the irregular facets of the flow probably result from feedback from the small scales. The vanishing of the Lyapunov exponent for $\phi \geq 1$ provides additional evidence for the periodicity of the large-scale flow. These results are consistent with estimates made from flow characteristics. The cross-sectional area (approximately 150 mm $\times$ 125 mm) and the velocity (approximately 14 m/s) provide an estimate of the Reynolds number of 3×10^5, which is below the transition to turbulent flow for a cylindrical barrier [45],

once again suggesting that the primary flame flow is not irregular.

We conducted the analysis for bluff-body-stabilized flow behind flame holders of four (symmetric) shapes. The qualitative features for the flows are similar in each case, although the level of irregularity depends on the specific shape of the flame holder. We found that the onset of von Karman shedding occurs at (nearly) the same equivalence ratio. However, the flow behind a v-gutter is least irregular and that behind the cylindrical bluff body is most irregular. This observation may assist in optimizing engine design.

Knowledge of the relevant coherent structures and their symmetries can be used to infer the normal-form equations for the underlying spatio-temporal dynamics [12, 46, 4]. These normal forms can be used to predict secondary bifurcations in the system [47, 46]. Such analyses have been conducted for many fluid systems, including cellular flame patterns [48, 49].

Periodic orbits within an irregular flow are especially useful in controlling a chaotic flow [50, 51]. The crucial observation is that since the cycle is embedded in the irregular orbit, it requires only a small perturbation to guide a chaotic system toward the periodic orbit [52, 53]. Furthermore, since the requisite perturbations are small, one may assume that superposition applies; once responses of the system to a collection of perturbations are established, they can be superposed in an appropriate way to obtain a pre-specified response of the system. The method has been successfully applied to control systems as diverse as reaction–diffusion systems [54], flame fronts [54], lasers [55], magnetoelastic ribbons [56], cardiac rhythms [57, 58, 59, 60], and brain signals [61]. One of our future goals is to validate that periodic orbits

within the flow can be used to reduce or eliminate irregular facets of bluff-body-stabilized flames.

The motivation for our work was to de-convolute the complex flame flow into its constituents. In our studies we explicitly used differences in the symmetries between symmetric and von Karman vortex shedding to identify flow patterns associated with each mode. Such partitioning is required because individual structures consists of a combination of coherent structures, rather than a single structure. Unfortunately, this approach cannot differentiate two or more modes with the same symmetry and cannot be used to analyze physical systems (e.g., jet engines) with no symmetry. One option is to use the frequency content of the dynamics to identify coherent structures to be combined into each flow component. Another possibility is to use dynamical mode decomposition [34, 35].

Bibliography

[1] S. Chandrasekhar, Hydrodynamic and Hydromagnetic Stability, Dover Publications, Inc., New York, 1961.

[2] P. G. Drazin, W. H. Reid, Hydrodynamic Stability, Cambridge University Press, Cambridge, UK, 1981.

[3] T. Lieuwen, Modeling premixed combustion-acoustic wave interactions: A review, Journal of Propulsion and Power 19 (2003) 765–781.

[4] M. Cross, P. Hohenberg, Pattern-formation outside of equilibrium, Reviews of Modern Physics 65 (1993) 851–1112.

[5] A. C. Noble, G. B. King, N. M. Laurendeau, J. R. Gord, S. Roy, Nonlinear thermoacoustic instability dynamics in a rijke tube, Combustion Science and Technology 184 (2012) 293–322.

[6] S. Kostka, A. C. Lynch, B. C. Huelskamp, B. V. Kiel, J. R. Gord, S. Roy, Characterization of flame-shedding behavior behind a bluff-body using proper orthogonal decomposition, Combustion and Flame 159 (2012) 2872–2882.

[7] T. Maxworthy, On mechanism of bluff body flame stabilization at low velocities, Combustion and Flame 6 (1962) 233.

[8] S. Chaudhuri, S. Kostka, M. W. Renfro, B. M. Cetegen, Blowoff dynamics of bluff body stabilized turbulent premixed flames, Combustion and Flame 157 (2010) 790–802.

[9] J. Hertzberg, I. Shepherd, L. Talbot, Vortex shedding behind rod stabilized flames, Combustion and Flame 86 (1991) 1–11.

[10] L.-Z. Huang, D.-M. Nie, Vortex shedding patterns in flow past inline oscillating elliptical cylinders, Thermal Science 16 (2012) 1395–1399.

[11] E. Konstantinidis, S. Balabani, Symmetric vortex. shedding in the near wake of a circular cylinder due to streamwise perturbations, Journal of Fluids and Structures 23 (2007) 1047–1063.

[12] M. Golubitsky, D. G. Schaffer, I. Stewart, Singularities and Groups in Bifurcation Theory, Vol. 2, Springer–Verlag, Cambridge, UK, 1988.

[13] J. Froyland, Lyapunov exponents for multidimensional orbits, Physics Letters A 97 (1983) 8–10.

[14] P. Cvitanovic, Invariant measurement of strange sets in terms of cycles, Physical Review Letters 61 (1988) 2729–2732.

[15] D. Auerbach, P. Cvitanović, J.-P. Eckmann, G. Gunaratne, I. Procaccia, Exploring chaotic motion through periodic orbits, Physical Review Letters 58 (1987) 2387–2389.

[16] P. Cvitanovic, Y. H. Lan, Turbulent fields and their recurrences, in: Antoniou, N. G., Diakonos, F. K. and Ktorides, C. N. (Ed.), Correlations and Fluctuations in QCD, Hellen. Minist. Educ.; Hellen. Minist. Cultutre; Univ. Athens; Hellen Org Tourism; Bullet SA, 2003, pp. 313–325, 10th International Workshop on Multiparticle Production, Iraklion, Greece, Jun 8–15, 2002.

[17] Y. Lan, P. Cvitanovic, Variational method for finding periodic orbits in a general flow, Physical Review E 69 (2004) 016217.

[18] P. Cvitanović, G. H. Gunaratne, I. Procaccia, Topological and metric properties of Hénon-type strange attractors, Physical Review A 38 (1988) 1503–1520.

[19] G. H. Gunaratne, I. Procaccia, Organization of chaos, Physical Review Letters 59 (1987) 1377–1380.

[20] G. H. Gunaratne, M. H. Jensen, I. Procaccia, Universal strange attractors on wrinkled tori, Nonlinearity 1 (1988) 157–180.

[21] P. Cvitanovic, Recycling chaos, in: Ferraz, A, Oliveira, F and Osorio, R (Ed.), Nonlinear Physical Phenomena, Int. Ctr. Condensed Matter; Conselho Nacl. Desenvolvimento Cien & Technol.; Int Ctr. Theoret. Phys, Off External Affairs; Ibm. Brazil, 1991, pp. 57–72, School on Nonlinear Physical Phenomena, Brasilia, Brazil, Jul 3-21, 1989.

[22] G. H. Gunaratne, P. S. Linsay, M. J. Vinson, Chaos beyond onset: A comparison of theory and experiment, Physical Review Letters 63 (1989) 1–4.

[23] A. Belmonte, M. Vinson, J. Glazier, G. Gunaratne, B. Kenny, Trajectory scaling functions at the onset of chaos - experimental results, Physical Review Letters 61 (1988) 539–542.

[24] M. Slutzky, P. Cvitanovic, D. Mogul, Deterministic chaos and noise in three in vitro hippocampal models of epilepsy, Annals of Biomedical Engineering 29 (2001) 607–618.

[25] M. Slutzky, P. Cvitanovic, D. Mogul, Identification of determinism in noisy neuronal systems, Journal of Neuroscience Methods 118 (2002) 153–161.

[26] J. L. Lumley, The structure of inhomogeneous turbulent flows, in: Atmospheric Turbulence and Radio Wave Propagation, Nauka, Moscow, 1967, pp. 166–178.

[27] G. Berkooz, P. Holmes, J. Lumley, The proper orthogonal decomposition in the analysis of turbulent flows, Annual Review of Fluid Mechanics 25 (1993) 539–575.

[28] G. Berkooz, P. Holmes, J. L. Lumley, Turbulence, Coherent Structures, Dynamical Systems, and Symmetry, Cambridge Monographs on Mechanics, Cambridge University Press, Cambridge, UK, 1996.

[29] M. N. Glauser, S. J. Leib, W. K. George, Coherent structures in the axisymmetric turbulent jet mixing layer, Turbulent Shear Flows 5 (1987) 134–135.

[30] L. Sirovich, Turbulence and the dynamics of coherent structures .1. coherent structures, Quarterly of Applied Mathematics 45 (1987) 561–571.

[31] L. Sirovich, Turbulence and the dynamics of coherent structures .2. symmetries and transformations, Quarterly of Applied Mathematics 45 (1987) 573–582.

[32] L. Sirovich, Turbulence and the dynamics of coherent structures .3. dynamics and scaling, Quarterly of Applied Mathematics 45 (1987) 583–590.

[33] P. Petersson, R. Wellander, J. Olofsson, H. Carlsson, C. Carlsson, B. B. Watz, N. Boestkjaer, M. Richter, M. Alden, L. Fuchs, X.-S. Bai, Simultaneous high-speed PIV and OH-PLIF measurements and modal analysis for investigating flame-flow interactions in low swirl flames, in: 16^{th} International Symposium on Applications of Laser Techniques to Fluid Mechanics, Lisbon, Portugal, 2012.

[34] P. J. Schmid, Dynamic mode decomposition of numerical and experimental data, Journal of Fluid Mechanics 656 (2010) 5–28.

[35] P. J. Schmid, Dynamic mode decomposition of experimental data, in: Proceedings of 8th International Symposium on Particle Image Velocimetry, PIV09-0141, Melbourne, Victoria, 2009.

[36] M. Bergmann, C. H. Bruneau, A. Lollo, Enablers for robust pod models, Journal of Computational Physics 228 (2009) 516–538.

[37] A. Wolf, J. Swift, H. Swinney, J. Vastano, Determining Lyapunov exponents from a time-series, Physica D: Nonlinear Phenomena 16 (1985) 285–317.

[38] B. Mandelbrot, How long is coast of britain - statistical self-similarity and fractional dimension, Science 156 (1967) 636–638.

[39] P. Grassberger, I. Procaccia, Measuring the strangeness of strange attractors, Physica D 9 (1983) 189–208.

[40] P. Grassberger, I. Procaccia, Characterization of strange attractors, Physical Review Letters 50 (1983) 346–349.

[41] G. Teschl, Ordinary Differential Equations and Dynamical Systems, Vol. 140, Graduate Studies in Mathematics, American Mathematical Society, Providence, RI, 2012.

[42] M. Gorman, M. elHamdi, K. Robbins, Chaotic dynamics near the extinction limit of a premixed flame on a porous plug burner, Combustion Science and Technology 98 (1994) 47–56.

[43] T. Lieuwen, J. Cho, Coherent acoustic wave amplification/damping by wrinkled flames, Journal of Sound and Vibration 279 (2005) 669–686.

[44] P. Mehta, M. Soteriou, A. Banaszuk, Impact of exothermicity on steady and linearized response of a premixed ducted flame, Combustion and Flame 141 (2005) 392–405.

[45] F. P. Incropera, D. P. deWitt, T. L. Bergman, A. S. Lavine, Fundamentals of Heat and Mass Transfer, John Wiley and Sons, Hoboken, NJ, 1990.

[46] P. Coullet, G. Iooss, Instabilities of one-dimensional cellular-patterns, Physical Review Letters 64 (1990) 866–869.

[47] G. Dangelmayr, D. Armbruster, Classification of Z(2)-equivariant imperfect bifurcations with corank-2, Proceedings of the London Mathematical Society 46 (1983) 517–546.

[48] A. Palacios, G. Gunaratne, M. Gorman, K. Robbins, Cellular pattern formation in circular domains, Chaos 7 (1997) 463–475.

[49] A. Palacios, M. Gorman, G. Gunaratne, Modal decomposition of hopping states in cellular flames, Chaos 9 (1999) 755–767.

[50] A. Fradkov, R. Evans, Control of chaos: Methods and applications in engineering, Annual Reviews in Control 29 (2005) 33–56.

[51] S. Narayanan, F. Hussain, Chaos control in open flows: experiments in a circular jet, in: Proceedings of the Fourth AIAA Shear Flow Control Conference, 1997, AIAA Paper No. 97-1822.

[52] E. Ott, C. Grebogi, J. Yorke, Controlling chaos, Physical Review Letters 64 (1990) 1196–1199.

[53] T. Shinbrot, C. Grebogi, E. Ott, J. Yorke, Using small perturbations to control chaos, Nature 363 (1993) 411–417.

[54] V. Petrov, M. Crowley, K. Showalter, Controlling spatiotemporal dynamics of flame fronts, Journal of Chemical Physics 101 (1994) 6606–6614.

[55] R. Roy, T. Murphy, T. Maier, Z. Gills, E. Hunt, Dynamic control of a chaotic laser - experimental stabilization of a globally coupled system, Physical Review Letters 68 (1992) 1259–1262.

[56] V. In, W. Ditto, M. Spano, Adaptive-control and tracking of chaos in a magnetoelastic ribbon, Physical Review E 51 (1995) R2689–R2692.

[57] A. Garfinkel, W. Ditto, M. Spano, J. Weiss, Control of cardiac chaos, Circulation 86 (1992) 217.

[58] A. Garfinkel, M. Spano, W. Ditto, J. Weiss, Controlling cardiac chaos, Science 257 (1992) 1230–1235.

[59] A. Garfinkel, J. Weiss, W. Ditto, M. Spano, Chaos control of cardiac-arrhythmias, Trends in Cardiovascular Medicine 5 (1995) 76–80.

[60] K. Hall, D. Christini, M. Tremblay, J. Collins, L. Glass, J. Billette, Dynamic control of cardiac alternans, Physical Review Letters 78 (1997) 4518–4521.

[61] S. Schiff, K. Jerger, D. Duong, T. Chang, M. Spano, W. Ditto, Controlling chaos in the brain, Nature 370 (1994) 615–620.

Chapter 6

Modal Decompositions and Deconvolution of Flow Dynamics using Proper Orthogonal and Dynamical Mode Decompositions

6.1 Introduction

Combustion instabilities can inflict severe damage in industrial systems and limit their performance [1, 2]. These instabilities are typically generated when a system is driven toward high performance or high efficiency and take the form of uncharacteristically hot or cold spots [2, 3, 4]. Hot spots can cause extensive and irreparable damage in large chemical reactors [4]. Cold patches can extinguish combustion in reactors or jet engines [5]. An important design goal is to prevent or control the onset and growth of combustion instabilities.

A major difficulty of such a design is the lack of a sufficiently accurate and analytically or computationally solvable model system. Reacting flows can, in principle, be modeled using an appropriate system of reaction-diffusion equations [6, 7, 8, 9] supplemented by the Navier-Stokes equations [10, 11]. However, there are several difficulties. First, the precise details of the underlying chemical reactions and values for diffusion rates for products are rarely known. Second, typical flows contain and are effected by long-range pressure and heat release fluctuations. In particular, the zero-Mach number (i.e., fluid speed $\ll$ sound speed) assumption used in most analytical studies is not expected to be valid even in simple configurations [12]. Thirdly, boundary conditions for most technologically relevant examples are non-trivial, and consequently special function expansions cannot be used to reduce the analyses. Computational analyses of reacting flows contain difficulties as well. Nonlinearity of the underlying equations cause energy to be recursively cascaded from large scales to small scales; flow components on the resulting vastly different scales are coupled.

Consequently, an accurate simulation of a combustion flow requires an extremely fine grid on which the computations are to be performed.

On the other hand, high-frequency, high-resolution imaging, such as measurements of temperature fields through *planner laser-induced florescence* (PLIF) and of velocity fields through *particle image velocimetry* (PIV) are becoming available [13, 14]. The data can be used to perform modal decompositions and dimensional reductions of the flows. However, turbulent combustion contains reproducible and non-reproducible components. Random experimental and observational noise can only be quantified statistically. The small scale "eddy-like" structures consequent to energy cascading, while not "random," are not reproducible; they depend sensitively on the initial conditions from which they emerged. Only the reproducible constituents can be used for flow characterization or control. Thus, successful post-processing of turbulent combustion should include techniques to de-convolute the flow into reproducible and non-reproducible constituents.

Nonlinear control methods that rely only on experimental data have been proposed [15, 16] and validated in contexts ranging from cardiac rhythms [17, 18] and laser systems [19] to neural signals [20, 21] and spatio-temporal fluid flows [22]. Specifically, the goal is to drive an irregular system toward a (low-order) unstable periodic orbit [23, 15]. These periodic orbits are contained in the attractor, and hence the feedback necessary to implement control is small. Importantly, the periodic orbits and feedback can be computed from modal decomposition of data [24, 22]; no model of the underlying dynamical system is required.

Typically modal decomposition is implemented using a pre-specified basis expansion, such as Fourier transforms or wavelets, or in the case of linear systems, through global eigenmodes [25, 26]. However, these approaches are not efficient in de-convoluting nonlinear flows contained in irregular domains for two reasons: (a) expansion of flow constituents like eddies or vortices requires a very large number of modes [27], and (b) it is difficult to assign expansion modes to a specific flow constituent, such as the von Karman vortices [13, 28]. Proper Orthogonal Decomposition (POD) addresses issue (a) [29, 30, 31, 32]. First, there is no preconceived selection of the expansion modes; rather, the proper orthogonal modes (or *coherent structures*) are computed from data through a correlation matrix. Next, features of turbulent flows can be captured by $\sim$25 POD modes [13, 28]. The remainder may represent noise and non-reproducible features of the flow. However, in general, it is not possible to use POD to resolve issue (b). (If the system is symmetric, it may be possible to associate symmetry-broken POD modes with symmetry-broken flow constituents [28].) It should be noted that POD is optimal in the sense that, at a given truncation, it provides the closest description of the original flow [32].

In this paper, we analyze reacting flows using POD and an alternative decomposition based on *Koopman eigenfunctions* [33, 26, 34]. The latter are eigenfunctions of the time evolution of a secondary field, such as the experimentally measurable temperature or flow velocity fields. They are a generalization of normal modes [34] and each represents a global collective motion of the secondary field. The spectrum of the underlying dynamics (e.g., reaction-dffusion and Navier-Stokes equations) is contained in the spectrum of the Koopman operator [26, 34]. Schmid [33] proposed

a fast algorithm, referred to as *dynamic mode decomposition* (DMD), to compute approximately (a subset of) the Koopman spectrum from spatio-temporal dynamics of the secondary field.

We study two problems. The first involves spatio-temporal dynamics of a cellular state formed on a flat circular flame front [5]. The state we analyze consists of two "rings" of cells that co-rotate at different rates. We compare and contrast proper orthogonal and dynamic mode decompositions. Both can be used to differentiate dynamics associated with the two rings. However, there are multiple dynamic modes that have the same spatial structure but different growth rates. They combine to form a single proper orthogonal mode. Thus, POD is the more parsimonious or efficient expansion while DMD provides more refined dynamical details of the modes.

The second problem involves reacting flows behind a symmetric bluff-body. The flow contains two types of eddies: periodic shedding of symmetric pairs of vortices and von Karman shedding, where vortices are shed alternately from opposite sides of the bluff body. We show how POD and DMD can be used to differentiate between the two types of vortex shedding.

In these studies, we identify two facets of DMD that are extremely useful in de-convoluting the flow. Unlike proper orthogonal modes, each dynamic mode is associated with a unique complex growth rate. Comparing DMD spectra from multiple nominally identical experiments (or from different segments of the same experiment) helps us identify "reproducible" modes in a flow. Spatio-temporal dynamics represented by the remaining modes may reflect noise and features sensitive to the precise initial conditions. In POD, a corresponding differentiation is attempted using the

latencies (see below) of modes. However, our analyses show that high latency modes of the flow are typically, but not always, reproducible. Thus, it is not possible to differentiate between reproducible and non-reproducible modes using only their latency. The second issue involves the use of DMD to identify multiple modes contained in a single flow facet. The time-dependent coefficients of the dynamic modes are complex functions. Even in noisy experimental data, we find that the phase of these coefficients (but not their magnitude) exhibits repeatable dynamics. The phase represents the angular position of a rotating ring of cells and quantifies the downstream displacement of the vortices in reacting flows. Whether two dynamic modes should be assigned to a single flow constituent can be determined using Lassojous figures. A flow constituent can be reconstructed when all modes all DMD modes associated with it are identified.

We outline proper orthogonal and dynamic mode decompositions in Section 6.2. Section 6.3 introduces a state of two co-rotating rings of cells on a combustion front and reports on results from POD and DMD. We find that either decomposition can be used to partition the dynamics to those of the outer and inner rings of cells. POD and DMD are compared and contrasted using this example. We also introduce the algorithm to capture noise and other non-reproducible facets of the flow. In Section 6.4 these ideas are used to analyze vortex shedding behind a symmetric bluff body. We consider two types of flows. In the first, symmetric vortex pairs are shed periodically from either side of the bluff body. The second includes von Karman vortices as well. We conduct POD and DMD on both classes of flows. In particular, DMD is used to differentiate between major flow components from noise and other

non-reproducible aspects of turbulent combustion. It is also used to select modes with similar phase dynamics. Finally, in Section 6.5 we discuss the implications of our results. The Appendix section 6.6 shows conditions under which combinations of dynamic modes can be proper orthogonal modes.

6.2 Dynamic Mode and Proper Orthogonal Decompositions

We briefly outline dynamic mode and proper orthogonal decompositions and the associated computations from a spatio-temporal field. They are included for completeness and follow Refs. [29, 30, 31, 32, 26, 34, 33]. Suppose the state of a system is $\mathbf{z}$ and its dynamics is given by

$$\dot{\mathbf{z}} = \mathcal{F}(\mathbf{z}), \tag{6.1}$$

with an appropriate set of boundary conditions. The dynamics evolves the initial state $\mathbf{z}_0$ of the system to $\mathbf{S}^t(\mathbf{z}_0)$ at time t. In the case of reacting flows, $\mathcal{F}$ consists of the relevant reaction-diffusion and Navier-Stokes equations with, perhaps, no slip boundary conditions. For reacting flows, these equations, the associated model parameters, and boundary conditions are not known with sufficient accuracy to make reliable predictions. On the other hand, one has available, high-frequency, high-resolution data on various secondary fields associated with the flow; e.g., the temperature field through *planar laser-induced florescence* (PLIF) or velocity field through *particle image velocimetry* (PIV). Let us represent one such (observable)

secondary field (associated with $\mathbf{z}$) by $u[\mathbf{z}](\mathbf{x})$, where $\mathbf{x}$ are the grid points on which the observations are made. As the state of the system evolves from $\mathbf{z}_0$ at time $t = 0$ to $\mathbf{S}^t(\mathbf{z}_0)$ at time t, the secondary field evolves from $u[\mathbf{z}_0](\mathbf{x})$ to $u\left[\mathbf{S}^t(\mathbf{z}_0)\right](\mathbf{x})$. When the context is clear, we will simplify the notation by writing $u(\mathbf{x}, t)$ for $u[\mathbf{z}](\mathbf{x})$.

6.2.1 Proper Orthogonal Decomposition

In POD, $u(\mathbf{x}, t)$ is decomposed in a basis $\{\Psi_k(\mathbf{x})\}$ whose members are the normalized eigenvectors of the correlation matrix $\mathbf{C}$ given by $C_{\mathbf{x},\mathbf{x}'} \equiv \langle u(\mathbf{x}, t)u(\mathbf{x}', t)\rangle_t$, where $\mathbf{x}$ and $\mathbf{x}'$ are two spatial locations and the average is over time. Since $\mathbf{C}$ is real and symmetric, coherent structures $\{\Psi_k(\mathbf{x})\}$ are real and orthogonal; we will assume that they have been normalized. $\Psi_0(\mathbf{x})$ is the time-averaged field. For fields in two spatial dimension, denote the number of pixels in the two directions by H and W. The spatio-temporal field can be expanded as

$$u(\mathbf{x}, t) = \sum_{k=0}^{HW-1} b_k(t)\Psi_k(\mathbf{x}), \tag{6.2}$$

where $b_k(t)$ are the time-dependent coefficients.

Variations in $u(\mathbf{x}, t)$ can be quantified using $V \equiv \mathbb{E}\left[(u(\mathbf{x}, t))^2\right]$, where the expectation is over the spatial points and snapshots. Using the expansion of $u(\mathbf{x}, t)$ and the orthonormality of $\Psi_k(\mathbf{x})$'s, it is seen that $V = \sum\langle|b_k(t)|^2\rangle_t$. $L_k \equiv \langle|b_k(t)|^2\rangle_t$ can be interpreted as the contribution of the k^{th} mode to the dynamics; it is referred to as the latency (or "energy"). The expansion is assumed to be in a non-increasing order of L_k. Generally, it is assumed that high latency modes are robust and the remainder represents noise and other irregular facets of the flow. A reduced-order

approximation [35] for the flow can be derived by truncating the series (6.2) at an appropriate order n ($< HW$) to obtain $u_n(\mathbf{x}, t) \equiv \sum_{k=0}^{n-1} b_k(t)\Psi_k(\mathbf{x})$. The"quality" of the approximation is given by

$$\beta_n = \frac{\sum_{k=0}^{n-1} L_k}{\sum_{k=0}^{HW-1} L_k}. \tag{6.3}$$

Larger values of β_n correspond to better approximations of the data. Coherent structures are the most efficient basis in the sense that, for given n no other decomposition of the form $\sum_{k=0}^{n-1} \tilde{b}_k(t)\tilde{\Psi}_k(\mathbf{x})$ has a larger value of β_n [29, 30, 31, 32].

6.2.2 Dynamic Mode Decomposition

For a fixed time t, the Koopman operator is the linear operator U^t defined as [26, 34]

$$U^t\left(u(\mathbf{x}, t=0)\right) = u\left(\mathbf{x}, t\right). \tag{6.4}$$

Thus, U^t describes how the secondary field at time $t = 0$ transforms to that at time t. It is assumed to depend on $\mathcal{F}$ and the time interval, but not on the initial time. Unlike $\mathcal{F}$, which can be a nonlinear system, U^t is a HW-dimensional linear operator [34]. Interestingly, under very general conditions, the spectrum of $\mathcal{F}$ is contained in the spectrum of U^t [26, 34]; hence the stability and structure of solutions $\mathbf{z}(t)$ of the system $\mathcal{F}$ can be inferred through the analysis of the Koopman operator.

Dynamic mode decomposition [36, 33, 25] is an efficient algorithm to compute approximations for the eigenvalues and eigenvectors of U^t from experimental snapshots collected at uniform time intervals δt. Since $U^{\delta t}$ is independent of the state $u(\mathbf{x}, t)$, one can represent the transformation of the field during the time interval $[t, t + \delta t]$

as

$$u\left(\mathbf{x}, t+\delta t\right) = \mathbf{A} u\left(\mathbf{x}, t\right), \tag{6.5}$$

where $\mathbf{A} = \mathbf{A}(\delta t)$ is a matrix of size $HW \times HW$. Denoting by u_n the field corresponding to the snapshot taken at time $t = n\delta t$, Eqn. (6.5) can be re-written as $u_{n+1} = \mathbf{A} u_n$. Thus,

$$\mathbb{U}_1 \equiv \left[u_1, u_2, \ldots, u_{n+1}\right] = \mathbf{A}\left[u_0, u_1, u_2, \ldots, u_n\right] \equiv \mathbf{A}\mathbb{U}_0. \tag{6.6}$$

Finally, we note that for sufficiently large n (certainly for n larger than the number of pixels in each snapshot), u_{n+1} is linearly dependent on all the previous u_k's; write $u_{n+1} = \sum_{k=1}^{n} c_k u_k$. Thus, we can write $\mathbb{U}_1 = \mathbb{U}_0\mathbf{B}$, where the *companion matrix* is [36, 33, 25, 26]

$$\mathbf{B} = \begin{pmatrix} 0 & 0 & \ldots & 0 & c_0 \\ 1 & 0 & \ldots & 0 & c_1 \\ 0 & 1 & \ldots & 0 & c_2 \\ \ldots & \ldots & \ldots & \ldots & \ldots \\ 0 & 0 & \ldots & 1 & c_n \end{pmatrix}. \tag{6.7}$$

Since $\mathbf{A}\mathbb{U}_0 = \mathbb{U}_0\mathbf{B}$, the spectra of $\mathbf{A}$ and $\mathbf{B}$ are identical. Even in cases where the expansion of u_{n+1} can only be approximated by a linear combination of u_k's, eigenvalues of $\mathbf{B}$ are approximations to those of $\mathbf{A}$ [36, 33, 26]. The spectrum of $\mathbf{B}$ can be computed using the (fast) Arnoldi method [37, 36]. Eigenfunctions of $\mathbf{A}$ are referred to as *dynamic modes* of the flow [36, 33, 25]. Dynamic mode decomposition provides a subset of the Koopman spectrum Λ_n and the corresponding eigenfunctions $\Phi_n(\mathbf{x})$. Koopman eigenfunctions evolve as $\exp(\Lambda_n t)$ under $\mathcal{F}$; they are the generalization of normal modes.

It should be noted that, since $\mathbf{A}$ is not symmetric, the eigenvalues Λ_n and the eigenfunctions $\Phi_n(\mathbf{x})$ are, in general, complex valued. Furthermore, the eigenfunctions are not orthonormal. Eigenvalues of the Hermitian conjugate $\mathbf{A}^\dagger$ of $\mathbf{A}$ are $\Lambda_n^* t$. The corresponding eigenfunctions $\tilde{\Phi}_n(\mathbf{x})$ are orthogonal to $\Phi_n(\mathbf{x})$'s; specifically, with an appropriate normalization $\int d\mathbf{x}\ \tilde{\Phi}_m(\mathbf{x})\Phi_n(\mathbf{x}) = \delta_{mn}$. Note that unlike POD, which uses second order statistics, dynamic modes are computed using first-order statistics. Hence one may expect consequences of noise and other irregular features to be less significant in DMD.

The spatio-temporal field $u(\mathbf{x}, t)$ can be expanded as

$$u(\mathbf{x}, t) = \sum_{DMD} a_n(t)\Phi_n(\mathbf{x}), \tag{6.8}$$

where, $\sum_{DMD}$ represents the sum over the DMD modes. By the orthonormality introduced above, $a_n(t) = \int d\mathbf{x}\ \tilde{\Phi}_n(\mathbf{x})u(\mathbf{x}, t)$. If necessary, the field can also be expanded in the basis $\{\tilde{\Phi}(\mathbf{x})\}$ as $u(\mathbf{x}, t) = \sum \tilde{a}_n(t)\tilde{\Phi}_n(\mathbf{x})$. Now the variations in the spatio-temporal dynamics reduces to $V = \sum a_n \tilde{a}_n$ and we can interpret the quantity $L_n = a_n\tilde{a}_n$ as the latency associated with the n^{th} mode. (Note however that L_n is not positive definite; hence, in defining β_n –Eqn. (6.3) – we need to take the sum of absolute values.)

Unlike proper orthogonal decomposition, dynamic modes are associated with unique eigenvalues Λ_n. We can use this observation to address an important issue. A flow constituent (e.g., von Karman vortices) is not captured by a single coherent structure or dynamic mode; rather several such modes are required to reconstruct a typical constituent [28]. In POD, there is no method to identify and assign modes

associated with a specific flow constituent. In contrast, analysis of simulated and experimental data suggests that the dynamic modes associated with a flow constituent can be identified. Specifically, such eigenvalues are found to lie on a smooth curve in the complex plane [36, 33, 25]. An alternative scheme is as follows: recall that the primary dynamic mode (i.e., that with the highest latency) has a single frequency, the imaginary part of the corresponding Λ. One may expect dynamic modes with harmonics of this frequency to be associated with the same flow constituent. In the next Section, these ideas are used to decompose real flows.

DMD modes associated with reproducible features of a flow will be "robust;" i.e., they will be found in multiple realizations of an experiment. In contrast, modes representing non-reproducible flow characteristics will change with the realization. The observation leads to the following conjecture: *it is possible to differentiate reproducible and non-reproducible aspects of a flow by comparing DMD spectra from multiple realizations of a set of nominally identical experiments.* As argued in the examples below, a similar differentiation of reproducible and non-reproducible modes cannot be made using POD. Finally, we observe that in constructing reduced order models, we can discard the non-reproducible features, and only retain their statistical characteristics; in other words, we only need to consider the primary, robust flow constituents in reduced order models.

6.3 Cellular Flame Patterns

6.3.1 The Experiment

The experiment was conducted in the laboratory of our late colleague, Professor Michael Gorman [5, 38, 27]. Cellular flame patterns were generated on a circular porous-plug burner mounted in a combustion chamber maintained at a pressure 0.3-0.5 atm. A mixture of methane and air enters a porous medium and following passage through it forms a flat flame front. It is a luminous disk 5.62 cm in diameter and approximately 0.5 mm thick. The ambient pressure, fuel/oxidizer ratio, and the flow rate are controlled to within 1%. A dage-MTI charge-coupled device camera is mounted vertically on top of the combustion chamber to record the spatio-temporal patterns.

As the flow rate is increased, the circular flame front experiences local curvature, resulting in symmetry-broken cellular structures. The cellular pattern consists of brighter (hotter) cells demarked by darker (cooler) cusps that extend further away from the porous plug. The motion is video-recorded at 30 Hz. The spatio-temporal dynamics was captured by $N = 123$ equally spaced snapshots with a resolution of $W = 216$ pixels along the length and $H = 190$ pixels along the height of a snapshot. Both POD and DMD were implemented on a matrix of $W \times H$ columns (spatial points in a snapshot) and N rows (number of snapshots).

6.3.2 The Double Rotating State

We analyze a cellular flame pattern of two co-rotating rings of cells, several consecutive snapshots of which are shown in Figure 6.1. The inner ring of two cells and the outer ring of six cells rotate clockwise, although at different rates. States where the rings rotate in opposite directions and those with rings containing different numbers of cells were also observed [5]. The analysis outlined below has been applied to these patterns as well.

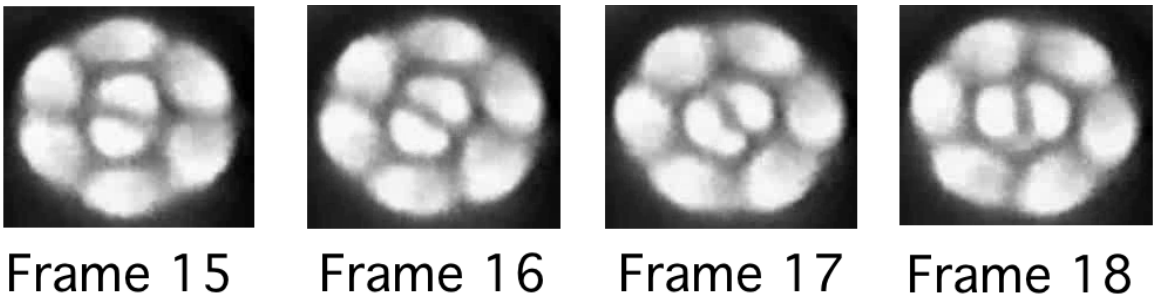

Figure 6.1: Several consecutive snapshots from the cellular flame state of two co-rotating rings of cells. Note that the angular speeds of the two rings are different.

6.3.3 Proper Orthogonal Decomposition

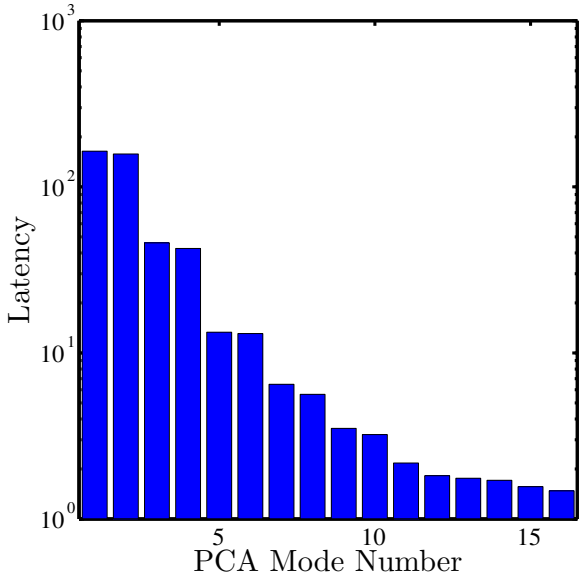

Figure 6.2: Latencies of the first 16 proper orthogonal modes of the double co-rotating state.

Figure 6.2 shows the latencies of the first sixteen proper orthogonal modes of the co-rotating cellular state, and Figures 6.3 and 6.4 show the first four proper orthogonal modes and the power spectra of (the real part of) their time-dependent coefficients. The first two modes have a six-fold symmetry and represent the outer ring while the next two modes have a two-fold symmetry and located near the inner ring. The next two modes (not shown), once again, are located near the outer ring and have a twelve-fold symmetry. The fourth pair is located in the region of the inner ring and has a four-fold symmetry. In fact, the motion of a ring of k cells require the presence of modes of k and $2k$-fold symmetries as discussed in Refs. [39, 40]. As seen

from panels (c) and (d) of Figures 6.3 and 6.4, the dynamics, $b_n(t)$, for these modes contain a narrow range of spectral components.

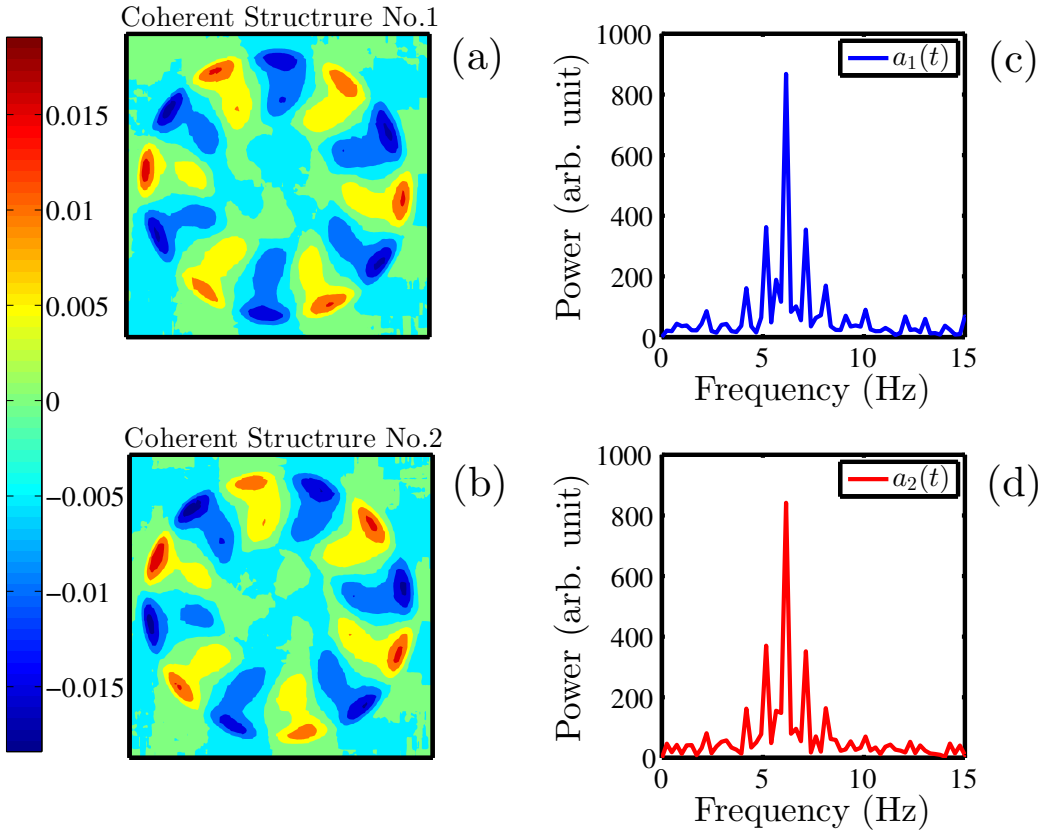

Figure 6.3: Coherent structures (a) $\Psi_1(\mathbf{x})$ and (b) $\Psi_2(\mathbf{x})$ and the power spectra (of the real part) of their time-dependent coefficients (c) $b_1(t)$ and (d) $b_2(t)$. Observe that the modes are located close to the outer ring of cells. Power spectra in (c) and (d) have several significant Fourier components.

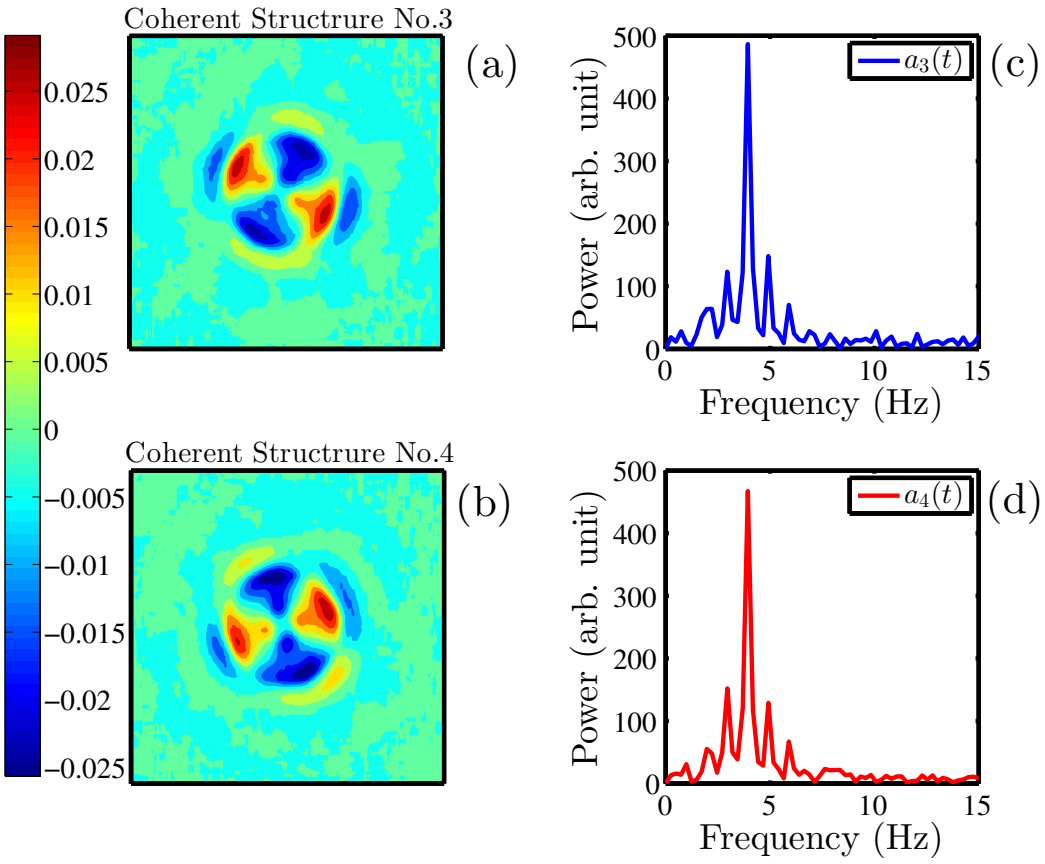

Figure 6.4: Coherent structures (a) $\Psi_3(\mathbf{x})$ and (b) $\Psi_4(\mathbf{x})$ and the power spectra (of the real part) of their time-dependent coefficients (c) $b_3(t)$ and (d) $b_4(t)$. Modes are located near the inner ring of cells. Power spectra in (c) and (d) have several significant Fourier components.

As seen from Figure 6.2, the first 8 modes (in addition to $\Phi_0(\mathbf{x})$) capture a significant fraction of the total latency of the spatio-temporal dynamics. The latencies of the remaining modes decay very slowly, and one may suspect that they represent

noise and non-reproducible facets of the flame dynamics. The spatio-temporal dynamics of the *reproduction* (i.e., the reduced-order dynamics) using the first $n = 9$ coherent structures is

$$u_9(\mathbf{x}, t) = \sum_{k=0}^{8} b_k(t)\Psi_k(\mathbf{x}). \tag{6.9}$$

Figure 6.5 shows several snapshots of the approximation, and should be compared with Figure 6.1. The differences between the two sets of snapshots is small. The spatio-temporal dynamics of the inner and outer rings can be extracted using reproductions that include modes $\{1, 2, 5, 6\}$ and $\{3, 4, 7, 8\}$ respectively, as also shown in Figure 6.5.

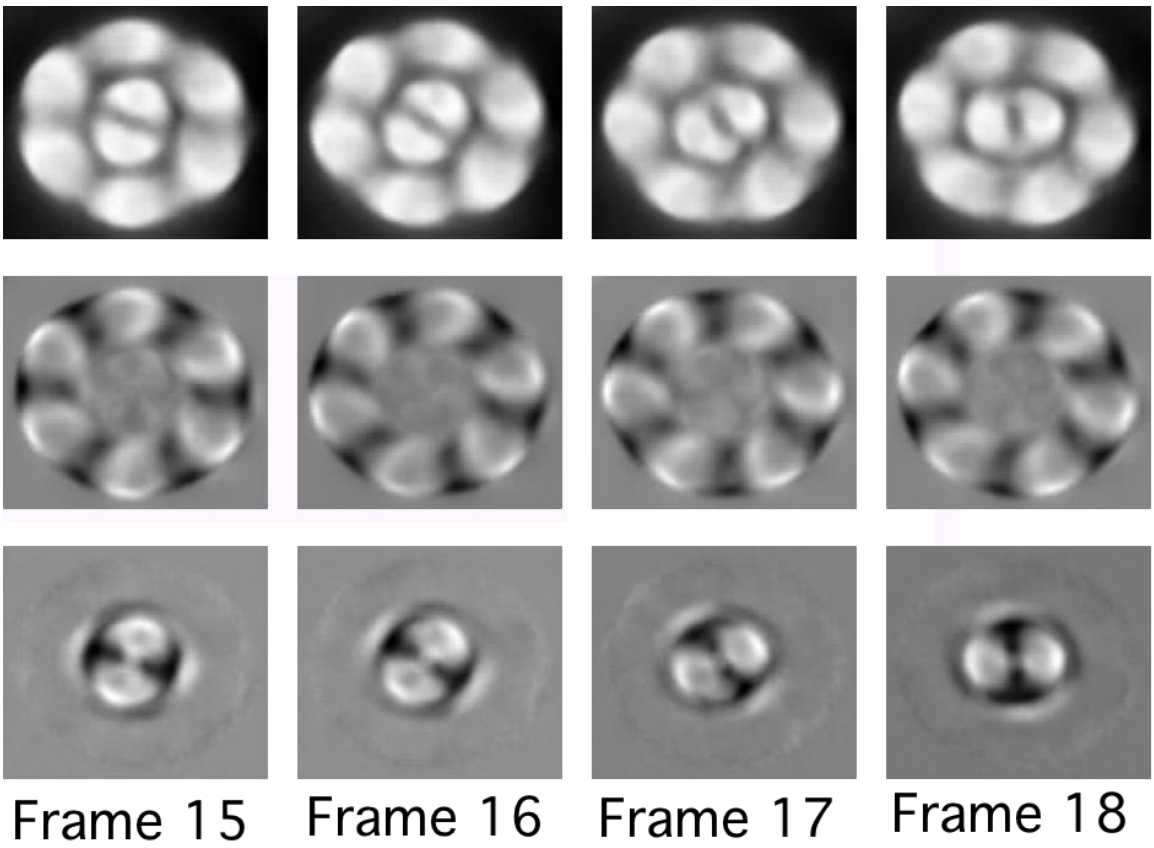

Figure 6.5: Reproductions of the snapshots corresponding to those shown in Figure 6.1 are shown in the top row. The second and third rows show the reproductions of the outer and inner rings of cells.

Although the spatio-temporal dynamics $u_9(\mathbf{x}, t)$ is close to $u(\mathbf{x}, t)$, we cannot determine the roles played by the remaining coherent structures (noise, finer features of the flow, etc.). Notice also that our selection of coherent structures 1, 2, 5, and 6 as belonging to a single dynamical constituent was based only on their symmetries. It is not clear how a flow constituent can be recreated in more general configurations.

6.3.4 Dynamic Mode Decomposition

Figure 6.6(a) shows the (complex) eigenvalues of the dynamic modes for the double co-rotating state with the highest 70 latencies. They appear in complex conjugate pairs and we only show those with non-negative imaginary parts. Next, we subdivide the series of snapshots into several subgroups, for example the first half, the second half, the middle half, etc. We recompute DMD spectra for each of these subgroups and search for the modes that are "robust"; i.e., those that are common to all subgroups. These robust modes, along with the mode numbers ordered in non-decreasing order of their latencies, are shown in Figure 6.6(b). The latencies of the modes are color coded (online version) according to the color bar shown to the right.

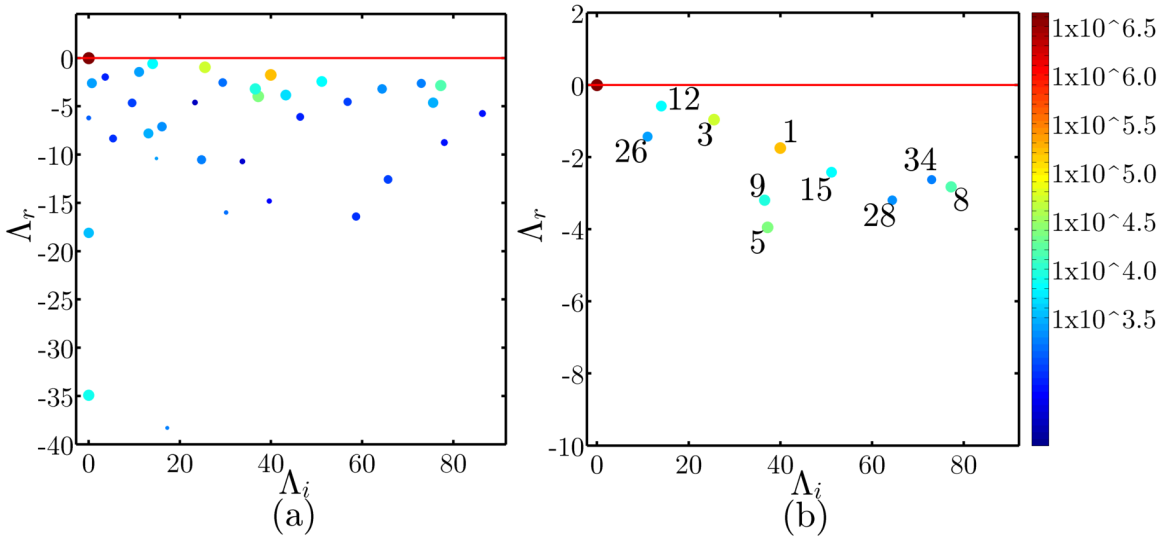

Figure 6.6: (a) Koopman eigenmodes of the double co-rotating state with the 70 largest latencies. They arise in complex conjugate pairs and only those with positive real parts are shown. (b) Robust modes which remain unchanged -or nearly unchanged- between several sub-intervals of the dynamics. They are assumed to represent the reproducible features of the flow.

Figure 6.7 shows the latencies of the dominant modes. We observe that, although most robust modes have high latencies, it is not possible to partition robust and non-robust modes using latency alone. Our conjecture is that those robust modes represent reproducible facets of the combustion flow; conversely, modes that are not robust are associated with the non-reproducible features including noise.

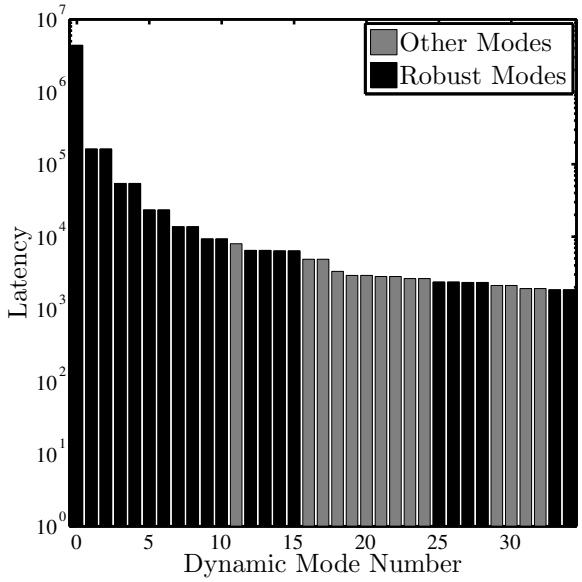

Figure 6.7: Latencies of the 35 dynamic modes with the largest latencies. The robust modes are shown in black.

Figure 6.8 shows the real and imaginary parts of the (complex) DMD mode $\Phi_1(\mathbf{x})$ with the highest latency; its eigenvalue is $\Lambda_1 = -1.75 + 39.96i$. The frequency associated with this mode is $\Omega_1 = Im(\Lambda_1)/2\pi \approx 6.4(frame\ rate)$. The mode is located on the outer ring of cells and has the same six-fold symmetry. Although this Koopman mode has a frequency Ω_1, nonlinear coupling to other modes impose additional frequency content to $\hat{a}_1(\omega)$.

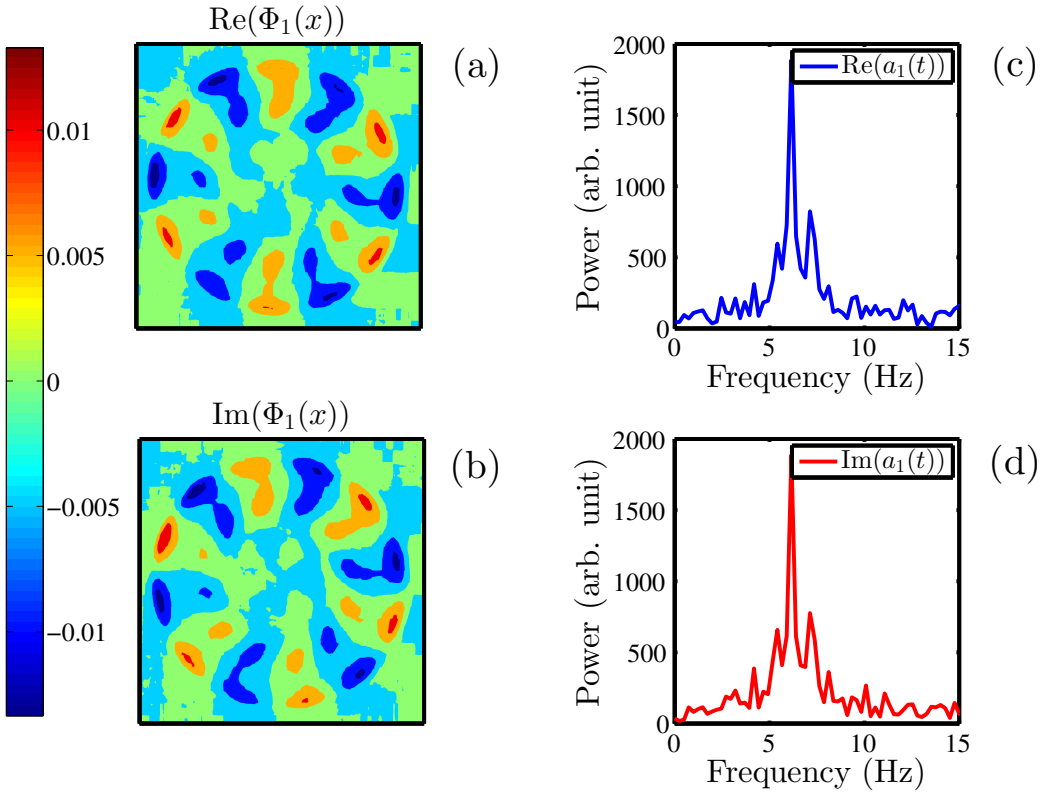

Figure 6.8: (a) Real and (b) imaginary parts of the dynamic mode of the double co-rotation state with the highest latency. The dynamics of the (c) real and (d) imaginary parts of $a_1(t)$ are dominated by the frequency Ω_1.

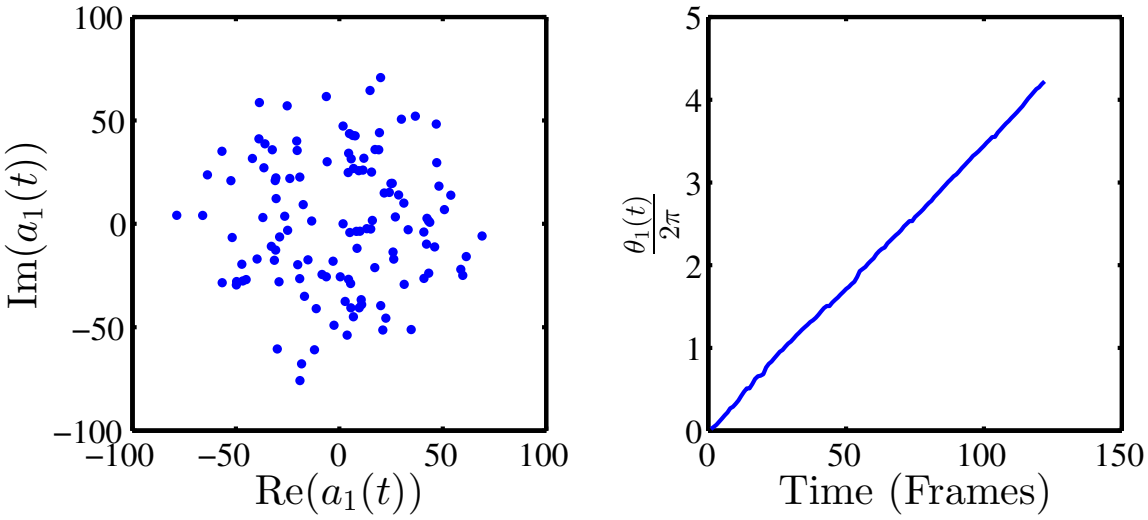

Figure 6.9: (a) The points $a_1(t)$ in the complex plane are broadly distributed. However, the behavior of the phase angle, defined as $\theta_1(t) = tan^{-1}\left(Im(a_1(t)/Re(a_1(t))\right)/s(1)$, where $s(1)$ is the symmetry of the mode, evolves smoothly. The slope $\omega_1(t)$ of the curve is the angular velocity of the ring.

The scattered plot of the real and imaginary parts of $a_1(t)$ is shown in Figure 6.9(a). The fluctuations may reflect experimental noise or irregularities in the flow. Interestingly, we find that the angular changes of the phase space orbit are highly regular and the irregularities are restricted to the radial component. In order to illustrate this point we define

$$\theta_1(t) = tan^{-1}\left(Im(a_1(t)/Re(a_1(t))\right)/s(1), \tag{6.10}$$

where $s(1)$ denotes the spatial symmetry of $\Phi_1(\mathbf{x})$; specifically $\Phi_1(\mathbf{x})$ belongs to the dihedral group $D(s(1))$. Thus, $s(1) = 2$ for the inner ring and $s(1) = 6$ for the outer ring. The role of $s(1)$ in the definition is justified from the following

observation: when a ring of cells rotates by $2\pi/s(1)$, the pattern is repeated, and $tan^{-1}\left(Im(a_1(t)/Re(a_1(t))\right)$ has changed by 2π.

As seen from Figure 6.9(b), the evolution of $\theta_1(t)$ is highly regular; its slope $\omega_1 \equiv \partial\theta_1/\partial t$ is the angular velocity of the ring of cells. We will henceforth use $\theta(t)$ and $\omega(t)$ to characterize the evolution of each dynamic mode. We also note that, since the POD modes are real, no such angular behavior can be defined in general. (Angular behavior of pairs of POD modes can be computed in special cases, see Ref. [27].)

Figure 6.10 shows the real and imaginary parts of the dynamic mode with the next highest latency, $\Phi_3(\mathbf{x})$, the power spectrum of $a_3(t)$, and the phase dynamics $\theta_3(t)$. (Note that $\Phi_2(\mathbf{x}) = \Phi_1^*(\mathbf{x})$ has the same latency as $\Phi_1(\mathbf{x})$. Similarly $\Phi_3(\mathbf{x})$ and $\Phi_4(\mathbf{x})$ have the same latency.) $\Phi_3(\mathbf{x})$ represents the inner ring and $\omega_3(t)$ its angular velocity. Once again, we note that the power spectrum has a smaller spectral range than that of the corresponding POD modes $\Psi_3(\mathbf{x})$ and $\Psi_4(\mathbf{x})$ and that the angular velocity of the inner ring is highly regular.

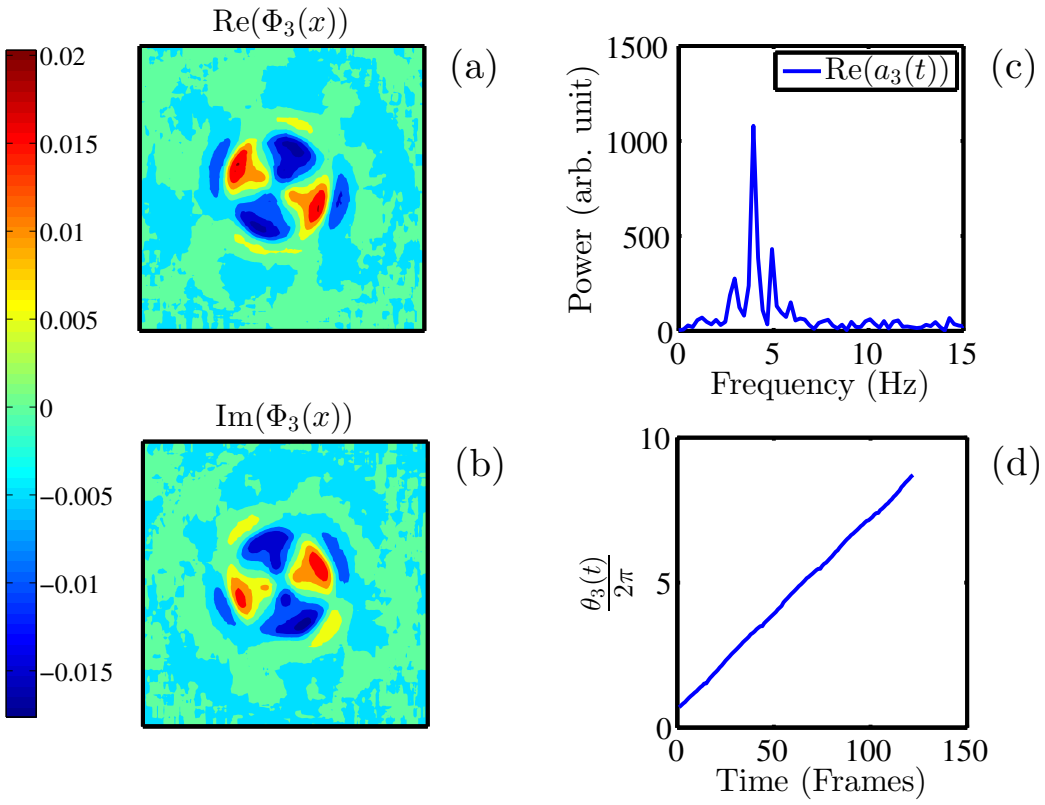

Figure 6.10: (a) Real and (b) imaginary parts of the dynamic mode of the double co-rotation state with the second highest latency. The dynamics of the (c) real part of $a_3(t)$ are dominated by one frequency. (d) The phase of $a_3(t)$ evolves smoothly.

The spectrum of the dynamics of the DMD mode $\Phi_1(\mathbf{x})$ is different from those of the dynamics of the corresponding POD modes $\Psi_1(\mathbf{x})$ and $\Psi_2(\mathbf{x})$. Let us explain this observation. $\Phi_9(\mathbf{x})$ has a spatial structure that is a rotation of $\Phi_1(\mathbf{x})$; it is located in the outer ring and has the same 6-fold symmetry. However, the eigenvalues Λ_1 and Λ_9 and the primary spectral components of $\hat{a}_1(\omega)$ and $\hat{a}_9(\omega)$ are different. In general, there can be multiple DMD modes with identical or symmetry-related spatial

structure but with different eigenvalues. In POD such modes are combined into a single mode or a pair of modes, such as $\Psi_1(\mathbf{x})$ and $\Psi_2(\mathbf{x})$. $\hat{b}_1(\omega)$ is the sum of the $\hat{a}(\omega)$'s for the associated dynamic modes. This is the sense in which the POD expansion is more efficient while DMD provides more refined dynamical details of a mode. For example, if the two modes $\Phi_1(\mathbf{x})$ and $\Phi_9(\mathbf{x})$ belonged to different flow constituents, POD will fail to make the proper assignments of modes.

Finally, the relationships between different dynamic modes can be illustrated using a Lassajous figures, such as those shown in Figure 6.11. It is a helpful presentation of mode dynamics that may aid in identifying strongly coupled modes. For example, the dynamics of $a_3(t)$ appears to be uncorrelated with the dynamics of $a_1(t)$ and strongly correlated with that of $a_{15}(t)$. The information is helpful in developing a low-order model for the flow.

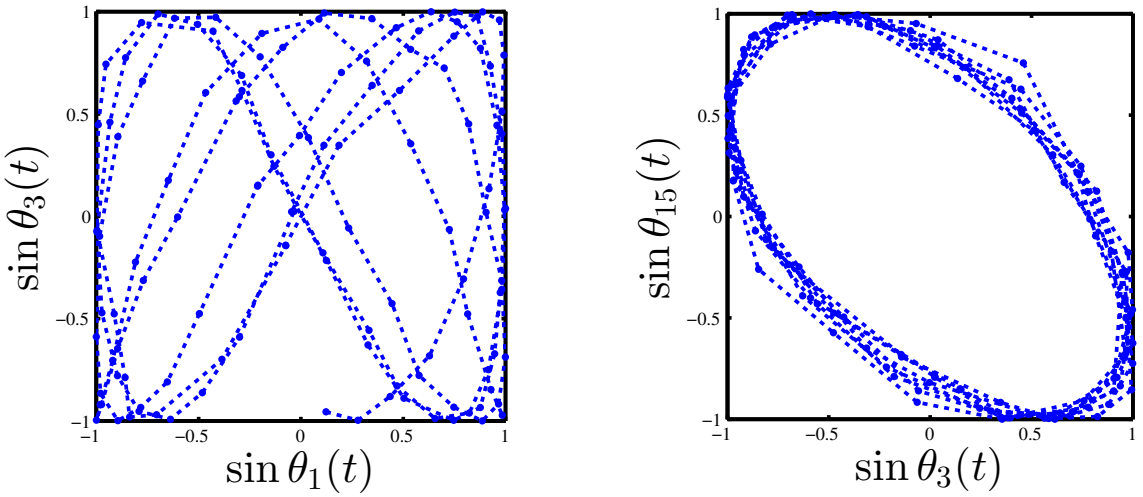

Figure 6.11: (a) Plot of $\theta_1(t)$ vs. θ_3 shows modes $\Phi_1(\mathbf{x})$ and $\Phi_3(\mathbf{x})$ likely exhibit independent dynamics. (b) In contrast, modes $\Phi_3(\mathbf{x})$ and $\Phi_{15}(\mathbf{x})$ appear to be strongly coupled, suggesting that they belong to a single flow constituent.

We highlight two significant advantages of dynamic mode decomposition. First, the DMD spectrum from multiple, nominally identical experiments can be used to differentiate between robust and non-robust aspects of a flow. Since a corresponding partition cannot be based on latency alone, POD cannot be used for the purpose. Second, the dynamics of the phase defined in Eqn. (6.10), unlike the corresponding magnitude, exhibits very little noise. Hence their phase dynamics, through Lassajous figures, can be used to search for modes that belong to the same flow constituent. An analogous phase cannot be defined in POD. These aspects of DMD are critical in developing effective low order models of the flow.

6.4 Reacting Flows behind a Bluff Body

In this Section, we use proper orthogonal and dynamic mode decompositions to analyze reacting flows behind symmetric bluff bodies. There are two classes of vortex shedding. The first involves periodic shedding of symmetric pairs of vortices from either side of the bluff body. The second is von Karman shedding, where a single vortex shed from one side of the bluff body is followed by a another shed from the opposite side [10, 11]. The von Karman shedding is periodic as well. Study of the onset and growth of vortex shedding behind bluff bodies is partly motivated by the changes in vortex dynamics as the equivalence ratio is changed from rich to lean conditions [13]. Their development needs to be constrained for controlling combustion instabilities related to various bluff body combustors [6, 41].

6.4.1 The Experiment

Experiments on reacting flows were conducted within an optically accessible, atmospheric-pressure combustion test section that contains a bluff-body flame holder for flame stabilization. Air is delivered into a 152-mm $\times$ 127-mm rectangular test section at a constant rate of 0.32 kg/s. While the air rate is maintained constant, propane fuel is added and mixed upstream of the flame holder to provide equivalence ratios (i.e., the fuel-to-oxidizer ratio and the corresponding stoichiometric value) that vary between $\phi = 0.6$ and 1.1. The flame holder is a v-gutter with a width of 38.1 mm and an angle of 35^o, which is capable of holding the flame to a blow-off equivalence ratio of $\phi = 0.55$. Additional facility details and detailed flame-holder dimensions

are provided in Ref. [13].

The bluff-body is symmetric under reflection about a line parallel to the flow, and symmetric vortex shedding [42, 43] is observed in the entire range of control parameters. As the equivalence ratio is reduced, the flows develop, in addition, the asymmetric von Karman vortices [13].

Two-dimensional images of hydroxyl (OH) behind the bluff-body V-gutter were acquired utilizing planar laser-induced fluorescence (PLIF) technique. The detailed description of the experimental setup could be found elsewhere [44]. Briefly, PLIF of OH was performed using a 10-kHz diode-pumped solid-state Nd:YAG and a tunable dye lasers. The 532 nm output of the Edgewave laser was used to pump the dye laser for obtaining tunable laser output at ∼586 nm. This wavelength is then frequency doubled at ∼283 nm to excite the $Q_1(9)$ rovibrational transition in the $A^2\Sigma+ \rightarrow X^2\Pi$ $(1,0)$ band of OH. The $Q_1(9)$ transition has a low Boltzmann fraction sensitivity between temperatures of 1000-2400K minimizing the need for a temperature correction on Boltzmann concentrations when extracting flame fronts. PLIF signal of OH was collected employing a LaVision dual-stage high-speed UV intensifier (IRO) coupled to a Photron SA-5 CMOS camera. The collected light was filtered using a Brightline Semrock filter with approximately 90% transmission between 300-340nm. The combination of spectral filtering and time-gating the intensifier allowed for maximum fluorescence collection while minimizing interference from flame emission and laser scatter.

Fluctuations in the recorded PLIF intensity contains a uniform gradient in the y-direction, as was verified by averaging several sets of snapshots. The effect can be

observed in the snapshots shown in Figure 6.12 and in the POD and DMD modes, which fail to be symmetric quantitatively.

6.4.2 Symmetric Vortex Shedding

In this Section we present the results from proper orthogonal and dynamic mode decompositions of reacting flows behind the v-gutter bluff body that exhibit only periodic shedding of symmetric pairs of vortices. The flow is observed for equivalence ratios between $\phi = 0.9$ and $\phi = 1.1$. Figure 6.12 shows several snapshots of the vortex shedding at $\phi = 1.1$ displaying a period of approximately 8 ms (80 frames). POD and DMD analyses were conducted on the last 4,000 of the 8,000 snapshots.

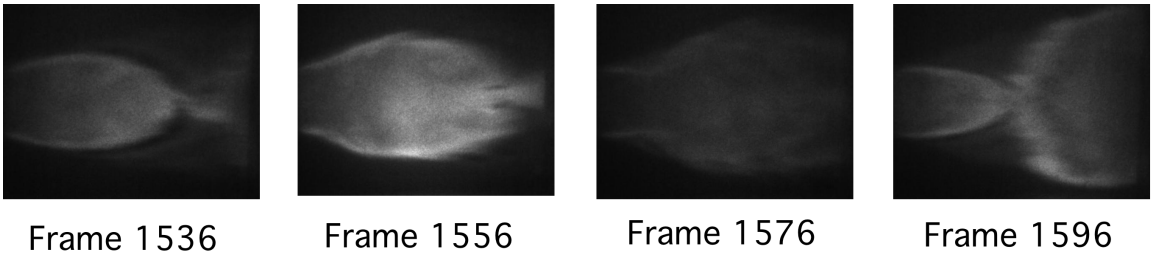

Figure 6.12: Four snapshots of the reacting flow at $\phi = 1.1$ exhibiting symmetric vortex shedding of approximate period 80 frames. Although the flow is expected to be symmetric, the PLIF images of these modes are not quantitatively symmetric due to a uniform gradient in the y-direction of the PLIF measurement.

6.4.2.1 Proper Orthogonal Decomposition

Figure 6.13 shows the first two proper orthogonal modes and the Fourier transforms of (the real part of) their coefficients. The modes contain a single high intensity patch (yellow/red) along the x-direction. These as well as all other relevant modes are (qualitatively) symmetric about a horizontal axis. However, as mentioned earlier, the PLIF intensity displays a uniform gradient in the y-direction, which is reflected in the quantitative asymmetry of the proper orthogonal modes. The time dependent coefficients of these modes exhibit a unique frequency 125 Hz.

The pair of POD modes with the next highest latencies are harmonics; specifically, they contain two sets of high intensity regions along the x-direction (compared to one in Figure 6.13) and the dominant spectral component of $\hat{b}_3(\omega)$ and $\hat{b}_4(\omega)$ are at a frequency 250 Hz. Modes that represent higher harmonics of $\Psi_1(\mathbf{x})$ and $\Psi_2(\mathbf{x})$ are found as well.

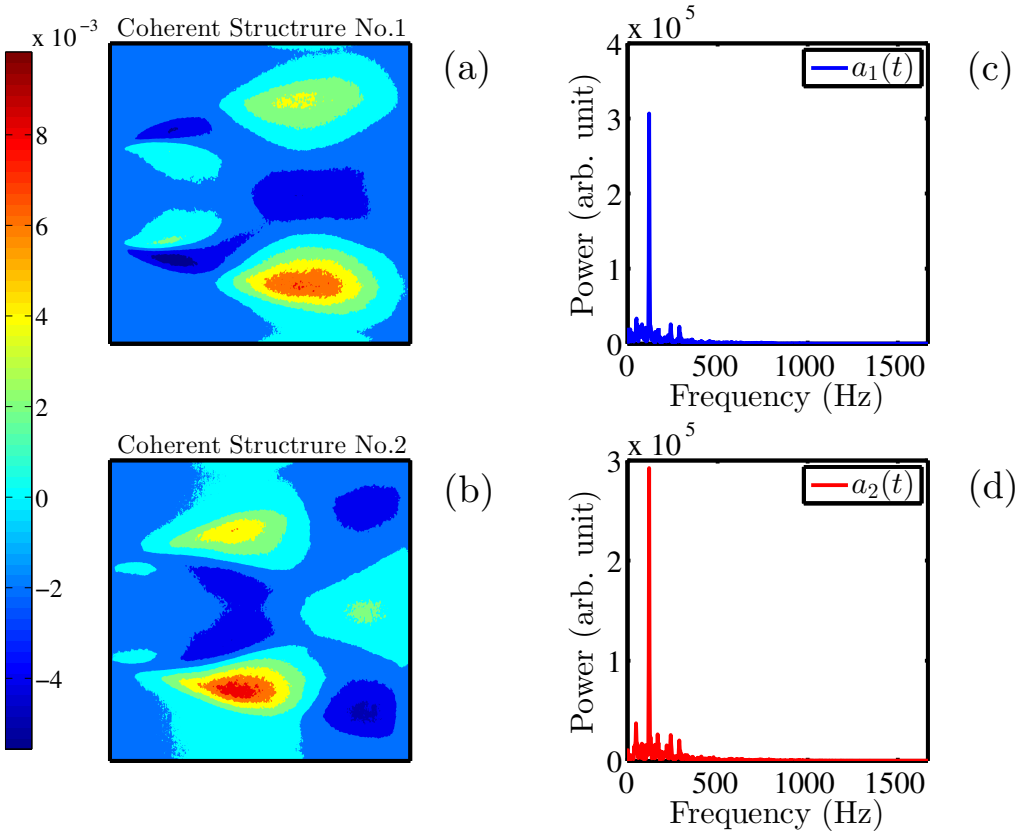

Figure 6.13: First (a) and the second (b) coherent structures for the reacting flow at equivalence ratio $\phi = 1.1$ where symmetric pairs of vortices are shed from the sides of the symmetric bluff body periodically. All primary coherent structures are nearly symmetric for this flow. The Fourier spectra of the time-dependent coefficients of these modes, shown in (c) and (d), exhibit a dominant frequency of 125 Hz.

6.4.2.2 Dynamic Mode Decomposition

Figure 6.14(a) shows the Koopman eigenvalues and Figure 6.14(b) the robust modes, which are identified using 2000-frame sections of the video. The mode numbers in Figure 6.14(b) are ordered according to their latencies shown in Figure 6.15. Once again we find that most, though not all, of the high latency modes are reproducible. This is another example to illustrate that latency does not partition robust and non-robust modes. (It should be noted that the figure shows only modes with positive imaginary parts, and not their complex conjugates with negative imaginary parts.)

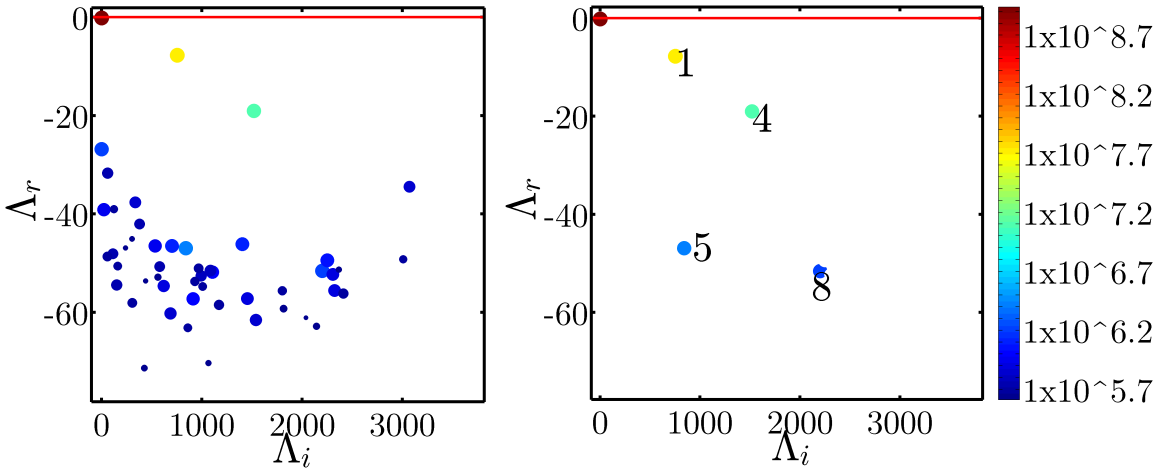

Figure 6.14: (a) The DMD spectrum for the reacting flow at equivalence ratio $\phi = 1.1$. (b) Koopman eigenvalues that are unchanged between subsections of the flow. The mode numbering is assigned according to the (non-increasing order of) latencies.

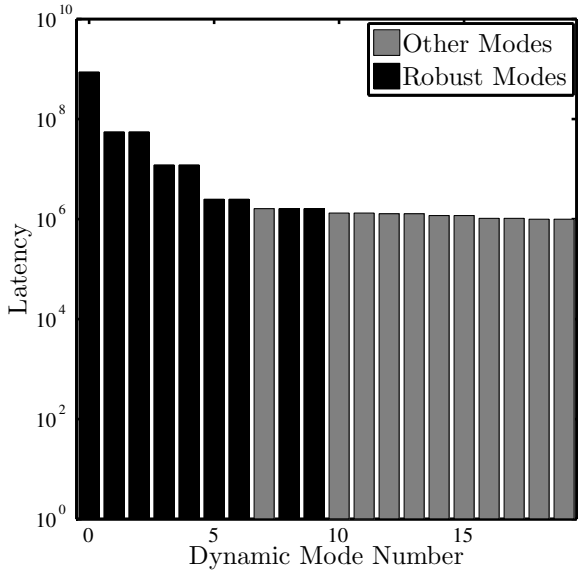

Figure 6.15: Latencies of the first 20 dynamic modes of the reacting flow at equivalence ratio $\phi = 1.1$. Robust modes are shown in black. Note that mode 7 is not reproducible.

Figures 6.16(a) and (b) show the real and imaginary parts of the dynamic mode $\Phi_1(\mathbf{x})$. Apart from the y-gradient in the PLIF field, the mode is symmetric about the x-axis. The coefficient of $\Phi_1(\mathbf{x})$, $a_1(t)$, has a dominant frequency of 125 Hz as seen from Figure 6.16(c). Furthermore, we notice that $\Phi_1(\mathbf{x})$ contains a single high intensity (yellow/red) region along the x-direction (in contrast to $\Phi_2(\mathbf{x})$, see below); we can define $s(1) = 1$, analogous to the symmetry of dynamic modes of the double rotating state. However, here the definition pertains to the number of "structures" in the flow direction. As in the last Section, we can define a "phase" associated with the mode by $\theta_1(t) = tan^{-1}\left(Im(a_1(t)/Re(a_1(t))\right)/s(1)$. It represents the displacement of the structure along the x-direction, rather than a spatial rotation

in the previous example. One can also define the rate of phase advancement by $\omega_1(t) = \partial\theta_1(t)/\partial t$. This will be the flow velocity of the corresponding constituent. Figure 6.16(d) shows that the evolution of $\theta_1(t)$ is highly regular in contrast to the noisy radial component $|a_1(t)|$. Thus even though there is a significant level of variation between successive vortices, the fluctuations are in the magnitude of the coefficient (similar to Figure 6.9(a)); the downstream flow velocity is highly regular.

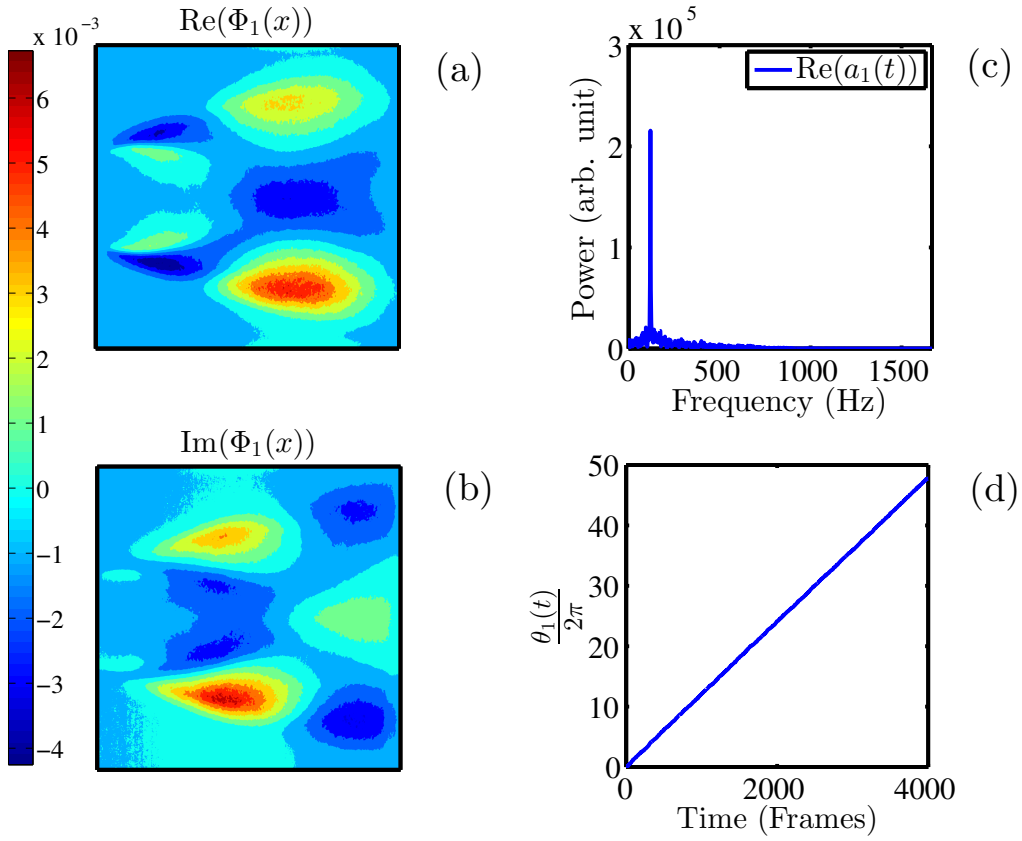

Figure 6.16: (a) Real and (b) imaginary parts of $\Phi_1(\mathbf{x})$ for the reacting flow at equivalence ratio $\phi = 1.1$. (c) The spectrum of $a_1(t)$ exhibits a dominant frequency at 125 Hz. (d) The phase advancement $\theta_1(t)$ exhibits a very regular growth.

Figure 6.17 shows the real and imaginary parts of $\Phi_4(\mathbf{x})$, one of the two dynamic modes with the next highest latency and the Fourier transform of the real part of $a_4(t)$. $\Phi_4(\mathbf{x})$ contains two distinct high intensity regions along the x-direction (those shown in yellow/red) and thus $s(4) = 2$. The phase has characteristics of a spatial harmonic of $\Phi_1(\mathbf{x})$ and the dominant frequency of $a_4(t)$ is 250 Hz. The dynamics of the phase $\theta_4(t)$, shown in Figure 6.17(d) is regular. The rate of phase advancement is identical to that of $\theta_1(t)$.

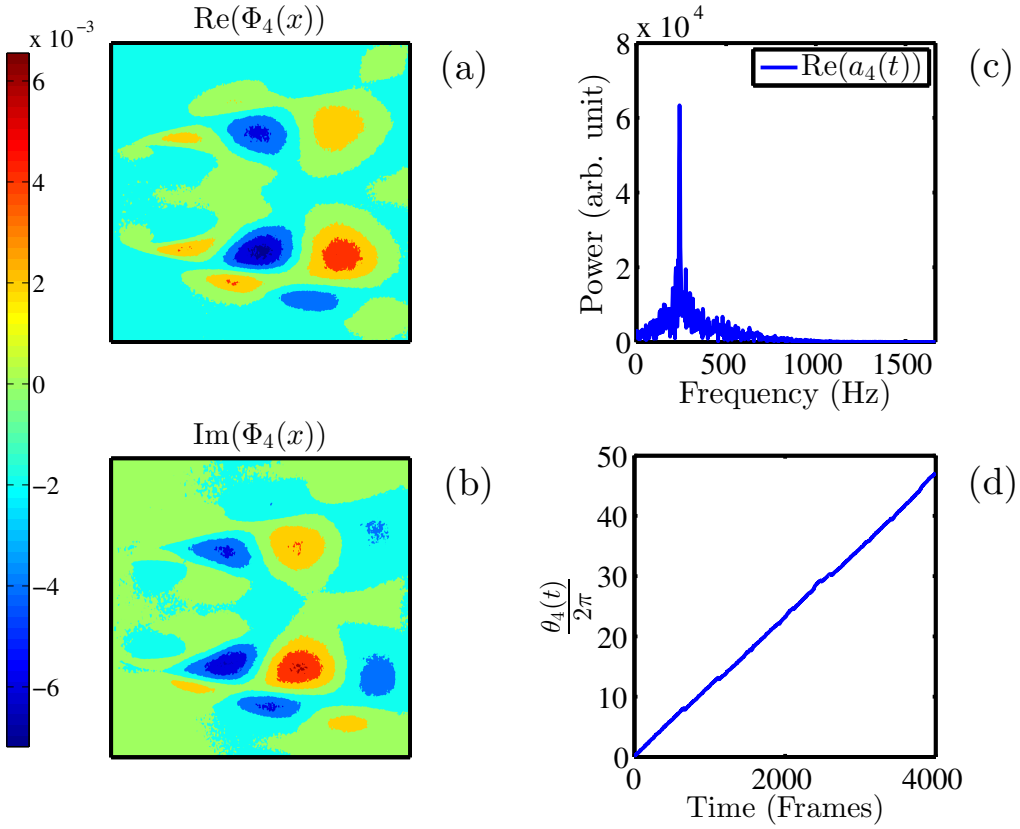

Figure 6.17: (a) Real and (b) imaginary parts of $\Phi_4(\mathbf{x})$ for the reacting flow at equivalence ratio $\phi = 1.1$. (c) $\hat{a}_4(\omega)$ peaks at 250 Hz. (d) $\theta_4(t)$ exhibits regular behavior and the rate of its growth is identical to that of $\theta_1(t)$.

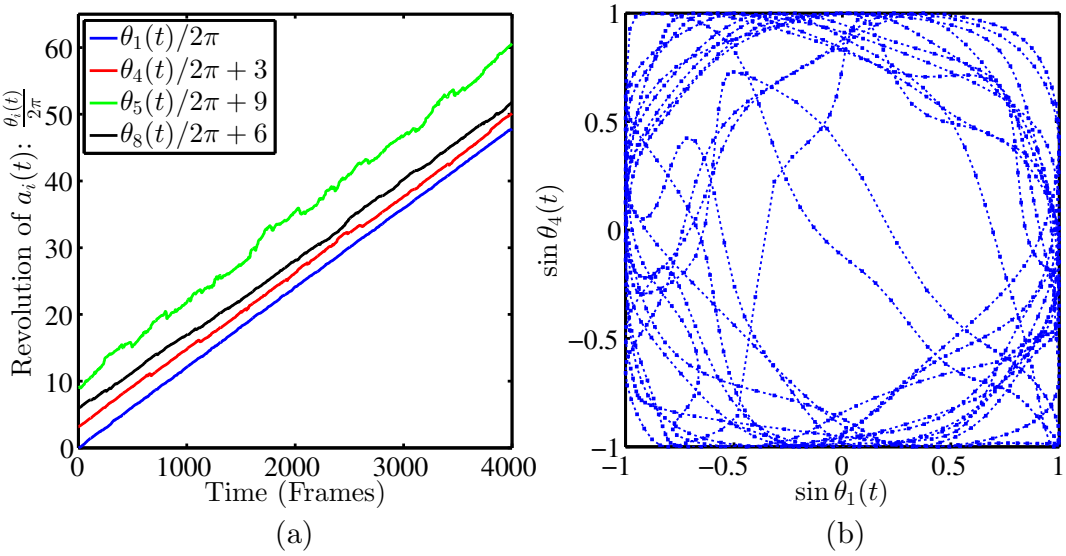

Figure 6.18: The rates of phase advancement of all robust modes for the reacting flow at $\phi = 1.1$ are nearly identical. Successive curves are shifted for clarity. (b) The Lassajous figure for the last 500 snapshots shows that Modes 1 and 3 are correlated, although some random drift between the phases is present.

Interestingly, the rate of phase advancements of all robust modes of the reacting flow at $\phi = 1.1$ are identical, as seen from Figure 6.18. (The Figure only shows one each from the four complex conjugate pairs of robust dynamic modes.) This observation suggests that the reacting flow at equivalence ration $\phi = 1.1$ contains one reproducible flow constituent which can be reconstructed using the 8 robust modes and the time average $\Phi_0(\mathbf{x})$. Figure 6.19 shows several snapshots of this reconstruction; it should be compared with the corresponding images of the original flow shown in Figure 6.12.

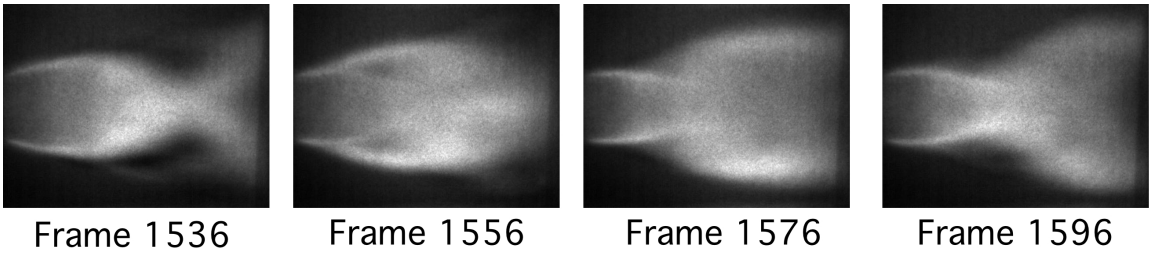

Figure 6.19: Several snapshots of the reconstruction of the reproducible flow using the robust modes. These snapshots should be compared with the corresponding snapshots of the original flow given in Figure 6.12.

6.4.3 Von Karman Vortex Shedding

The reacting flow at equivalence ratio $\phi = 0.8$ contains symmetric vortex shedding as well as von Karman shedding. Here noise and non-reproducible facets of the flow are significantly higher than at $\phi = 1.1$. Part of this irregularity may be consequent to the nonlinear coupling between symmetric and von Karman vortex shedding.

6.4.3.1 Proper Orthogonal Decomposition

The reacting flow at $\phi = 0.8$ has both symmetric and asymmetric coherent structures [13, 28], the leading modes being symmetric. As discussed in Ref. [28], the asymmetric modes need to be associated with von Karman vortex shedding. Figure 6.20 shows the symmetric and asymmetric modes with the highest latencies.

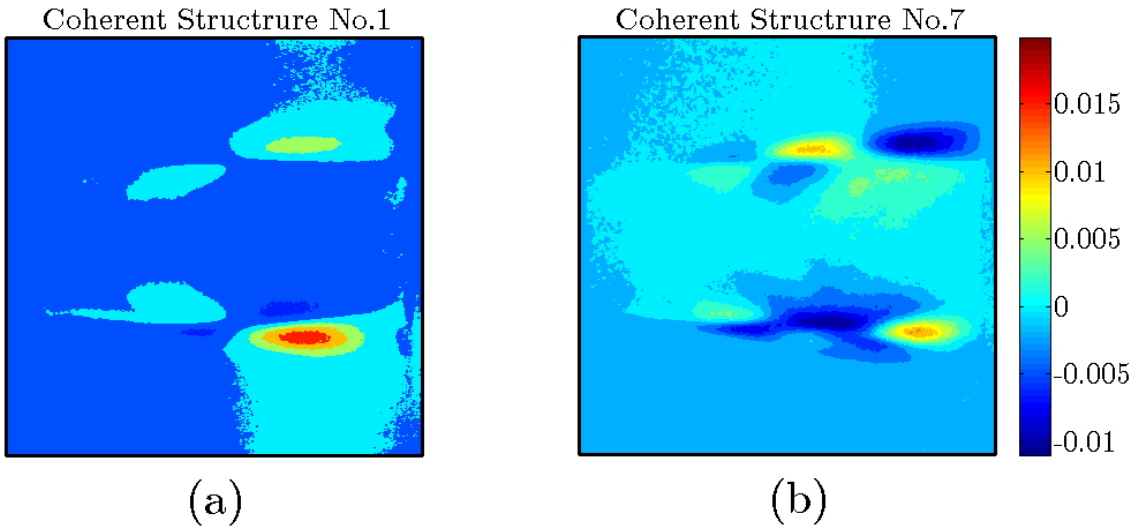

Figure 6.20: (a) Symmetric and (b) asymmetric modes with largest latencies for the reacting flow at $\phi = 0.8$. The asymmetric modes represent von Karman vortex shedding [13, 28].

6.4.3.2 Dynamic Mode Decomposition

Figure 6.21(a) shows the Koopman eigenvalues of the flow at $\phi = 0.8$ and Figure 6.21(b) presents the robust modes that were identified using 2000-frame sections of the flow.

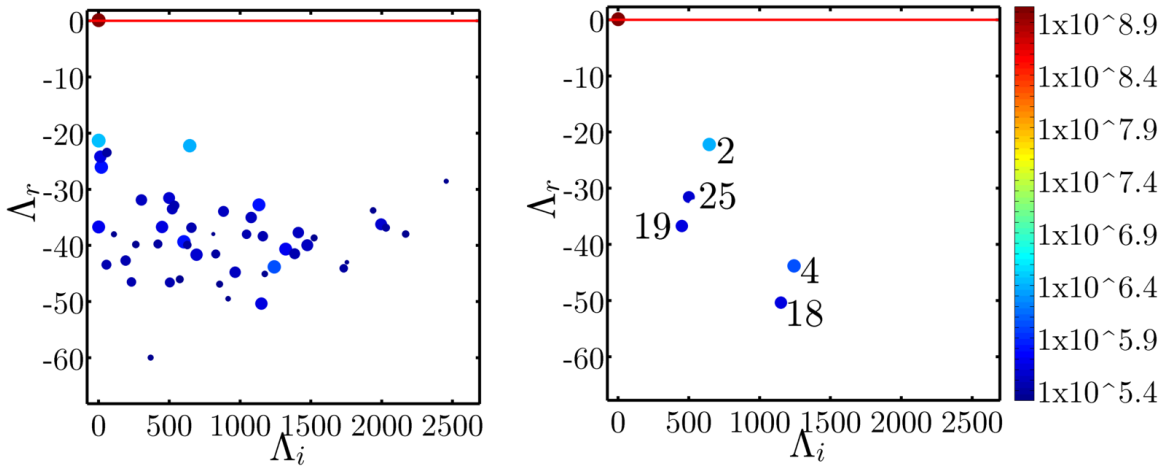

Figure 6.21: (a) The DMD spectrum for the reacting flow at equivalence ratio $\phi = 0.8$. The flow exhibits symmetric vortex shedding as well as von Karman shedding at this equivalence ratio. (b) Modes 2 and 4 are robust, and modes 18, 19, and 25 are asymmetric modes with the largest latency. Eigenvalues of the last three differ slightly between different subsections of the flow.

Modes 2 and 4 are robust and symmetric about the x-axis. Asymmetric modes with the largest latencies are 18, 19 and 25; however, they are not robust, differing slightly between different subsections of the video. Figure 6.22 shows the real and imaginary parts of $\Phi_2(\mathbf{x})$, the spectrum $\hat{a}_2(\omega)$ of the real part of $a_2(t)$, and the phase advancement. The corresponding results for the asymmetric mode with the highest latency, $\Phi_{18}(\mathbf{x})$, is in Figure 6.23. As for the earlier cases, the phase advancement of $a_2(t)$ and $a_{18}(t)$ is significantly more regular (and noise-free) than the overall dynamics. This behavior reiterates the underlying regularity in the phase of vortex shedding. We also find that the rate of phase advancement of all major dynamic

modes are identical. Figure 6.24 shows several snapshots of the reacting flow along with the symmetric (modes 0, 2, and 4) and asymmetric (modes 18, 19, and 25) flow constituents.

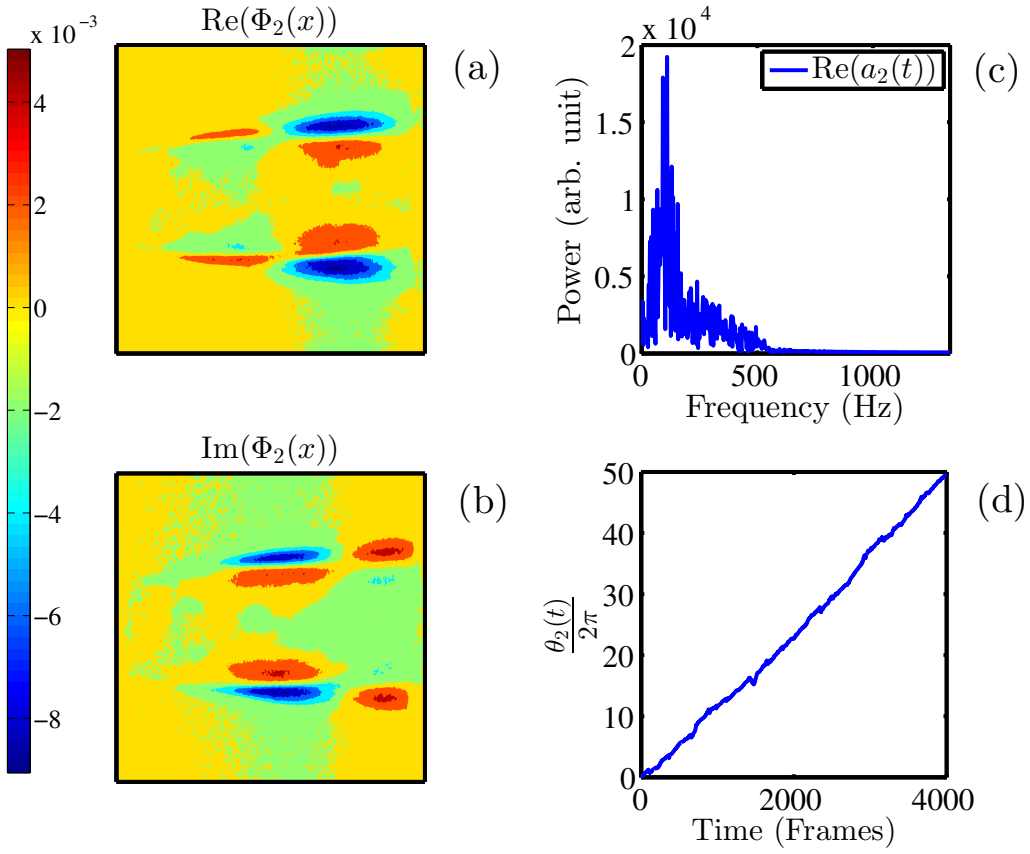

Figure 6.22: (a) Real and (b) imaginary parts of $\Phi_2(\mathbf{x})$ for the reacting flow at equivalence ratio $\phi = 0.8$. This mode has the largest latency among the symmetric dynamic modes. (c) $\hat{a}_2(\omega)$ is significantly noisier than the corresponding spectra at $\phi = 1.1$; it contains a peak at 125 Hz. (d) phase advancement of $a_2(t)$ is regular.

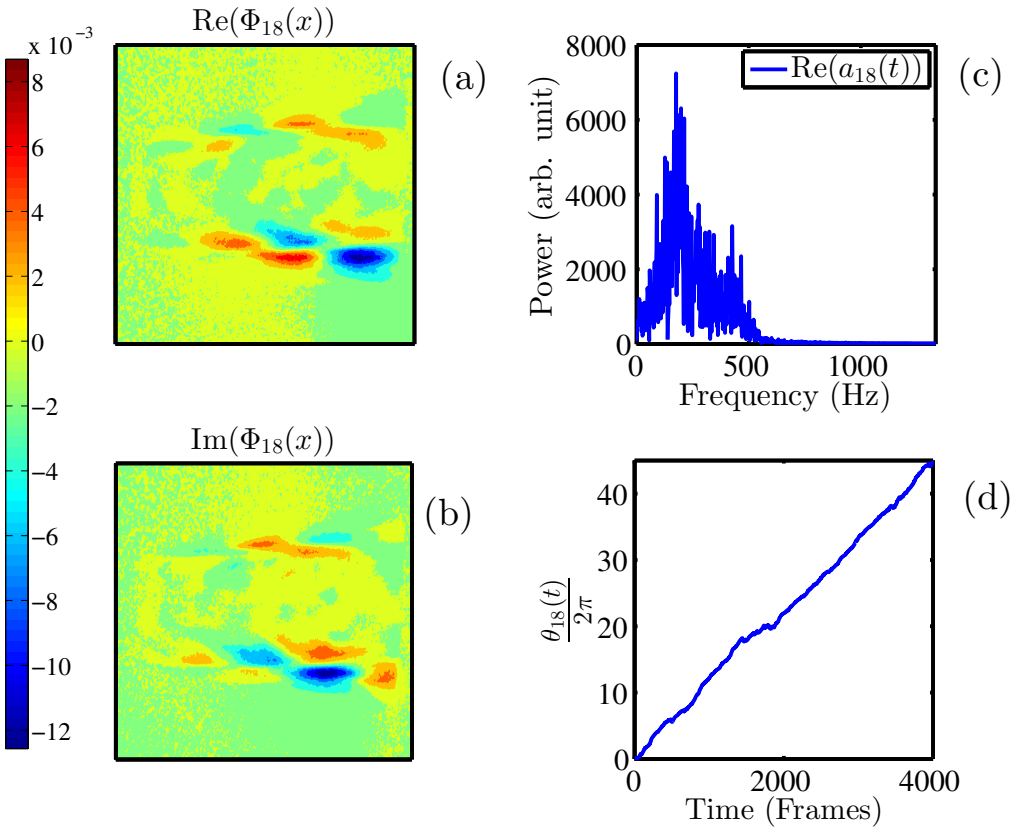

Figure 6.23: (a) Real and (b) imaginary parts of $\Phi_{18}(\mathbf{x})$ for the reacting flow at equivalence ratio $\phi = 0.8$. This mode has the largest latency among the asymmetric dynamic modes. (c) $\hat{a}_{18}(\omega)$ is significantly noisier than the corresponding spectra at $\phi = 1.1$; it contains a peak at 250 Hz. (d) phase advancement of $a_{18}(t)$ is regular.

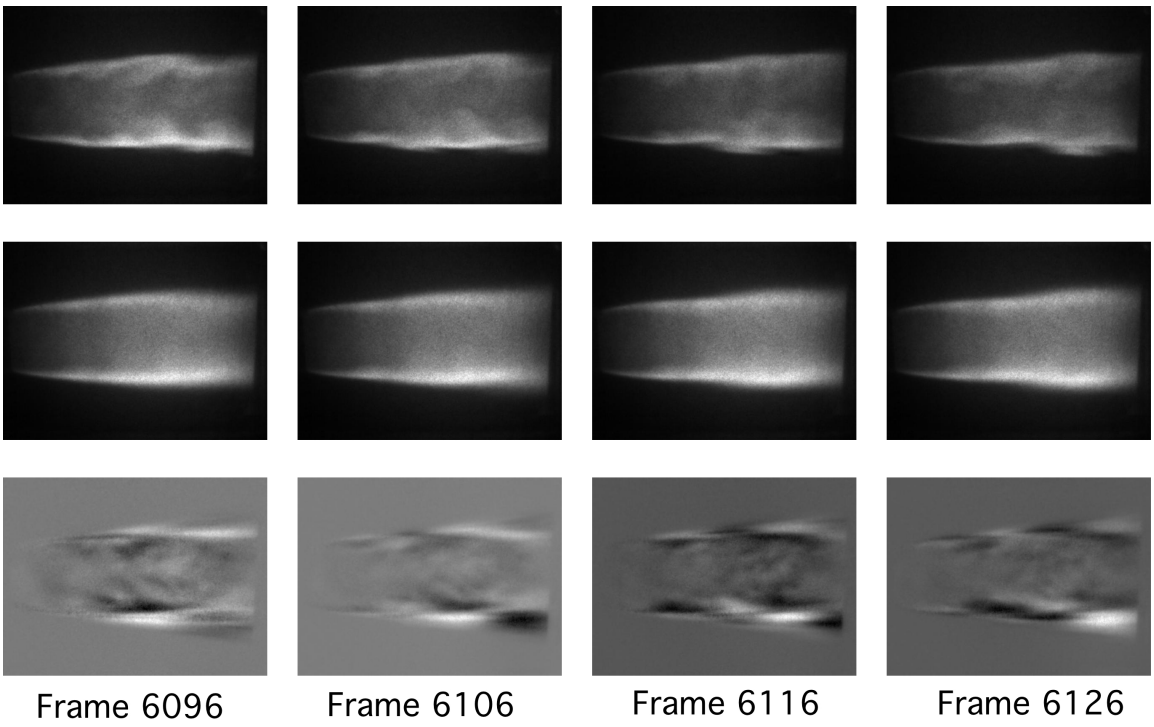

Figure 6.24: Several snapshots of reacting flow at $\phi = 0.8$ (top row) and reconstructions of the symmetric (second row) and asymmetric (bottom row) flow constituents.

6.5 Discussion

Combustion instabilities pose serious challenges to the design of lean, premixed, clean-burning combustors; they can severely limit combustor efficiency and cause catastrophic damage [1, 2, 3, 4]. A comprehensive analysis of combustion instabilities and how to prevent their onset can prove extremely useful in reactor design. Unfortunately, nonlinearity and long-range pressure variations complicate the analysis of combustion instabilities and limit the use of analytical and computational

approaches to efficient design.

Recent advances in high-frequency, high-resolution imaging provide an alternative strategy to analyze complex flows [26, 34]. The goal is to identify distinct flow constituents and determine the coupling between them. However, experimental flows contain noise and, especially in the case of turbulent convection, facets that are not reproducible; i.e., features, such as small scale eddies, that depend on the precise initial conditions and differ between multiple realizations of an experiment. Only their statistical properties are relevant. Thus, it is important to be able to differentiate reproducible features of the flow from noise and non-reporducible aspects. Once reproducible flow constituents are identified, it is possible to introduce a low-order model of the flow.

The first step in the analysis is a modal decomposition of the flow. Since most real combustors do not have symmetric regular shapes, the use of pre-specified bases, such as Fourier or wavelet bases, for post-processing is inefficient. Specifically, a large number of such modes are required to approximate nonlinear constituents like eddies. Approaches like proper orthogonal decomposition, which extract the optimal basis functions from data, can be expected to be more effective. Indeed, the structure and dynamics of eddies in turbulent combustion can be captured with a (relatively) small number of proper orthogonal modes [13, 28]. However, it is not possible to identify the set of coherent structures to be associated with a specific flow constituent, such as a periodically shed collection of von Karman vortices.

In this paper, we proposed the use of Koopman modes to de-convolute combustion flows. Koopman eigenvalues and eigenfunctions can be computed from a series of

equally spaced snapshots of the flow field. All spectral components of the dynamics underlying the flow are contained in the Koopman spectrum [33, 26, 34]. Each Koopman mode is associated with a single complex growth rate Λ. As in POD, the relative importance of a mode towards the reconstruction of the spatio-temporal dynamics can be estimated using an appropriately defined latency.

We analyzed two reacting flows using proper orthogonal and dynamic mode decompositions. The first was a non-trivial cellular state observed in a uniform circular flame front. A symmetry breaking bifurcation of a uniform circular flame front generates a variety of stationary and non-stationary cellular states of the flame [5, 38, 27]. The state we studied contained two rotating rings of cells which co-rotated with different angular speeds. The second set of flows analyzed were reacting flow behind symmetric bluff-bodies [42, 43, 13]. In one example, the flow contained only periodic shedding of symmetric pairs of vortices from the ends of the bluff body. In the second example, the flow contained symmetric and von Karman vortex shedding. Our goal in both studies was to de-convolute the flow into its constituents and to differentiate them from noise and other irregular features.

Both POD and DMD can be used to separate the two rings of cells of the co-rotating cellular state. The constituents exhibited the anticipateted symmetries and contained harmonics, required for the rotation of rings [39, 40]. POD was the more efficient decomposition in the sense that the spatio-temporal dynamics was approximated with the smaller number of coherent structures. In contrast, there were several dynamic modes with the same spatial structure but different growth rates. Thus, DMD presented more detailed dynamical descriptions of the modes.

We introduced a method to differentiate robust flow constituents from noise and non-reproducible facets of the co-rotating cellular state. It is based on the dynamic mode decomposition of several subsections of the flow, and identifying common eigenvalues. We conjectured that these robust modes capture the reproducible features of the dynamics and conversely that non-reproducible modes represent non-robust facets of the flow. It should be noted that proper orthogonal decomposition cannot be used for the purpose. First, as we discussed in Section 6.3.4, the POD modes are a combination of DMD modes, and the contribution of the individual components (some of which may be reproducible and others not) cannot be established. Second, the partition cannot be made using latency since some non-reproducible modes have high latency. The ability to differentiate between robust and non-robust modes is a significant advantage that DMD has over POD in post-processing experimental data.

We discovered that, although the phase space orbits were noisy, the angular motion (defined via the coefficient of DMD modes) associated with the state evolved with highly regular dynamics. The result suggests that the phase angle be used to describe the underlying dynamics and to associate strongly correlated dynamic modes using Lassajous figures. The rate of change of the phase angle was equal to the angular velocity of the corresponding ring of cells. Finally, a correlated group of dynamic modes can be used to reconstruct a flow constituent. We also note that, in general, it is not possible to define the an angular motion using proper orthogonal modes. This is a second advantage of DMD over POD as a means for post-processing data.

The conclusions made for the double rotating state applied to reacting flows as

well. Once again the flow can be approximated with a smaller number of POD modes. However, dynamic mode decomposition of multiple nominally identical sets of snapshots helped differentiate between robust and non-robust dynamic modes, and hence reproducible and non-reproducible flow characteristics. As in the co-rotating state, we defined a "phase" of the dynamic modes using their (time-dependent) coefficients. In bluff-body flows, it represents, not an angular position, but rather the downstream displacement of the associated vortex. The phase dynamics was found to be highly regular compared to the (erratic) changes in the magnitude of the coefficients. Using phase dynamics and Lassajous figures, we identified strongly correlated modes that were associated with a single flow constituent. Thus, we were able to reconstruct symmetric and asymmetric vortex shedding.

The ability to identify reproducible flow constituents and select dynamic modes associated with a flow constituent is helpful in constructing reduced-order models for the combustion flows. Construction of these models is based on the dynamics, symmetries and topological features of the reproducible flow constituents. They have to be supplemented by the statistical features of noise and other non-reproducible aspects of the flow.

6.6 Dynamic Modes and Coherent Structures

This Appendix section outlines a set of conditions under which a combination of dynamic modes with the same spatial structure is a coherent structure of the spatio-temporal dynamics. Consider first a spatio-temporal dynamics containing only a

single dynamic mode $\Phi(\mathbf{x})$ with an eigenvalue λ. Although λ may have a non-zero real part, external driving –and interactions between other modes– means that effectively $Re(\lambda) = 0$ for post-transcient dynamics; denote $\lambda = i\mu$, where $\mu \in \mathbb{R}$. Thus, the (real) spatio-temporal field is

$$u(\mathbf{x}, t) = e^{i\mu t}\Phi(\mathbf{x}) + e^{-i\mu t}\Phi^*(\mathbf{x}). \tag{6.11}$$

Noting that the time average $\langle e^{i\mu t}\rangle_t \sim \delta_{\mu 0}$, the correlation matrix is

$$C_{\mathbf{x},\mathbf{x}'} = \langle u(\mathbf{x}, t)u(\mathbf{x}', t)\rangle_t = \Phi(\mathbf{x})\Phi^*(\mathbf{x}') + \Phi^*(\mathbf{x})\Phi(\mathbf{x}'), \tag{6.12}$$

where $\mathbf{x}$ and $\mathbf{x}'$ are two spatial locations. Consequently

$$\sum_{\mathbf{x}'} C_{\mathbf{x},\mathbf{x}'}\Phi(\mathbf{x}') = N\alpha\Phi(\mathbf{x}) + N\beta\Phi^*(\mathbf{x}), \tag{6.13}$$

where $\alpha = \langle\Phi^*(\mathbf{x}')\Phi(\mathbf{x}')\rangle_{\mathbf{x}'} \in \mathbb{R}$, $\beta = \langle\Phi(\mathbf{x}')\Phi(\mathbf{x}')\rangle_{\mathbf{x}'} \in \mathbb{C}$, and N is the total number of spatial points.

Consider a "phase-advanced" (or in the case of the cellular state, rotated) pattern $e^{i\theta}\Phi(\mathbf{x})$ whose real part is $\Phi_R(\mathbf{x}) \equiv e^{i\theta}\Phi(\mathbf{x}) + e^{-i\theta}\Phi^*(\mathbf{x})$. Using Eqn. (6.13) and its complex conjugate

$$\sum_{\mathbf{x}'} C_{\mathbf{x},\mathbf{x}'}\Phi_R(\mathbf{x}') = N\left[\alpha e^{i\theta} + \beta^* e^{-i\theta}\right]\Phi(\mathbf{x}) + N\left[\alpha e^{-i\theta} + \beta e^{i\theta}\right]\Phi^*(\mathbf{x}), \tag{6.14}$$

With $\theta = (i/4)\ln(\beta/\beta^*)$, $\sum_{\mathbf{x}'} C_{\mathbf{x},\mathbf{x}'}\Phi_R(\mathbf{x}') \sim \Phi_R(\mathbf{x})$, and hence $\Phi_R(\mathbf{x})$ is an eigenfunction of $C_{\mathbf{x},\mathbf{x}'}$; i.e., the phase-advanced dynamic mode is a coherent structure.

Next we extend the result to a field formed by a linear combination of a set of dynamic modes with the same spatial structure with perhaps phase-advances. As before, the effective real part of the corresponding eigenvalues are zero due to the fact

that the spatio-temporal state is post-transcient. The corresponding spatio-temporal pattern can be written as

$$u(\mathbf{x},t) = \left(\sum_k c_k e^{i\mu_k t + i\theta_k}\right)\Phi(\mathbf{x}) + \left(\sum_k c_k^* e^{-i\mu_k t - i\theta_k}\right)\Phi^*(\mathbf{x}), \tag{6.15}$$

where c_k is the coefficient and θ_k's is the pause advance of the k^{th} DMD mode and $e^{i\mu_k t}$ is its eigenvalue. Since the μ's are distinct, the corresponding correlation matrix is

$$C_{\mathbf{x},\mathbf{x}'} = \left(\sum_k |c_k|^2\right)\left[\Phi(\mathbf{x})\Phi^*(\mathbf{x}') + \Phi^*(\mathbf{x})\Phi(\mathbf{x}')\right]. \tag{6.16}$$

It follows that a phase-advanced dynamic mode is a coherent structure for the spatio-temporal dynamics.

Finally, we outline how the result generalizes to a spatio-temporal field with two dynamic modes. The generalization to multiple modes is trivial. Denote the two dynamic modes by $\Phi_1(\mathbf{x})$ and $\Phi_2(\mathbf{x})$. The spatio-temporal field can be expressed as

$$u(\mathbf{x},t) = c_1 e^{i\mu_1 t}\Phi_1(\mathbf{x}) + c_2 e^{i\mu_2 t}\Phi_2(\mathbf{x}) + c.c., \tag{6.17}$$

where c_1 and c_2 are the coefficients of the dynamic modes and $c.c.$ represents the complex coefficient. The correlation matrix for the state is

$$C_{\mathbf{x},\mathbf{x}'} = |c_1|^2\Phi_1(\mathbf{x})\Phi_1^*(\mathbf{x}') + |c_1|^2\Phi_1^*(\mathbf{x})\Phi_1(\mathbf{x}') + |c_2|^2\Phi_2(\mathbf{x})\Phi_2^*(\mathbf{x}') + |c_2|^2\Phi_2^*(\mathbf{x})\Phi_2(\mathbf{x}'). \tag{6.18}$$

Defining $\alpha_1 = \langle\Phi_1(\mathbf{x}')\Phi_1^*(\mathbf{x}')\rangle_{\mathbf{x}'} \in \mathbb{R}$, $\beta_1 = \langle\Phi_1(\mathbf{x}')\Phi_1(\mathbf{x}')\rangle_{\mathbf{x}'} \in \mathbb{C}$, $\gamma_1 = \langle\Phi_1(\mathbf{x}')\Phi_2^*(\mathbf{x}')\rangle_{\mathbf{x}'} \in \mathbb{C}$ and $\gamma_2 = \langle\Phi_1(\mathbf{x}')\Phi_2(\mathbf{x}')\rangle_{\mathbf{x}'} \in \mathbb{C}$, it can be seen that

$$\sum_{\mathbf{x}'} C_{\mathbf{x},\mathbf{x}'}\Phi_1(\mathbf{x}') = N\alpha_1\Phi_1(\mathbf{x}) + N\beta_1\Phi_1^*(\mathbf{x}) + N\gamma_1\Phi_2(\mathbf{x}) + N\gamma_2\Phi_2^*(\mathbf{x}). \tag{6.19}$$

If the domains of $\Phi_1(\mathbf{x})$ and $\Phi_2(\mathbf{x})$ do not overlap (as is the case for the first two dynamic modes for the double rotating state –see Figures (6.8) and (6.10)), then $\gamma_1 = 0 = \gamma_2$. Then, Eqn. (6.19) reduces to Eqn. (6.13). Consequently, a phase-advanced dynamic mode is a principal component, as was noted in Section 6.3.

Bibliography

[1] J. B. Heywood, Internal Combustion Engine Fundamentals, McGraw-Hill, Inc., New York, 1988.

[2] Y. S. Matros, Unsteady Processes in Catalytic Reactors, Elsivier Science Publishers, Amsterdam-New York, 1985.

[3] G. A. Viswanathan, M. Sheintuch, D. Luss, Transversal hot zones formation in catalytic packed-bed reactors, Industrial and Engineering Chemistry Research 47 (2008) 7509–7523.

[4] G. Viswanathan, D. Luss, Moving transversal hot zones in adiabatic, shallow packed-bed reactors, AICHE Journal 52 (2006) 705–717.

[5] M. Gorman, M. elHamdi, K. Robbins, Chaotic dynamics near the extinction limit of a premixed flame on a porous plug burner, Combustion Science and Technology 98 (1994) 47–56.

[6] T. Lieuwen, Modeling premixed combustion-acoustic wave interactions: A review, Journal of Propulsion and Power 19 (2003) 765–781.

[7] J. Hertzberg, I. Shepherd, L. Talbot, Vortex shedding behind rod stabilized flames, Combustion and Flame 86 (1991) 1–11.

[8] F. P. Incropera, D. P. deWitt, T. L. Bergman, A. S. Lavine, Fundamentals of Heat and Mass Transfer, John Wiley and Sons, Hoboken, NJ, 1990.

[9] E. Motheau, Y. Mery, F. Nicoud, T. Poinsot, Analysis and modeling of entropy modes in a realistic aeronautical gas turbine, Journal of Engineering for Gas Turbines and Power-Transactions of the ASME 135 (2013) 092602.

[10] S. Chandrasekhar, Hydrodynamic and Hydromagnetic Stability, Dover Publications, Inc., New York, 1961.

[11] P. G. Drazin, W. H. Reid, Hydrodynamic Stability, Cambridge University Press, Cambridge, UK, 1981.

[12] F. Nicoud, K. Wieczorek, About the zero Mach number assumption in the calculation of thermoacoustic instabilities, International Journal of Spray and Combustion Dynamics 1 (2009) 67–111.

[13] S. Kostka, A. C. Lynch, B. C. Huelskamp, B. V. Kiel, J. R. Gord, S. Roy, Characterization of flame-shedding behavior behind a bluff-body using proper orthogonal decomposition, Combustion and Flame 159 (2012) 2872–2882.

[14] P. Petersson, R. Wellander, J. Olofsson, H. Carlsson, C. Carlsson, B. B. Watz, N. Boestkjaer, M. Richter, M. Alden, L. Fuchs, X.-S. Bai, Simultaneous high-speed PIV and OH-PLIF measurements and modal analysis for investigating

flame-flow interactions in low swirl flames, in: 16^{th} International Symposium on Applications of Laser Techniques to Fluid Mechanics, Lisbon, Portugal, 2012.

[15] E. Ott, C. Grebogi, J. Yorke, Controlling chaos, Physical Review Letters 64 (1990) 1196–1199.

[16] T. Shinbrot, C. Grebogi, E. Ott, J. Yorke, Using small perturbations to control chaos, Nature 363 (1993) 411–417.

[17] A. Garfinkel, W. Ditto, M. Spano, J. Weiss, Control of cardiac chaos, Circulation 86 (1992) 217.

[18] A. Garfinkel, M. Spano, W. Ditto, J. Weiss, Controlling cardiac chaos, Science 257 (1992) 1230–1235.

[19] R. Roy, T. Murphy, T. Maier, Z. Gills, E. Hunt, Dynamic control of a chaotic laser - experimental stabilization of a globally coupled system, Physical Review Letters 68 (1992) 1259–1262.

[20] S. Schiff, K. Jerger, D. Duong, T. Chang, M. Spano, W. Ditto, Controlling chaos in the brain, Nature 370 (1994) 615–620.

[21] S. Schiff, K. Jerger, T. Chang, T. Sauer, P. Aitken, Stochastic versus deterministic variability in simple neuronal circuits .2. hippocampal slice, Biophysical Journal 67 (1994) 684–691.

[22] S. Narayanan, G. H. Gunaratne, F. Hussain, A dynamical systems approach to the control of chaotic dynamics in a spatiotemporal jet flow, Chaos 23 (2013) 033133.

[23] P. Cvitanović, G. H. Gunaratne, I. Procaccia, Topological and metric properties of Hénon-type strange attractors, Physical Review A 38 (1988) 1503–1520.

[24] D. Auerbach, P. Cvitanović, J.-P. Eckmann, G. Gunaratne, I. Procaccia, Exploring chaotic motion through periodic orbits, Physical Review Letters 58 (1987) 2387–2389.

[25] S. Bagheri, P. Schlatter, P. J. Schmid, D. S. Henningson, Global stability of a jet in crossflow, Journal of Fluid Mechanics 624 (2009) 33–44.

[26] C. W. Rowley, I. Mezic, S. Bagheri, P. Schlatter, D. S. Henningson, Spectral analysis of nonlinear flows, Journal of Fluid Mechanics 641 (2009) 115–127.

[27] A. Palacios, G. Gunaratne, M. Gorman, K. Robbins, Cellular pattern formation in circular domains, Chaos 7 (1997) 463–475.

[28] J.-C. Hua, G. H. Gunaratne, S. Kostka, N. Jiang, B. V. Kiel, J. R. Gord, S. Roy, Dynamical-systems analysis and unstable periodic orbits in reacting flows behind symmetric bluff bodies, Physical Review E 88 (2013) 033011.

[29] L. Sirovich, Turbulence and the dynamics of coherent structures .1. coherent structures, Quarterly of Applied Mathematics 45 (1987) 561–571.

[30] L. Sirovich, Turbulence and the dynamics of coherent structures .2. symmetries and transformations, Quarterly of Applied Mathematics 45 (1987) 573–582.

[31] L. Sirovich, Turbulence and the dynamics of coherent structures .3. dynamics and scaling, Quarterly of Applied Mathematics 45 (1987) 583–590.

[32] J. L. Lumley, The structure of inhomogeneous turbulent flows, in: Atmospheric Turbulence and Radio Wave Propagation, Nauka, Moscow, 1967, pp. 166–178.

[33] P. J. Schmid, Dynamic mode decomposition of numerical and experimental data, Journal of Fluid Mechanics 656 (2010) 5–28.

[34] I. Mezic, Analysis of fluid flows via spectral properties of the Koopman operator, Annual Review of Fluid Mechanics 45 (2013) 357–378.

[35] M. Bergmann, C. H. Bruneau, A. Lollo, Enablers for robust pod models, Journal of Computational Physics 228 (2009) 516–538.

[36] P. J. Schmid, Dynamic mode decomposition of experimental data, in: Proceedings of 8th International Symposium on Particle Image Velocimetry, PIV09-0141, Melbourne, Victoria, 2009.

[37] W. H. Press, S. A. Teukolsky, W. T. Vetterling, B. P. Flannery, Numerical Recipes in C++: the Art of Scientific Computing, Cambridge University Press, Cambridge, UK, 2002.

[38] G. Gunaratne, M. elHamdi, M. Gorman, K. Robbins, Asymmetric cells and rotating rings in cellular flames, Modern Physics Letters B 10 (1996) 1379–1387.

[39] G. Dangelmayr, D. Armbruster, Classification of Z(2)-equivariant imperfect bifurcations with corank-2, Proceedings of the London Mathematical Society 46 (1983) 517–546.

[40] R. Goldstein, G. Gunaratne, L. Gil, P. Coullet, Hydrodynamic and interfacial patterns with broken space-time symmetra, Physical Review A 43 (1991) 6700–6721.

[41] T. Lieuwen, J. Cho, Coherent acoustic wave amplification/damping by wrinkled flames, Journal of Sound and Vibration 279 (2005) 669–686.

[42] L.-Z. Huang, D.-M. Nie, Vortex shedding patterns in flow past inline oscillating elliptical cylinders, Thermal Science 16 (2012) 1395–1399.

[43] E. Konstantinidis, S. Balabani, Symmetric vortex. shedding in the near wake of a circular cylinder due to streamwise perturbations, Journal of Fluids and Structures 23 (2007) 1047–1063.

[44] A. W. Caswell, N. Jiang, S. Roy, B. C. Huelskamp, J. R. Monfort, A. C. Lynch, V. Belovich, J. R. Gord, High-repetition-rate OH-PLIF and PIV measurements in bluff body stabilized flames, in: 52nd Aerospace Sciences Meeting, AIAA SciTech, American Institute of Aeronautics and Astronautics, 2014.